UNIVERSIDADE
BEIRA INTERIOR

Isolation of the Six-Transmembrane Epithelial Antigen of the Prostate 1 (STEAP1) using Gellan Gum Microspheres

João Pedro Batista da Silva

Dissertação para obtenção do Grau de Mestre em
Biotecnologia
(2º ciclo de estudos)

Orientador: Prof. Doutor Luís António Paulino Passarinha
Co-orientadora: Profª. Doutora Ângela Maria Almeida de Sousa
Co-orientador: Mestre Jorge Daniel Barroca Ferreira

Covilhã, outubro de 2022

Declaração de Integridade

Eu, João Pedro Batista da Silva, que abaixo assino, estudante com o número de inscrição M11087 do curso de Biotecnologia da Faculdade de Ciências, declaro ter desenvolvido o presente trabalho e elaborado o presente texto em total consonância com o **Código de Integridades da Universidade da Beira Interior**.

Mais concretamente afirmo não ter incorrido em qualquer das variedades de Fraude Académica, e que aqui declaro conhecer, que em particular atendi à exigida referenciação de frases, extratos, imagens e outras formas de trabalho intelectual, e assumindo assim na íntegra as responsabilidades da autoria.

Universidade da Beira Interior, Covilhã 10 /10 /2022

O conteúdo do presente trabalho é da exclusiva responsabilidade do autor

João Pedro Batista da Silva

(João Pedro Batista da Silva)

Acknowledgments

I would like to thank the following people, without whom I would not have been able to complete this master's dissertation.

First, I would like to thank my supervisors Professor Doctor Luís Passarinha and Professor Doctor Ângela Sousa for all the support, guidance and opportunities you have presented to me throughout this year. Your knowledge and insight steered this project in the right direction.

Second, I would like to thank Jorge Ferreira and Diana Gomes for helping me get started and for all the day to day guidance, advice and knowledge you shared with me. Sorry for taking so much of your time! I would also like acknowledge the University of Beira Interior and CICS-UBI research center for providing the facilities and materials necessary to develop this work.

Third, I would like to thank my friends for all the fun times spent together, talking about the most random things and for always being there for me. Particularly, Luís Pereira, José Bento and Vladyslav Lendel, I appreciate the fact that you took time to proofread several documents and for all the friendly banter, that always brightened my day.

Finally, I would like to acknowledge my parents for their efforts to keep me studying all these years, for always having my back and essentially for the opportunity to conclude this stage in my life. I am also grateful to my sister, for always believing in me and for her endless support.

Resumo Alargado

O cancro da próstata é um dos cancros mais frequentemente diagnosticados no sexo masculino, prevendo tornar-se a neoplasia maligna mais prevalente nos próximos anos. As terapias atuais têm eficácia limitada e não são suficientemente adequadas para mitigar as alarmantes taxas de incidência e mortalidade (aproximadamente 1.4 e 0.38 milhões, respetivamente) especialmente em fases mais avançadas não responsivas a tratamento hormonal. Desta forma, é crucial o desenvolvimento de novas abordagens de diagnóstico e terapêuticas. A *Six-Transmembrane Epithelial Antigen of the Prostate 1* (STEAP1) é uma proteína sobre-expressa no cancro da próstata, funcionando como um transportador transmembranar e canal iónico e desempenhando um papel na comunicação intercelular entre células tumorais. Adicionalmente, esta proteína foi associada com elevados níveis celulares de espécies reativas de oxigénio. Consequentemente, a sobre-expressão de STEAP1 leva ao aumento da proliferação celular e agressividade do tumor. Além disso, a STEAP1 está maioritariamente ausente em tecidos normais e órgãos vitais, sugerindo uma especificidade para o microambiente tumoral, indicando que esta proteína membranar pode ser considerada um potencial biomarcador e alvo terapêutico. No entanto, para explorar esse potencial, é necessário isolar frações de STEAP1 estáveis, bioativas e puras em concentrações elevadas. Atualmente, a principal limitação dos bioprocessos de natureza recombinante está relacionada com a fase de *downstream*, sendo que estas etapas contabilizam aproximadamente 80% dos custos totais. As etapas cromatográficas efetuadas em modo sequencial na purificação de STEAP1 não produzem rendimentos apropriados para a cristalização desta proteína e consequentemente promover a determinação da estrutura 3D e o desenvolvimento estudos de biointeração com antagonistas emergentes. Assim, o método *batch* surge como uma alternativa, considerando que é um método largamente aplicado na indústria, sendo capaz de combinar as etapas de clarificação, concentração e purificação primária de proteínas numa única etapa. Paralelamente, este método é simples, rápido e de baixo custo. A goma gelana é um exopolissacarídeo aniónico que tem a capacidade de formar géis termorreversíveis na presença de catiões divalentes. Desde a sua descoberta, este polímero foi aplicado com sucesso na indústria alimentar, farmacêutica e biotecnológica. Recentemente, foi demonstrada a aplicabilidade da gelana como matriz cromatográfica, devido a ser um polímero poroso, hidrofílico e possuir elevada capacidade de ligação. Este conceito foi também aplicado na formulação de microesferas de gelana para a captura de proteínas solúveis e pDNA. Assim, o principal objetivo deste trabalho foi desenvolver e otimizar um método de *batch* utilizando microesferas de gelana para a captura de STEAP1, uma proteína

transmembranar, diretamente de um lisado bruto de *Komagataella pastoris* X33 Mut$^+$. Para atingir este objetivo, as microesferas de gelana foram preparadas através do método de emulsão água-em-óleo pela extrusão de uma solução de 1.41% de gelana previamente aquecida a 90ºC sobre uma solução de óleo a 750 rpm e 100ºC. As microesferas foram reticuladas com cálcio e níquel, correspondendo aos tipos de estratégias iónica e de afinidade exploradas no *batch*, respetivamente. As microesferas foram caracterizadas relativamente ao diâmetro médio (microscopia semiótica), à morfologia (SEM) e composição química (FTIR e EDX). Os resultados obtidos demonstram que as microesferas apresentam uma morfologia esférica com uma estrutura uniforme e consistente, com tamanhos médio de 239.06 μm (níquel) e 330.37 μm (cálcio). O EDX demonstrou uma maior percentagem de integração de níquel, quando comparado com microesferas de gelana reticuladas com cálcio, justificando o menor tamanho destas microesferas pela formação de uma rede tridimensional mais compacta. Os espectros de FTIR juntamente com as percentagens iónicas obtidas por EDX demonstram o sucesso da etapa de reticulação. Em relação ao *batch*, várias otimizações foram realizadas visto que a STEAP1 apresentou alguma tendência de formar complexos estáveis com a gelana. Inicialmente, foi demonstrado que o detergente DM, a uma concentração de 0.1% (v/v), permitiu a solubilização mais eficaz e, por conseguinte, maior grau de recuperação de STEAP1. Posteriormente, a concentração ideal de lisado a injetar na matriz de gelana, correspondeu a ~7 mg de proteína total/mL, ou seja, uma diluição de 1:6 (concentração de lisado bruto de ~43 mg/mL) por cada produção de *batch*. Por último, verificou-se que 35 mL de microesferas de gelana para 6 mL de tampão é o rácio ideal a utilizar no método de captura em modo *batch*. As microesferas reticuladas com níquel foram utilizadas para a estratégia de afinidade. Surpreendentemente, a pH 9.2 foi possível ligar a totalidade de STEAP1 explorando a afinidade da sua cauda de histidinas aos iões de níquel presentes na superfície das microesferas de gelana. No entanto, no método de *batch* a STEAP1 provou ser sensível mesmo a modestas concentrações de imidazole e não foi possível recuperar a proteína alvo numa única fração. Contrariamente, as microesferas de cálcio utilizadas na estratégia iónica produziram resultados mais encorajadores. De facto, a STEAP1 liga totalmente a pH 6.2 em 10 mM MES e elui numa única fração na presença de 500 mM NaCl a pH 11 em 10 mM Tris. No entanto, não foi possível eliminar totalmente a formação de complexos STEAP1-gelana, mesmo com a implementação de várias etapas de otimização, nomeadamente, solubilização, concentração de lisado, rácio de microesferas e nas etapas do batch, bem como das suas respetivas concentrações de NaCl. Para descomplexar a STEAP1 da gelana, as frações recuperadas do *batch* iónico foram acopladas a uma etapa de polimento de co-imunoprecipitação, descomplexando os agregados STEAP1-gelana que resultaram numa fração de STEAP1 na forma

monomérica (~35 kDa) de elevado grau de pureza. Desta forma, demonstramos uma integração inovativa baseada no método de *batch* de gelana com uma etapa de co-imunoprecipitação que resulta na captura, clarificação e purificação de STEAP1.

Palavras-chave

Cancro da próstata, Clarificação, Co-imunoprecipitação, Gelana, Método de *batch*, STEAP1.

Abstract

Prostate cancer is one of the most frequent cancers diagnosed in males, predicted to become the most prevalent malignancy in upcoming years. Current therapies have limited efficacy and are not suitable to mitigate the alarming incidence and mortality rates, especially in later hormone-refractory stages. In this manner, it is crucial the development of novel approaches. Six-Transmembrane Epithelial Antigen of the Prostate 1 (STEAP1) is a protein highly overexpressed in PCa predicted to function as a transmembrane transporter and ionic channel, to play a role in intercellular communication between tumor cells and has been associated with the generation and propagation of high levels of reactive oxygen species. Consequently, STEAP1 leads to increased cellular proliferation and tumor aggressiveness. Furthermore, STEAP1 is mostly absent from normal tissues, suggesting a specificity for the cancer microenvironment, indicating that STEAP1 could have potential as a biomarker and therapeutic target. However, to explore this potential it is first necessary to isolate stable, bioactive and pure protein fractions of high concentration. Thus, we prepared calcium- and nickel-crosslinked gellan gum microspheres through a water-in-oil emulsion with 1.41% (w/v) gellan at 750 rpm and 100ºC. The microspheres were characterized trough FTIR, SEM and EDX, ensuring adequate size, morphology, and crosslinking. The microspheres were used to capture STEAP1 solubilized in 0.1% (v/v) DM derived from *Komagataella pastoris* X33 Mut^+ mini-bioreactor lysates using two different approaches, exploring ionic and affinity interactions. The ionic strategy presented the best results and consisted of STEAP1 capture in 10 mM MES buffer at pH 6.2. The target was then eluted by electrostatic repulsion with 10 mM Tris supplemented with 500 mM NaCl at pH 11. These optimized conditions allowed the recovery of STEAP1 in a single step, eliminating heterologous proteins in intermediary steps. The clarified fraction was polished by coupling with a Co-immunoprecipitation step. This technique was able to decomplex STEAP1-gellan gum complexes formed during the batch clarification. This innovative integration results in a monomeric STEAP1 fraction with high purity degree.

Keywords

Batch method, Clarification, Co-immunoprecipitation, Gellan Gum, Prostate Cancer, STEAP1.

Index

List of Figures

List of Tables

Isolation of STEAP1 using GG microspheres

List of Acronyms

3D	Three-dimensional
AOX	Alcohol Oxidase gene
AR	Androgen Receptor gene
ARG	Arginine
ATPS	Aqueous Two-Phase Systems
ATR	Attenuated Total Reflection
BCA	Bicinchoninic Acid
BMGH	Buffered Minimal Glycerol medium
BRCA	Breast Cancer gene
BSA	Bovine Serum Albumin
BSE	Backscattered Electron
CIS	Carcinoma *in situ*
Co-IP	Co-immunoprecipitation
COMT	Catechol-O-methyltransferase
CYMAL-5	5-Cyclohexyl-1-Pentyl-β-D-Maltoside
DM	n-Decyl-β-D-Maltoside
DMT1	Divalent Metal Transporter 1
DNA	Deoxyribonucleic acid
DNase	Deoxyribonuclease I
EDX	Energy-dispersive X-ray spectroscopy
ETS	Erythroblast Transformation-Specific transcription factors family
EWSR1	RNA-binding protein EWS 1 gene
FAD	Flavin Adenine Dinucleotide
FNO	F420H2:NADP+ oxidoreductase
FRE	Ferric Reductase family
FTIR	Fourier-transform infrared spectroscopy
GEN	Genapol X-100
GG	Gellan Gum
GLN	Glutamine
GSTP1	Glutathione S-Transferase Pi 1 gene
HAGG	High Acyl Gellan Gum
HIS	Histidine
IMAC	Immobilized Metal Affinity Chromatography

LAGG	Low Acyl Gellan Gum
MES	2-(N-Morpholino)ethanesulfonic acid
MRI	Magnetic Resonance Imaging
mRNA	Messenger Ribonucleic acid
MYC	Family of regulatory and proto-oncogenes
NaCl	Sodium chloride
NADPH	Nicotinamide Adenine Dinucleotide Phosphate
NMR	Nuclear Magnetic Resonance
NP-40	Nonidet P-40
NRF2	Nuclear factor erythroid 2-related factor 2 gene
O/W	Oil-in-water
OD_{600nm}	Optical density at 600nm
PCR	Polymerase Chain Reaction
pDNA	Plasmid DNA
pI	Isoelectric point
PIN	Prostatic Intraepithelial Neoplasia
PSA	Prostate-Specific Antigen
PTEN	Phosphatase and Tensin homolog gene
PTM	Post Translational Modifications
PVDF	Polyvinylidene difluoride
rhSTEAP1	Recombinant human six transmembrane epithelial antigen of the prostate 1
SDS	Sodium Dodecyl Sulfate
SDS-PAGE	SDS-Polyacrylamide Gel Electrophoresis
SEM	Scanning Electron Microscopy
SER	Serine
TEMED	*N,N,N′,N′*-Tetramethylethylenediamine
TMPRSS2-ERG	Transmembrane Protease Serine 2–ETS-related gene fusion
TP53	Tumor Protein 53 gene
TPP	Three-Phase Partitioning
W/O	Water-in-oil
YPD	Yeast Peptone Dextrose medium

List of Communications

Oral communication:

- XVII International CICS-UBI Symposium, Covilhã, July 2022: João Silva, Diana Gomes, Jorge Ferreira, Ângela Sousa, Luís Passarinha, Isolation of STEAP1 from a *Komagataella pastoris* lysate using gellan gum microspheres in a simple batch method.

Poster:

- Biopartitioning & Purification Conference (BPP2022), Aveiro, September 2022: João Silva, Diana Gomes, Jorge Ferreira, Ângela Sousa, Luís Passarinha, Capture of STEAP1 from *a Komagataella pastoris* lysate through a simple batch method using gellan microspheres.

List of Publications

- D. Gomes, J.P. Batista-Silva, J. Barroca-Ferreira, D. Costa, A. Sousa, L.A. Passarinha. Gellan gum microspheres and their applications in the biomedical industry. In A.K. Nayak, M.S. Hasnain. Gellan Gum as Biomedical Polymer (Submitted to Elsevier; In revision; Annex 1).
- D. Gomes, J.P. Batista-Silva, A. Sousa, L.A. Passarinha. Gellan gum-based materials: a review of preparation methods, characterization techniques and applications (Submitted).
- J.P. Batista-Silva, D. Gomes, J. Barroca-Ferreira, A. Sousa, L.A. Passarinha. Specific Six-transmembrane Epithelial Antigen of the Prostate 1 Capture with Gellan Gum Microspheres: Design, Optimization and Integration (Submitted to Carbohydrate Polymers; Annex 2).

Chapter 1 - Introduction

1.1. Prostate Cancer

Prostate cancer (PCa) is one of the leading cancers affecting the male population, second only to lung cancer. According to Globocan, PCa yearly incidence is predicted to increase from the current 1.4 million to 2.4 million new cases in 2040, with mortality rates following a similar trend [1]. Indeed, PCa is a multifactorial and complex disease with several risk factors, associated with germline susceptibility, acquired somatic mutations, and micro- and macroenvironmental components [2]. PCa incidence is undoubtedly related to age progression, with highest incidence being seen in elderly men [3]. PCa incidence is also correlated with a "Westernized" diet and lifestyle and higher country development indexes. Indicated in Figure 1, it is clear that higher PCa incidences are observed in North and Western Europe, North America, Brazil and Australia. It has been proposed that the western diet, characterized by high-fat and high-sugar foods coupled with excessive read meat consumption is a primary risk factor for PCa [3,4].

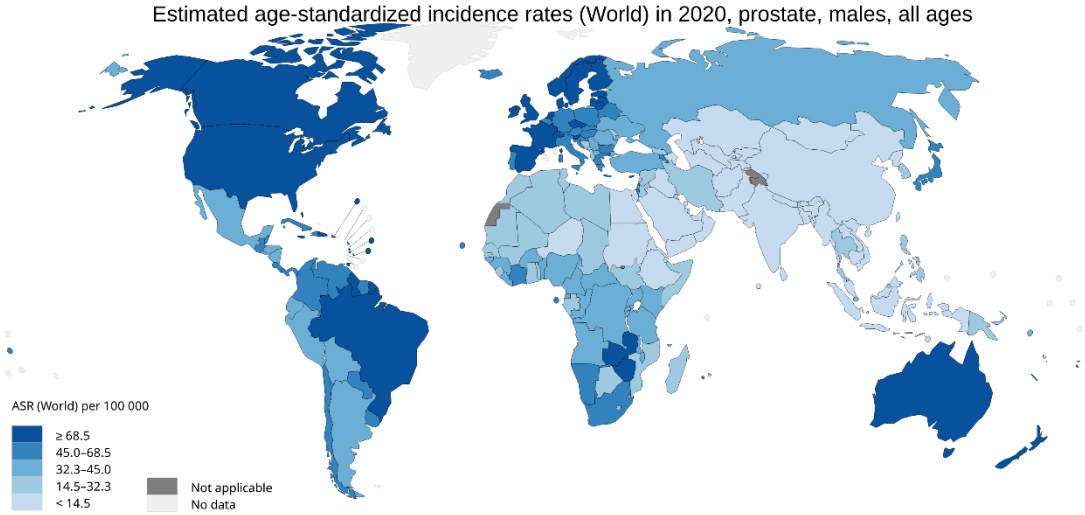

Figure 1. Global Geographical Incidence of PCa in 2020. Data from Global Cancer Observatory (https://gco.iarc.fr/today; Accessed in 23/08/2022).

Furthermore, smoking and obesity are also non-heritable risk factors involved in PCa [4,5]. There also appears to be some racial and ethnic differences, in regards to propensity for germline mutations. Mutations in DNA damage repair genes, particularly, BRCA1 and BRCA2, seems to be linked to earlier and more aggressive PCa [5,6]. The general molecular progression of PCa has been well defined since the early 2000s (Figure 2). Briefly, chronic inflammation and infection derived from several sources, is believed to be the driving force of PCa, through oxidative stress (generating reactive oxygen species), consequently inducing DNA damage and advancing normal prostate epithelium

to a proliferative inflammatory atrophy state. In this state, proliferative luminal epithelial cells may be more susceptible to epigenetic and genomic mutations, leading to prostatic intraepithelial neoplasia and malignant phenotype, eventually progressing to prostate adenocarcinoma [2–4]. Since then, a series of somatic alterations were identified to play a role in progression of PCa from benign tumors, to localized PCa and eventually to the aggressive metastatic state (Figure 3). The main changes can be gene fusions (e.g., TMPRSS2-ERG), overexpression of MYC proto-oncogene, deletion or mutations of the tumor suppressor genes PTEN and TP53 and amplification, mutation, overexpression and increased signaling of AR [2,4,5]. Indeed, these are the genetic factors with the highest frequency of alterations in both localized and castration-sensitive and castration-resistant PCa [2,7–10].

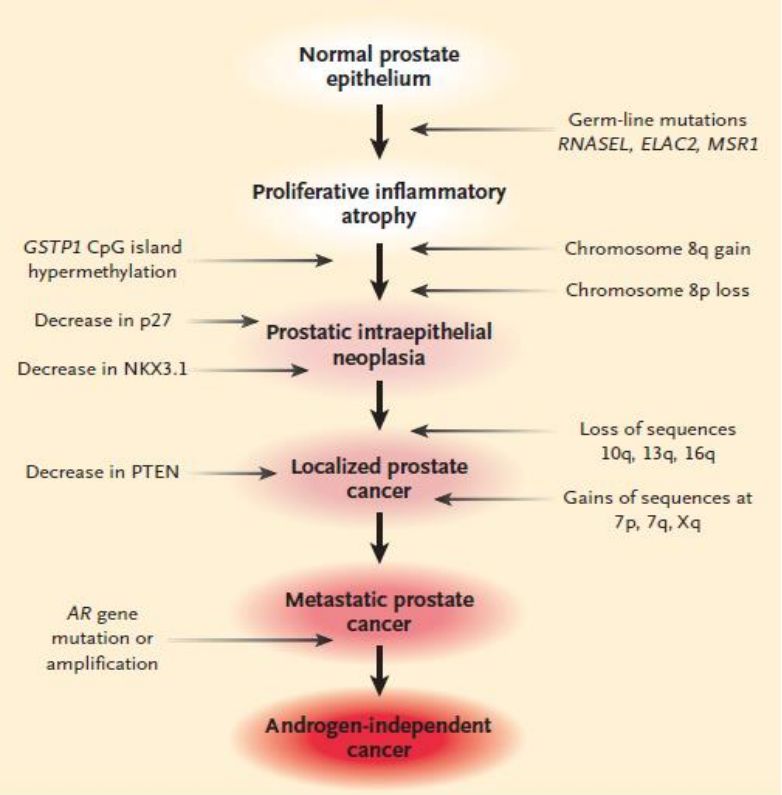

Figure 2. Molecular pathological initiation and progression of PCa and corresponding somatic mutations; Adapted from [4].

Currently, PCa is mainly diagnosed through the serum levels of prostate-specific antigen (PSA), while prognosis is asserted based on PSA levels, Gleason Score and the TNM classification system [11]. However, PSA lacks specificity and is often unsuccessful in distinguishing between malignant PCa and benign prostatic hyperplasia or prostatitis, resulting in excessive false positives [12,13]. Recently, new biomarker diagnostic kits emerged, testing the mRNA expression levels of several genes involved in PCa initiation and progression. However, given PCa heterogeneity, a singular diagnostic test is insufficient to provide accurate diagnosis [14]. In regards to treatment options,

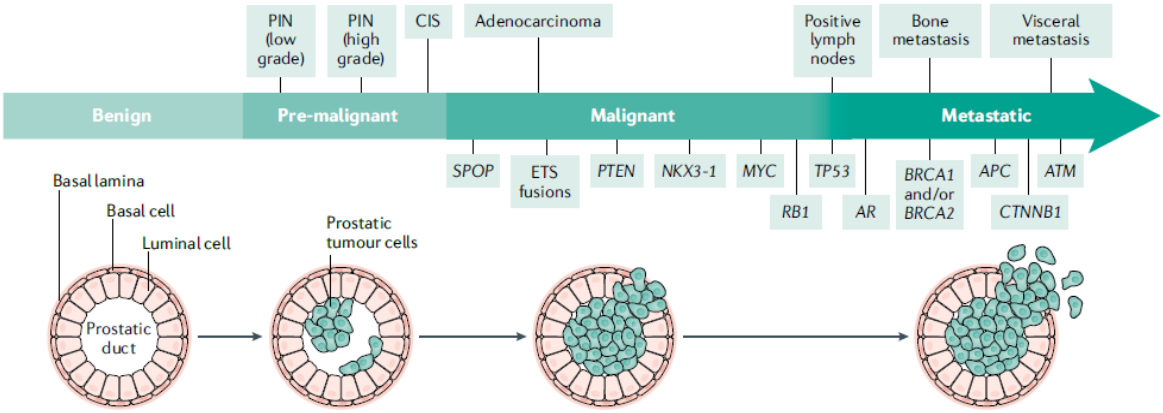

Figure 3. Somatic mutations involved in the progression of PCa; PIN: prostatic intraepithelial neoplasia; CIS: carcinoma *in situ*; Adapted from [5].

prostatectomy, androgen deprivation therapy, radiation and chemotherapy are the standard options for early stage PCa. Nevertheless, when PCa eventually advances to more aggressive stages, especially to androgen-independent metastasis or in the case of biochemical recurrence, these options exhibit very low efficacy and overall survival levels [15,16]. Indeed, novel approaches are necessary for both single test PCa-specific diagnosis, as well as, efficient treatment for advanced and aggressive PCa, which is normally viewed as incurable.

1.2. Six-Transmembrane Epithelial Antigen of the Prostate 1 (STEAP1)

1.2.1. Structural features and physiological functions

Six-Transmembrane Epithelial Antigen of the Prostate 1 (STEAP1), was discovered in 1999 by Hubert and coworkers in a metastatic PCa xenograft model [12]. It was the first identified member of the STEAP family of proteins, which now has 5 members (STEAP1-4 and STEAP1B2) [15]. There is great similarity between STEAP family members, in particular, structurally they possess six transmembrane domains, flanked by C- and N-termini, similar to yeast FRE family of metaloredutases and F420H2:NADP+ oxidoreductase (FNO) binding proteins, respectively [17]. Further, majority of STEAP proteins contain an YXXØ consensus sequence (Ø corresponds to amino acids with bulky hydrophobic side chain [18]) associated with anchorage of transmembrane proteins to lysosomes and endosomes. STEAP proteins also contain the Rossman fold (GXGXXG/A motif), which is common in oxidoreductase proteins [17]. Indeed, due to their structure, STEAP proteins have been appointed to play a role in metal homeostasis, participating in the reduction and uptake of iron and copper [19].

However, unlike STEAP2-4, STEAP1 does not contain an N-terminal NADPH binding domain, therefore, lacking the ability to reduce metals. Nevertheless, STEAP1 has been associated with the transferrin-bound Fe uptake pathway, suggesting that it might still have a role in iron metabolism [20]. STEAP1B2 is most homologous to STEAP1, however it contains only four transmembrane domains, and its function remains elusive [15,21].

STEAP1 gene is located on chromosome 7q21.13 and has a total length of 10.4 kb, comprising 5 exons and 4 introns. Although the transcription of the STEAP1 gene results in 2 mRNA transcripts, only the 1.4 kb transcript is processed into a mature protein, with a total of 339 aminoacids and predicted molecular weight of 39851.13 Da (compute Mw – Expasy; SIB) [12,17,22]. The molecular weight of STEAP1 has been reported with different values, but it is most likely due to differences in native [21] or recombinant sources [23] and the absence or presence of post translational modifications (PTMs) [21]. STEAP1 is a membrane protein overexpressed in PCa, while being absent or with low expression in other tissues and vital organs [12,17]. Indeed, STEAP1 expression in LNCaP cells is approximately 56 fold higher than in PNT2 cells [24]. In PCa, STEAP1 is expressed mainly at gap- and tight-junctions at the plasma membrane of epithelial cells [12,13,25]. Due to its role as a cell surface antigen and knowing its predicted secondary structure, homology was drawn to other proteins that function as transmembrane channels, and STEAP1 is believed to act as ionic channel, transporting sodium, calcium, potassium and small molecules, such as cytokines and chemokines [12,17,22,25,26]. STEAP1 has also been associated with cell adhesion and intercellular communication [15,17,26]. In fact, targeting PCA3 and LNCaP cells with anti-STEAP1 monoclonal antibodies considerably reduced intercellular communication, up to 90% [27]. Furthermore, silencing STEAP1 in mesenchymal stem cells leads to impairment in cell adhesion [28]. In addition, elevated levels of STEAP1 have also been found in extracellular vesicles. These assemblies are often associated with cargo trafficking and signal delivery, which might be an additional method used for PCa progression, apart from direct cell contact [29,30].

Recently, Oosterheert and Gros reported a partial 3D structure of homotrimeric STEAP1 (PDB: 6Y9B; Resolution: 2.97 Å; Figure 4). Each STEAP1 protomer was bound to a fragment of the clinically relevant mAb120.545 anti-STEAP1 antibody and contained a single b-type heme prosthetic group in its core [31]. Each subunit contains six α-helices, corresponding to the transmembrane domains of the protein, located at 71-91, 119-139, 164-184, 218-238, 258-278 and 291-311 base pairs of the aminoacid sequence, respectively. Membrane segments are connected by three extracellular loops, while the C- and N-termini reside in the intracellular space [12,31]. In addition, similar to what is found in the 3D structure of STEAP4, STEAP1 contains a specific FAD-binding domain, with the critical aminoacids involved in anchorage being GLN140, ARG161, SER237 and

GLN254 (Uniprot: Q9UHE8). Moreover, the iron contained in the heme group is axially coordinated by two histidine residues (HIS 175 and HIS 268), that are highly conserved throughout all STEAP family members. As previously described, STEAP1 does not contain an oxidoreductase-like NADPH binding domain spanning over ~175 aminoacids like other STEAP proteins. Instead, it has a long unorganized loop ranging from aminoacid 1-69, that does not provide enough electronic density to be modeled by Cryogenic-Electron Microscopy (Cryo-EM). Further, aminoacids from 313-339 also remain unmodeled [31]. Although on its own STEAP1 is incapable of reducing metals,

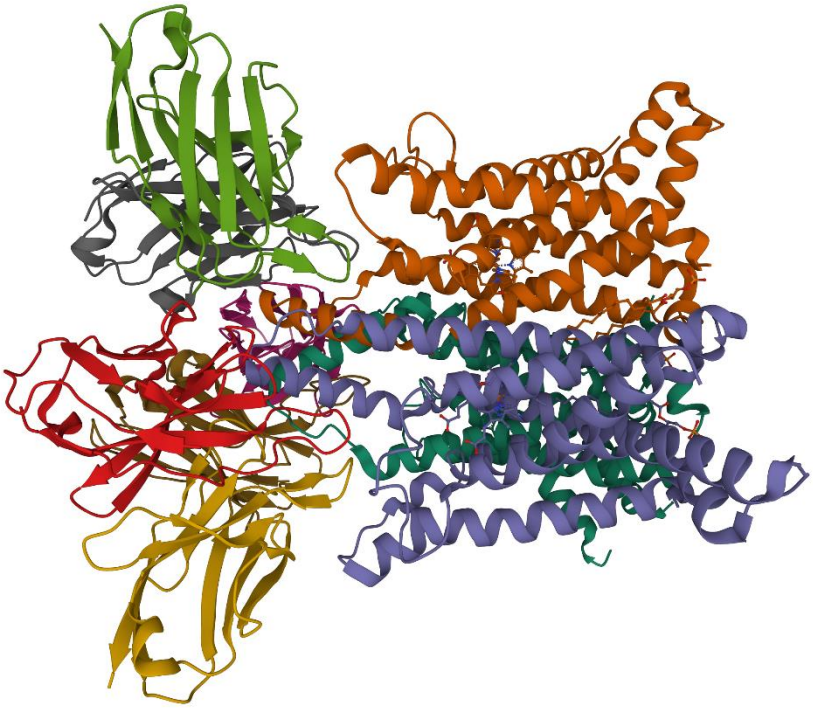

Figure 4. Cartoon representation of homotrimeric STEAP1. Each STEAP1 protomer is bound a single anti-STEAP1 antibody fragment and contains a single heme group in its core. Figure retrieved from PDB (code 6Y9B;[31]). Purple, dark green and orange represent each STEAP1 protomer, while light green, red and yellow are indicative of the coordinating mAb120.545.

Oosterheert and Gros also demonstrated that when STEAP1 is fused with the oxidoreductase domain of STEAP4 it is capable of promoting the reduction of iron(III), suggesting that STEAP1 can form heterotrimers with other STEAP members or other NADPH oxidoreductases to play a role in iron homeostasis [31]. This corroborates earlier findings from Kim and coworkers, where a STEAP1/2 heterotrimer was capable of reducing both iron and copper. The heterotrimer had a much higher affinity towards iron reduction, which also suggests a larger STEAP1 role in iron homeostasis [23]. Indeed, this research group also demonstrated that the redox potential of STEAP1's heme group is -114 to -118 mV, which indicates its efficacy and potential to reduce metal complexes *in vivo*. Additionally, they reported that STEAP1 also partakes in oxygen reduction,

resulting in the formation of superoxide, which suggests that it also acts as a superoxide synthase [23]. Furthermore, since STEAP1 is highly overexpressed in PCa and might be a key participant in the transferrin iron uptake pathway it is safe to assume that STEAP1 participates in the progression of PCa. Indeed, accumulation of high levels of iron has been shown to cause ill effects in neurodegenerative disorders, such as Alzheimer's, Parkinson's, and Huntington's diseases. In those cases, iron can donate electrons to oxygen, and when in excess it can generate hydroxyl radicals and hydroxyl anions through the Fenton reaction. Further, enhanced iron levels can also produce peroxyl and alkoxyl radicals due to iron-related lipid peroxidation [32]. This supports Grunewald and coworkers finding that STEAP1 is associated with oxidative stress responses and elevated levels of reactive oxygen species, which subsequently, are responsible for the activation of redox-sensitive and pro-invasive genes [33]. Normally, certain detoxification systems are in place to deal with reactive oxygen species. However as previously seen in Figure 2, GSTP1 gene and potential others antioxidant defense mechanisms are downregulated or deactivated in the transition from proliferative inflammatory atrophy to prostatic intraepithelial neoplasia [4]. The unilateral presence of STEAP1 throughout all PCa stages, especially the high levels in early prostatic intraepithelial neoplasia, also seem to suggest that this protein is a driving force, not only in the progression, through the production of oxygen reactive species, but also in the initiation and transition to a malignant phenotype [21,34].

The complete STEAP1 structure was recently predicted by AlphaFold, the state-of-the-art artificial intelligence (AI) for the computational prediction of 3D protein structures. When superimposed with the PDB deposited structure, AlphaFold (Entry: Q9UHE8) predicts transmembrane domains with over 90% accuracy. However, in regards to unorganized sections, which are the great majority of missing segments from the PDB structure, the prediction accuracy can fall to as low as 50%. Further, AlphaFold is so far incapable of predicting PTMs [35]. In fact, several PTMs sites were found in both N- and C-termini of STEAP1, which either are lacking in the PDB structure or have a modest accuracy value in the AlphaFold 3D prediction structure [21,25]. Since PTMs have been proposed as key differences between non-neoplastic PNT1A and neoplastic LNCaP [21], it seems that a solution for complete structural understanding of STEAP1 is still lacking.

Besides PCa, STEAP1 is also overexpressed in several other cancers, including, breast [36], bladder [37], colorectal [38], endometrial [39], Ewing's sarcoma [40], gastric [41], liver [42] , lung [43], ovarian [44], testicular [45] and in gliomas[46]. In most cases, similar to PCa, high STEAP1 expression is associated with tumor aggressiveness and dire outcomes. However, in endometrial, breast, colorectal and Ewing's Sarcoma, high

STEAP1 expression was correlated with higher overall survival and better outcomes. In endometrial and breast cancer, STEAP1 inhibited tumor progression by affecting the expression of epithelial to mesenchymal transition genes [39,47]. In colorectal cancer, STEAP1 controlled total levels of reactive oxygen species by regulation of nuclear erythroid 2-related factor (NRF2), opposed to what is seen in PCa [38]. In Ewing's sarcoma it was hypothesized that high expression of STEAP1 leads to sensitization of cells to chemotherapy [40]. Overall, it appears that STEAP1 can play different roles in several types of cancer depending on hormonal profile, cell type and cancer microenvironment [15]. Further, Ewing's Sarcoma is caused by the fusion of the EWSR1 gene with a member of the ETS family of transcription factors. The resultant gene seems to play a regulatory role in STEAP1 expression [48]. In PCa, the fusion of TMPRSS2 with ERG (member of ETS family) is a key factor for PCa development. Perhaps, this gene fusion could be related to STEAP1. Moreover, silencing STEAP1 in hepatocarcinoma suppressed the expression of c-Myc and promoted p27 activity [42]. Since both genes associated with these proteins are dysregulated in PCa, it is not unreasonable to assume that STEAP1 might play a similar role to what is exhibited in liver cancer. Indeed, it appears STEAP1 might be involved in several signaling pathways linked to initiation and progression of PCa.

1.2.2. Biomarker and therapeutic target

Due to the aforementioned STEAP1 functions, high cell surface expression and specificity for cancer microenvironment, this oncoprotein has been regarded as a potential biomarker and therapeutic target in PCa. It has been shown that STEAP1 is responsive to therapeutic treatment with sex hormones. In fact, 5α-dihydrotestosterone and 17β-estradiol induce STEAP1 down-regulation in LNCaP cells [49,50]. Furthermore, STEAP1 mRNA has been detected in the serum of cancer patients by real-time PCR [17,25,51]. In addition, it appears that higher levels of mRNA are detected in tumors from patients with biochemical recurrence [16]. This suggests that STEAP1 mRNA can be used as an early diagnostic tool, which could possibly predict cancer aggressiveness or potential for relapses. Likewise, STEAP1 has been appointed as a tumor-associated antigen that can act as a crucial target for immunotherapy. Specifically, [89Zr]Zr-DFO-MSTP2109A anti-STEAP1 antibody was well tolerated and suitable for positron emission tomography bioimaging in PCa, with the capability to track alterations in STEAP1 expression, and accordingly, monitor the progression of PCa [52–54]. This strategy could replace and improve upon the poor PCa detection, using Magnetic Resonance Imaging (MRI) as a diagnostic tool [2]. Antibody-Drug conjugates, in particular of anti-STEAP1 antibodies with monomethyl auristatin E, a potent antimitotic agent, have shown

aptitude in containing and lessening total tumor volume and hindering castration-resistant PCa [55–57]. The priming of cytotoxic T lymphocytes with STEAP1 epitopes in an attempt to improve immune responses and reduce tolerance has been another strategy heavily explored [58–60]. This strategy has been associated with higher T cell infiltration in the tumor microenvironment [61,62], reduced metastases [63] and tumor inhibition [37,64–67]. Indeed, the promise of the RNAActive® vaccine CV9103 has warranted clinical trials, where both CD4 and CD8 response was observed for STEAP1 [68]. Even so, immunotherapy-based approaches are a relatively new commodity, and in most cases the efficacy is modest at best. Certainly, these strategies are not yet potent enough to combat the immunosuppressive nature of the tumor microenvironment, being only a matter of time for the microenvironment to reject the primed lymphocytes or induce tolerance. Also, STEAP1 seems to contribute first hand in regards to immunosuppression [46].

1.2.3. Current STEAP1 production and purification methods

As previously discussed, the lack of a complete 3D structure is one of the most critical aspects of STEAP1 research. Since Cryo-EM was not able to produce, so far, the full STEAP1 architecture due to electron density issues, it is necessary to find alternatives [31]. Nowadays structure-based virtual screening and small drug discovery seems to be one of the most mature technologies to tackle cancer [69,70]. In parallel work, whilst virtual screening a series of potential STEAP1 inhibitors it was noticed that some molecules exhibited different binding sites and interacted with different aminoacids when screened *versus* the PDB or the AlphaFold structure (Blind docking approach; unpublished data from our research group). This exacerbates the compelling evidence that a complete structure is a requirement. Currently, the best course of action seems to be crystallization. However, this technique requires large amounts of purified protein to obtain high purity crystals [71]. Current landscape of STEAP1 production and purification workflow can be found in Table 1. Both STEAP1 produced in native form through LNCaP Cells [72] or recombinant STEAP1 produced in human embryonic kidney cells [31] or *baculovirus*-insect cells [23] are not yielding enough concentration for crystallization. Recently, our research group made strides in the optimization of recombinant human STEAP1 production in *Komagataella pastoris* (*K. pastoris*) [73]. *K. pastoris* is a popular host for the biosynthesis of heterologous proteins as it has the ability to process mature proteins with appropriate PTMs. Additionally, when induced by a methanol feed, heterologous protein levels can constitute up to 30% of the total cell protein content [74]. Moreover, this optimization was conducted in a benchtop mini-

bioreactor platform, which indicates the ease of scalability and also has the potential to yield high STEAP1 titers [73]. As this moment, this seems to be one of the most promising upstream strategy and attention should be turned towards downstream optimization. Indeed, most purification methods currently available are centered on sequential chromatographic steps (Table 1). But as can be seen by the lack of an appropriate structure these methods fail to obtain enough pure STEAP1 concentration. In turn, if these strategies were coupled for instance with crude and complex lysates derived from the aforementioned upstream process, it would either take several chromatographic runs or a large scale-up of chromatographic columns, which would increase total bioprocess costs to exorbitant amounts. Therefore, new alternatives are needed that can act as a primary capture and purification step, while keeping downstream costs feasible.

Table 1. Overview of current upstream and downstream processes in the pursuit of 3D STEAP1 structural determination; Adapted from [72]; Ref from top to bottom [72,31,23].

Protein	Expression System	Extraction	Isolation	Chromatographic Buffers	Structural Resolution
Native Human STEAP1	Neoplastic Prostate Cancer Cells (LNCaP)	RIPA Buffer (50 mM Tris Base, 150 mM NaCl, 1 mM EDTA, 0.5% Sodium Deoxycholate, 0.1% SDS, 1% NP-40, pH 7.8)	Hydrophobic Interaction Chromatography (Butyl-Sepharose) coupled to Co-Immunoprecipitation	1.375 M $(NH_4)_2SO_4$, pH 7.8 (Binding) 10 mM Tris, pH 7.8 (Elution)	n.a.
Recombinant Human STEAP1	Human Embryonic Kidney Cells (HEK)	Ordinary Lysis Buffer (50 mM Tris, 250 mM NaCl, 0.7% digitonin, 0.3% n-Dodecyl-β-D-Maltoside, 0.06% Cholesteryl hemi-succinate, pH 7.8)	Affinity Chromatography (Streptactin) (*A*) Size Exclusion Chromatography (Superdex 200 10/300) (*B*)	50 mM Tris, 250 mM NaCl, 0.08% digitonin, pH 7.8 (Binding Buffer A) Binding Buffer A + 3.5 mM desthiobiotin (Elution Buffer A) 20 mM Tris, 200 mM NaCl, 0.08% digitonin, pH 7.8 (Buffer B)	~3.0 Å Cryo-EM structure of trimeric human STEAP1 bound to three antigen-binding fragments of mAb 120.545 (PDB 6Y9B)
Recombinant Rabbit STEAP1	*Baculovirus*-Insect Cells	Ordinary Lysis Buffer (200 mM HEPES, 150 mM NaCl, 1 mM PMSF, 5 mM $MgCl_2$, 5 mM Imidazole, 10 μM hemin chloride, 1.5% MNG-DDM, pH 7.5)	Affinity Chromatography (Talon Co^{2+}) (*A*) Size Exclusion Chromatography (Superdex 200 10/300) (*B*)	20 mM HEPES, 150 mM NaCl, 20 mM Imidazole, 10 μM hemin chloride, 0.1% MNG-DDM, pH 7.5 (Buffer A) 20 mM HEPES, 150 mM NaCl, 0.01% MNG-DDM, pH 7.5 (Buffer B)	n.a.

1.3. Batch Method

Downstream processing is currently the main bottleneck in the production of biopharmaceuticals. As opposed to upstream fermentation advances, purification techniques have progressed at a slower pace in the last 2 decades. Since purification processes account for up to 80% of total process costs, with chromatographic techniques being at the forefront of rampant costs, new innovations are being sought out [75–77]. Thus, techniques that offer process integration, reducing the amount of low value added unit operations and that can handle large volumes of feed while maintaining high product recovery and purity have been in the spotlight. These methods have been developed for initial low-resolution steps, for the direct capture of target products from complex lysates, integrating clarification, concentration and primary capture and purification into a single batch step [77,78]. Liquid-liquid extraction and batch adsorption have been the most suitable techniques to tackle said requirements.

Liquid-liquid extraction can be divided into two main techniques: Aqueous two-phase systems (ATPS) and Three-phase partitioning (TPP). Both systems have been widely used for the separation and purification of several bioproducts, including, cells, viruses, enzymes and pDNA [77,79]. ATPS exploits the differential partition of target biomolecules between two immiscible phases, usually generated by either two polymers or a polymer and salt. The bioproduct is partitioned based on its intrinsic properties to one phase, while impurities move to the other phase. TPP follows a similar protocol, however one phase is composed of an organic solvent, usually *tert*-butanol [79–81]. The major upside of both techniques is the capability to deal with large quantities of complex feeds and the fact that they can be ran in continuous mode. However, since the molecular mechanisms that regulate target molecule partition (e.g., size, electrochemical, hydrophobicity, conformation, among others), as well as, characteristics of the components of the phases used are usually not well established, making optimization of these systems long-lasting and laborious. Moreover, difficulties were observed in scaling up and validation in the clearance of impurities, especially in ATPS, where the phase forming polymers may be hard to remove [77]. In the case of TPP, this method has been reported to cause loss of activity in enzymes and to induce protein structure changes [80].

Alternatively, batch adsorption has been applied to the separation of several relevant proteins and antibodies [82]. This method consists of the application of a complex protein solution with a fixed amount of adsorbent particles, where adsorption can be controlled by adsorption buffer conditions to exploit potential differences

between target protein and impurities. Then, a washing step is usually employed to clarify the bound proteins, by removing impurities. And finally, elution is carried out by exchange in the surrounding solution, usually being recovered with an additional step, most often centrifugation [82]. A Batch protein adsorption scheme can be found in Figure 5, represented by the three main typical steps: binding of proteins in crude lysate to the adsorbent particles, followed by a washing step, usually by modification of buffer conditions, and finally, elution of the clarified and partially clarified protein solutions by applying buffer conditions that are unfavorable for the interaction [82].

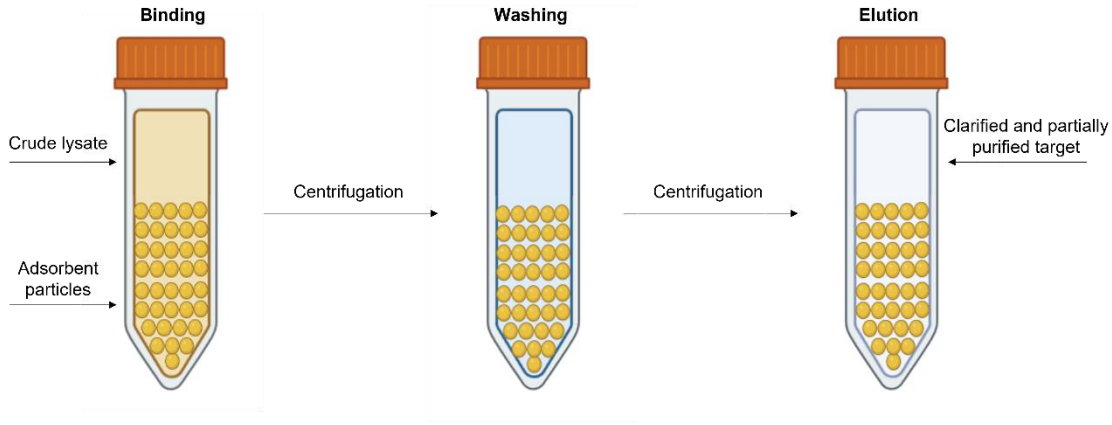

Figure 5. Schematic representation of the Batch method and the three characteristic steps: Binding, Washing and Elution.

The protein batch adsorption method is favored in cases where a large volume of feed must be processed rapidly to accomplish efficient cycle times or where proteolysis of target protein is a concern, since stirred batch tank adsorption is faster than column-mode adsorption. Furthermore, it is also advantageous in handling crude feeds with high viscosity or high quantities of debris [82]. Similar to liquid-liquid extraction, batch adsorption is best suited for low-resolution clarification, concentration and capture steps, where bulk impurity removal is essential for following high-resolution chromatographic polishing techniques [82]. The batch method has been described for silica-based materials and for magnetic particles, in which case the intermediary centrifugation steps are replaced with magnet separation [83–87]. However, magnetization of particles can quickly raise overall batch cost and complexity. Further, if the size or density of the particle is too large, such as silica, very high stirring velocities must be employed , which could cause protein denaturation, through the “egg-beater effect” [83]. Indeed, Hlady and coworkers recommended low-density materials, in particular gel beads, for batch protein adsorption as they can be suspended in the protein solution with milder stirring rates [83]. In addition, as size of particles decreases, it is expected an increase in specific surface contact area, thereby increasing total target protein adsorption [88]. Yet, there seems to be a bottom range as one can go, since

nanoparticles high surface area to volume ratio often causes colloidal instability and aggregation, altering their physicochemical properties and biological interactions, which could compromise batch adsorption [89]. In the micro range, this effect is not as prominent, therefore making hydrogel microbeads ideal for batch protein adsorption.

1.4. Gellan Gum

For a long time, there has been an increase in health-conscious consumers demanding natural food products. This has turned the food industry towards the use of biopolymers as food additives, fulfilling the role of texturizing agents, gelling and thickening agents, emulsion stabilizers and fat replacers [90,91]. At first, majority of polysaccharides used for this purpose were derived from plant sources, such as guar gum pectins, and starches. However, at the turn of the century, seasonal availability was a severe drawback. Consequently, microbial exopolysaccharides that can be produced reliably, reproducibly and under controlled conditions were introduced and found success in food, pharmaceutical and chemical industries, due to their unique structure and properties [91–93]. Microbial exopolysaccharides are water-soluble polymers that may or may not be ionic in its chemical nature, with regular, branched or unbranched repeating units that are connected by glycosidic linkages [92,93]. Gellan Gum (GG) is an extracellular bacterial polysaccharide, typically produced by fermentation of *Sphingomonas paucimobilis*, which secretes GG to the culture medium upon glucose metabolization [94,95]. GG was first identified by Kanego and Kang at Kelco in 1978, through an intensive screening program of soil and water bacteria, having received FDA approval in 1992 [92,95].

1.4.1. Structure and physical properties

Gellan gum is a linear, anionic, high molecular weight (~500 kDa) heteropolysaccharide composed by repeating tetrasaccharide units of β-D-glucose, β-D-glucuronic acid and α-L-rhamnose, in a ratio of 2:1:1 [96,97]. Protein and ash are also commonly found post extraction, but these can be removed by filtration or centrifugation [92]. GG can be divided into two main forms: native GG, also known as high acyl GG (HAGG) and deacetylated GG, also referred to as low acyl GG (LAGG) (Figure 6). High acyl GG contains two acyl groups, *O*-acetate and *L*-glycerate (0.5 mol and 1 mol per repeat unit, respectively), which are bound to the glucose residue adjacent to glucuronic acid [92,96]. Native GG can be transformed into the more common and commercialized deacetylated GG by hot alkaline hydrolysis. However, removal of acyl groups severely impacts the rheology of formed gels [98]. The former GG configuration produces soft

and elastic gels, whereas the latter produces hard, rigid and brittle gels. Furthermore, thermal stability increases upon alkaline treatment. However, low acyl GG requires cationic ions to induce gelation [96,99]. A comprehensive comparison of physical properties between both GG conformations can be seen in Table 2.

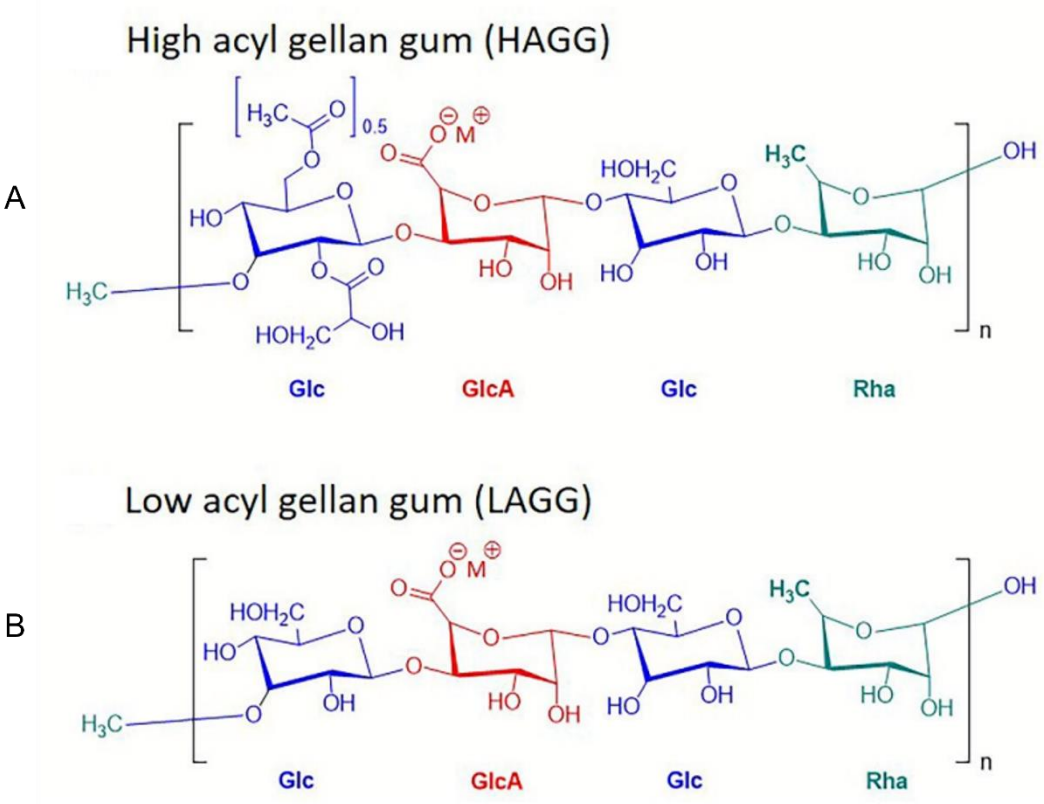

Figure 6. Molecular structure of both types of GG: Native/High Acyl (A) and Deacetylated/Low Acyl (B); Adapted from [96].

Table 2. Analysis of differential properties in both High Acyl and Low Acyl GG; Adapted from [99].

	HA Gellan Gum	LA Gellan Gum
Hydration	>80 °C	>80 °C
Sequestrants	No	Yes
Hot viscosity	Low	Low
Gelling ions	Not required	Yes (mono or divalent or acid)
Setting temperature	50 °C–80 °C	25 °C–60 °C
Melting	Yes	No (except low ionic strength and in milk)
Texture	Soft, elastic	Firm, brittle

1.4.2. Gelation process

Gellan gum undergoes gel transition during heating and cooling of GG solutions in the presence of enzymatic linkages, salts or pressure, with the gelation process being classified as a phase transition [92,100]. The GG gelation process can be divided into three main steps, based on the conformation GG adopts (Figure 7). First, GG is hydrated at temperatures >80◦C, yielding low viscosity solutions and ensuring proper GG dissolution, with a coil shape [94,99]. Upon cooling in the transition zone (ranging from 30-50◦C), a shift occurs transforming single-coil strands into a double helix configuration, which is stabilized by interchain hydrogen bonding and Van der Waals forces in the carboxylate groups of glucuronic acid residues [93,94,100]. Following, at setting temperatures, the double helices will aggregate into cation induced junction zones, forming a complex branched 3D network [100]. GGs gelling property is mainly governed by the type and quantity of cations, pH, temperature and polymer concentration [100]. Indeed, GG gels can be formed in pH ranges from 3.5 to 8. However, it has been shown that lower overall net charge at low pH values diminishes electrostatic repulsion between negatively charged chains and yields stronger gels [92]. Furthermore, GG undergoes gelation in the presence of monovalent, divalent and trivalent cations. Divalent cations appear to form stronger gels at lower concentrations than monovalent cations. The aggregation effect induced by monovalent cations appears to revolve around the screening of electrostatic repulsion between ionized carboxylate groups in GGs backbone, whereas for divalent cations, a chemical bond occurs between salt ions and two carboxylate groups in the glucuronate moiety, on top of the screening effect [96]. The presence of divalent cations during cooling also increases the total number of salt bridges, improving gelling properties. Moreover, gel strength is intensified with increases in polymer percentage. In addition, incorporation of sucrose or fructose into the GG matrix can also boost overall gel strength, reduce the necessary ion concentration and improve optical clarity [92].

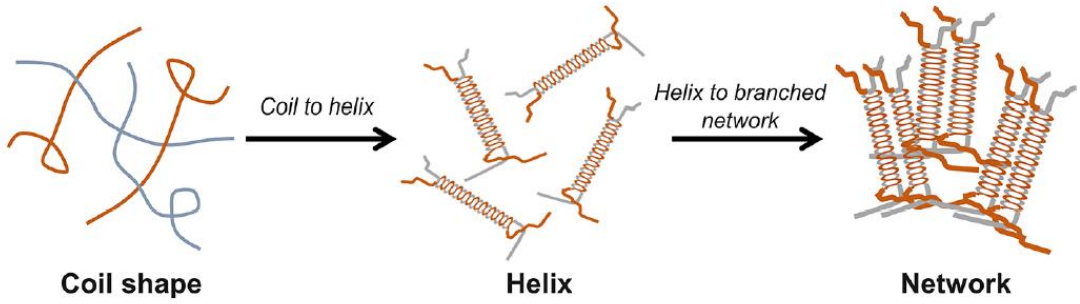

Figure 7. Schematic representation of the GG gelation process; Adapted from [94].

1.4.3. Applications

Conventionally, GG was predominantly used in the food industry due to its gelling, optical clarity and flavor release properties. The inherent thermal and acidic stability over the pH range of most food products also made it attractive for products that require rougher processing conditions [91,98,100,101]. Indeed, GG was incorporated into jams, jellies, fillings, dairy products, fabricated foods and a wide array of other confectionary and bakery products. Depending on the product, it acted as bulking, structuring, texturizing and thickening agent. Additionally, it could be used as a stabilizer and water-binding addictive, diminishing moisture fluctuations and inhibiting syneresis and was widely used to replace starches, which caused a blunting effect on food flavor [90–92,100]. Nowadays, it is also used as a preservative food additive, functioning as a hurdle and minimizing the deterioration of minimally processed food products. To this effect, GG has been incorporated into edible coatings and active packaging materials [102–106]. GG gels are also applied in cosmetics and dental care industries, as they function as emulsion stabilizers and suspenders in shampoos, and self-care products. The shear thinning rheology of these gels are also responsible for enhanced lubrication feel in lotions and creams. Similar to food, it is responsible for flavor release in toothpaste formulations [90,107].

Recently, biomedical, pharmaceutical and biotechnological applications were found for GG since it is a natural, biocompatible, biodegradable and abundant polymer. Moreover, its anionic nature means that it can be suitable for *in situ* gelling systems. It also possesses extraordinary mucoadhesive characteristics, with a structure rich in functional groups, readily physically or chemically modified [108–111]. In biotechnology, GG gels have been employed as an agar substitute to produce culture media for microorganisms and plants [91,92]. Incorporation of GG in pre-existing systems can also increase removal of uranium and nickel from contaminated bodies of water [112,113]. Similarly, a GG-based photothermal evaporator can promote desalination of polluted or regular seawater [114]. Moreover, GG beads can encapsulate enzymes or cells to promote degradation of environmental pollutants [115–117] or stimulate biosynthesis of economically valuable goods [118–120].

GG-based materials have also been heavily explored in the formulation of drug delivery systems. Indeed, due to such strong mucoadhesive features, GG has been mostly targeted towards routes of administration where a mucous membrane is present, in particular, the oral, nasal and ocular route. All of these routes are quite difficult to target, since they either degrade both drug and delivery system in harsh stomach conditions, are readily eliminated by the mucociliary clearance system or are expelled by rapid lid blink and tear turnover, respectively, limiting residence times and biodistribution [121–125].

However, *in situ* GG gelling systems can be administered to resist these clearance mechanisms in ocular and nasal cavities. In regards to oral administration, GG gels have high acidic stability and are not as affected by first pass metabolism, reaching intestinal targets. Nonetheless, if upper gastrointestinal delivery is the goal, several GG floating beads systems, incorporating effervescent materials or low density oils, have also been reported that remain at the stomach and exert desired function. Some of these systems are summarized in Table 3.

Table 3. Oral, ophthalmic and nasal GG-based drug delivery formulations and their application in the pharmaceutical fields; Adapted from [97].

Formulation	**Drug**	**Application**
Oral formulations		
GG beads	Theophylline	Phosphodiesterase inhibitor
	Propranolol hydrochloride	Beta-blocker
	Cephalexin	Antibiotic
	Metformin hydrochloride	Antidiabetic
	Amoxicillin	Antibiotic
	Glipizide	Type 2 diabetes mellitus
	Rifabutin	Antibiotic
In situ gelling system	Theophylline	Phosphodiesterase inhibitor
	Paracetamol	Analgesic, antipyretic
In situ floating gelling system	Amoxicillin	Antibiotic
Immediate release tablets	Metoclopramide	Antidiabetic
GG tablets	Metronidazole	Antibacterial
GG beads coated with chitosan	Amoxicillin	Antibiotic
Oil filled GG buoyant beads blended by Carbopol 934 or HPMC	Clarithromycin	Antibiotic
Microcapsules of GG and egg albumin	Diltiazem-resin complex	Antihypertensive
Acrylamide-grafted GG tablets	Metformin hydrochloride	Antidiabetic
Carboxymethyl GG beads	Metformin	Antidiabetic
Ophthalmic formulations		
In situ ophthalmic solution	Sezolamide, dorzolamide	Anti-glaucoma
	Pilocarpine	Anti-glaucoma
	Timolol maleate	Glaucoma
	Indomethacin	Anti-inflammatory

	Carteolol hydrochloride	Anti-glaucoma
	Pefloxacin mesylate	Antibiotic
	Piroxicam	Anti-inflammatory
	Gatifloxacin sesquihydrate	Antibiotic
	Timolol maleate	Anti-glaucoma
	Gatifloxacin	Bacterial conjunctivitis
	Matrine	
In situ ophthalmic nanoemulsion	Terbinafine hydrochloride	Fungal keratitis
Ocular insert	Ciprofloxacin hydrochloride	Bacterial conjunctivitis
Sustained delivery ophthalmic system	Methylprednisolone	
Soluble bioadhesive ocular insert	Gentamicin	Antibiotic for veterinary use
Albumin nanoparticles with GG for ophthalmic use	Pilocarpine	Anti-glaucoma
Nasal formulations		
In situ nasal gel	Fluorescein dextran	Epithelial uptake testing
	Scopolamine hydrobromide	Nausea, motion sickness
	Momethasone furoate	Anti-inflammatory
	Dimenhydrinate	Motion sickness
Intranasal microparticles	Metoclopramide	Antiemetic
GG microspheres	Sildenafil citrate	Erectile dysfunction

Over the last years, GG has also been investigated in tissue engineering in virtue of its biocompatibility, biodegradability and structural similarity to native glycosaminoglycans [96]. However, bare GG has weak mechanical strength, poor bone induction and smooth gel surface, thereby, lacking binding sites for cells. Incorporation of polymers, nanoparticles, demineralized bone powder or adhesion signaling peptides into GG biomaterials can tailor these composites to mimic the extracellular matrix, matching the mechanical properties of native tissue [126–130]. Moreover, GG hydrogels are characterized as superabsorbent materials that can absorb excess exudate and provide moisture to lesions [131]. Indeed, these GG scaffolds have been used as wound dressings, in cartilage repair and in bone defects. To further aid recovery, these scaffolds can also be loaded with cells [132], growth factors [133] and antibacterial agents [134].

Isolation of STEAP1 using GG microspheres

Our research group demonstrated the suitability of GG to function as a chromatography matrix, since it is porous, hydrophilic, with high binding capacity and low unspecific adsorption [135]. Additionally, we have also shown that GG microspheres crosslinked with divalent cations can successfully capture soluble proteins and pDNA directly from complex lysates of *Komagataella pastoris* and *Escherichia coli,* respectively [136,137].

Chapter 2 - Objectives

The capture of proteins from lysates using microparticles has been successfully documented in the literature. Our research group demonstrated the aptness of nickel- and magnesium-crosslinked GG microspheres to capture soluble catechol-*O*-methyltransferase. Further reports focus several other systems for the capture of cytokines, antibodies and growth factors. However, to date and to the best of our knowledge, there is no adsorption GG-based scheme for the capture of membrane proteins.

In this manner, the goal of this work is the capture of the highly relevant membrane protein, STEAP1, using GG microspheres reinforced with divalent ions. This major objective was sectioned in three main portions, aiming to:

1. Produce GG microspheres through a water-in-oil emulsification method and crosslinking with an appropriate divalent cation.
2. Assess the proper formation of GG microspheres and confirm the incorporation of crosslinker, through semiotic microscopy, scanning electron microscopy (SEM), energy dispersive X-ray spectroscopy (EDX) and Fourier-transformed infrared spectroscopy (FTIR).
3. Application of GG microspheres batch method to capture STEAP1 from a complex *Komagataella pastoris* lysate.
4. Optimize relevant operational and environmental parameters, namely, detergent solubilization, total protein content per batch, microsphere ratios and elution profiles.

Isolation of STEAP1 using GG microspheres

Chapter 3 - Experimental

3.1. Materials

Ultrapure reagent-grade water utilized in all solutions was obtained from a Milli-Q system from Millipore/Waters. Gellan Gum (Gelzan™, Gelrite®), glass beads, bromophenol blue, 2-(N-Morpholino)ethanesulfonic acid (MES) hydrate, MES sodium salt, lysozyme and deoxyribonuclease I (DNase) were purchased from Sigma-Aldrich Co. (St. Louis, MO, USA). Tris-base, tween-20, glycine, imidazole, sodium chloride (NaCl), nickel chloride hexahydrate ($NiCl_2.6H_2O$) and methanol were obtained from ThermoFischer Scientific (Waltham, MA, USA). Calcium Chloride dihydrate ($CaCl_2.2H_2O$) and sodium dodecyl sulfate (SDS) were acquired from PanReac Applichem (Darmstadt, Germany). Bis-Acrylamide/Acrylamide 40% and NZYColour Protein Marker II were obtained from GRiSP Research Solutions (Oporto, Portugal) and NZYTech (Lisbon, Portugal), respectively. β-mercaptoethanol and *N,N,N′,N′*-Tetramethylethylenediamine (TEMED) were acquired from Merck (Darmstadt, Germany). All other reagents and supplies were of analytical grade.

3.2. Gellan microspheres production

Gellan Gum microspheres were formulated through a water-in-oil (W/O) emulsion technique formerly optimized by our group through a design of experiments approach [138]. Briefly, 20 mL of a 1.41% GG solution was heated to 90◦C, at 300 rpm for 15 min, to ensure polymer dissolution. Then, the GG solution was transferred to a syringe and was extruded dropwise. The syringe was coupled with a 21G needle and attached to a syringe pump (Harvard Apparatus, UK). The flow rate was fixed at 75 µL/min and the solution was dripped from a height of approximately 20 cm into a 100% vegetable cooking oil, previously heated to 100◦C and constant stirring rate of 750 rpm. Following, the microspheres were crosslinked with either Ca^{2+} or Ni^{2+}, by the addition of a 200 mM solution to the emulsions at room temperature for a total of 30 min, maintaining 750 rpm. Next, non-utilized oil and crosslinker fractions were removed in a vacuum filtration system with 11 µm pore size filter paper (VWR, USA), and microspheres were washed with 70% ethanol. Finally, GG microspheres were dried with water and stored in 10 mM MES buffer pH 6.2, at 4 ◦C until the completion of batch runs.

3.3. Gellan microspheres characterization

3.3.1. Semi-Optical Microscopy analysis

Average diameter of GG microspheres was calculated through semi-optical microscopy. Therefore, microspheres in a hydrated state were seated into microscope slides and visualized at 10x magnification. Six different images (n = 6) consisting of a total of 46 measurements were obtained and the mean diameter was assessed.

3.3.2. Scanning Electron Microscopy (SEM) analysis

GG microspheres surface morphology was evaluated through SEM, using a Hitachi S-3400 N microscope (Tokyo, Japan). The microspheres were placed and carefully distributed onto an aluminum support with a carbon base and frozen at -20 ◦C. Then, several magnifications were explored to acquire representative images, with a backscattered electron (BSE) 3D detector.

3.3.3. Energy Dispersive X-ray Spectroscopy (EDX) analysis

The elemental composition of formulated microspheres was assessed by energy dispersive X-ray spectroscopy to identify major chemical components and to confirm the incorporation of crosslinker ions. Hence, microspheres still frozen, post SEM snapshot acquisitions, were analyzed via a QUANTAX 400 detector (Bruker, USA).

3.3.4. Fourier-Transformed Infrared Spectroscopy (FTIR) analysis

FTIR was conducted to gauge the suitable formation of GG microspheres and to ensure divalent ion crosslinking. In order to determine these conditions, samples were lyophilized, and spectra were acquired using a FTIR spectrophotometer (Nicolet iS10, ThermoFischer Scientific) for both GG powder and GG microspheres. Spectra were collected operating in ATR mode with an average of 120 scans on wavenumbers ranging from 400-4000 cm^{-1}, at a resolution of 32 cm^{-1}, and the equipment was managed in the OMNIC Spectra software (ThermoFischer Scientific).

3.4. Mini-bioreactor production of recombinant human STEAP1

The production of recombinant human STEAP1 was performed as described by Duarte and coworkers [49]. In brief, *Komagataella pastoris* X-33 Mut^+ were selected at 30◦C on YPD plates. Then, a single colony was transferred to Erlenmeyer shaker flasks containing 100 mL of BMGH medium. Pre-fermentation culture was grown overnight at 30◦C and 250 rpm, until optical density reached a value between 5-6. Next, an appropriate volume was collected in an equivalent amount to an OD_{600nm} of 0.5 and was

placed into 750 mL reactor vessels with 250 mL of BSM medium supplemented with SMT and Zeocin™. STEAP1 biosynthesis process was divided into 3 main stages. In the first stage, a standard batch took place until full depletion of glycerol, which is detected by a sharp rise in dissolved oxygen. Second, in order to improve biomass levels, a glycerol fed-batch phase was carried out for 2h. The fed-batch was coupled with a 1h transition phase, characterized by the injection of methanol into the feed to accustom fermenter culture to a new carbon source. Finally, performing a methanol feed strategy induced the AOX promoter and stimulated the expression of recombinant human STEAP1 (rhSTEAP1). The cells were separated by centrifugation for 10 min at 1500g and 4◦C.

3.4.1. STEAP1 recovery

In order to extract STEAP1, pelleted cells were resuspended in lysis buffer (50 mM Tris, 150 mM NaCl, pH 7.8 supplemented with a protease inhibitor cocktail). Lysozyme (1 mg/mL) was added to the mix, and enzymatic digestion took place at room temperature for 15 min. Then, the mix was added to a falcon containing glass beads in a ratio of 1:2:2 (1g biomass, 2 mL of lysis buffer and 2g of beads). Partially digested cells were further mechanically lysed through seven 1 min vortex cycles, interleaved by 1 min incubations on ice. Next, both cell debris and beads were separated by a 5 min 500g centrifugation at 4◦C. The protein pellet was resuspended in lysis buffer supplemented with DNase (1 mg/mL) and centrifuged at 16000g for 30 min at 4◦C. Following discard of the supernatant, the pellet was resuspended in the binding buffer correspondent to the following batch method capture step.

3.5. Batch method for the STEAP1 capture

The batch method employed for the capture of rhSTEAP1 was adapted from the batch described by Gomes and coworkers for the capture of the soluble isoform of catechol-*O*-methyltransferase [136]. First of all, GG microspheres were equilibrated with the proper buffer for the capture step. The batch itself was represented by three main stages: Binding, Washing and Elution. The binding or capture step was initiated by the addition of 6 mL of diluted lysate to an appropriate volume of microspheres, ranging from 20 to 35 mL. This step was carried out for 4h, at 4◦C under gentle tube agitation, followed by a centrifugation at 500g for 8 min and recovery of the supernatant. Ensuing washing and elution steps followed the same workflow with a total cycle length of 1h. The batch was applied to calcium- and nickel-crosslinked GG microspheres. For calcium, an ionic exchange strategy was chosen, by manipulation of pH and ionic strength (ranging from 6.2 to 11 and 0 mM to 500 mM NaCl, respectively) to recover STEAP1. In regards to nickel, an affinity strategy mimicking Immobilized Metal Affinity Chromatography

(IMAC) was used, wherein STEAP1 would bind to the microspheres through its 6xHis-Tag and be eluted by several increasing imidazole concentrations, ranging from 5 mM to 500 mM. Fractions recovered from each stage were concentrated and desalted with Vivaspin concentrators (10,000 MWCO) and stored at 4◦C until further purity or immunoreactivity analysis.

3.6. Co-Immunoprecipitation

Clarified and pre-purified samples recovered from the batch method were coupled with a Co-Immunoprecipitation (Co-IP) polishing step. Co-IP was performed following manufacturer's protocol for Protein A/G PLUS-Agarose Immunoprecipitation Reagent (sc-2003, Santa Cruz Biotechnology, Dallas, TX, USA) with slight modifications. Succinctly, samples containing STEAP1 were incubated for 1h at 4◦C with anti-STEAP1 mouse monoclonal antibody (B-4, Santa Cruz Biotechnology, Dallas, TX, USA). Then, an appropriate volume of agarose beads was added and overnight incubation under constant stirring was conducted. The formed conjugated complexes were recovered by centrifugation at 1000g for 5 min at 4◦C. After discarding the supernatant and washing the conjugates with PBS, the pelleted complexes were resuspended in electrophoresis loading buffer (refer to section 3.7). The agarose beads were removed from the antibody-STEAP1 complexes by the combinatory effect of sample boiling at 100◦C and 5% (v/v) β-mercaptoethanol .

3.7. SDS-PAGE and Western Blot

Reducing SDS-Polyacrylamide Gel Electrophoresis (SDS-PAGE) was performed according to the Laemmli method [139]. Briefly, samples recovered from batch runs were boiled for 5 min at 100◦C and resolved in duplicate 12.5% SDS-PAGE gels at 120V. One gel was stained with Coomassie blue, whereas the other was transferred into a PVDF membrane (GE Healthcare,Wauwatosa, WI, USA) at 750 mA for 90 min at 4◦C. A 5% non-fat milk solution was used to block the membranes for 1 h, followed by overnight incubation with anti-STEAP1 mouse monoclonal antibody 1:300. The next day, membranes were incubated for 2 h with goat anti-mouse IgG-HRP 1:5000 (sc-2005, Santa Cruz Biotechnology, Dallas, TX, USA), and STEAP1 was detected with ChemiDoc™ MP Imaging System after incubation with ECL substrate (Bio-Rad, Hercules, CA, USA).

3.8. Total protein quantification

The total protein content in the lysates and samples was quantified by Pierce BCA Protein Assay Kit (ThermoFischer Scientific), following manufacturer's protocol with slight modifications. Briefly, 19 µL of water, 1 µL of sample and 80 µL of working reagent (50:1; A:B) were added to a 96 well microplate, in triplicate. The volume in the wells was homogenized by gentle shaking of the microplate and was incubated in the dark at 37◦C for 30 mins. Subsequently, absorbance values were read at 562 nm in an xMarkTM Microplate Absorbance Spectrophotometer (Bio-Rad, USA). Calibration curves were built for MES and Tris buffer, using Bovine Serum Albumin (BSA) as standard, with concentrations ranging from 0 to 1.2 mg/mL (MES - Figure 8 ; Tris - Figure 9).

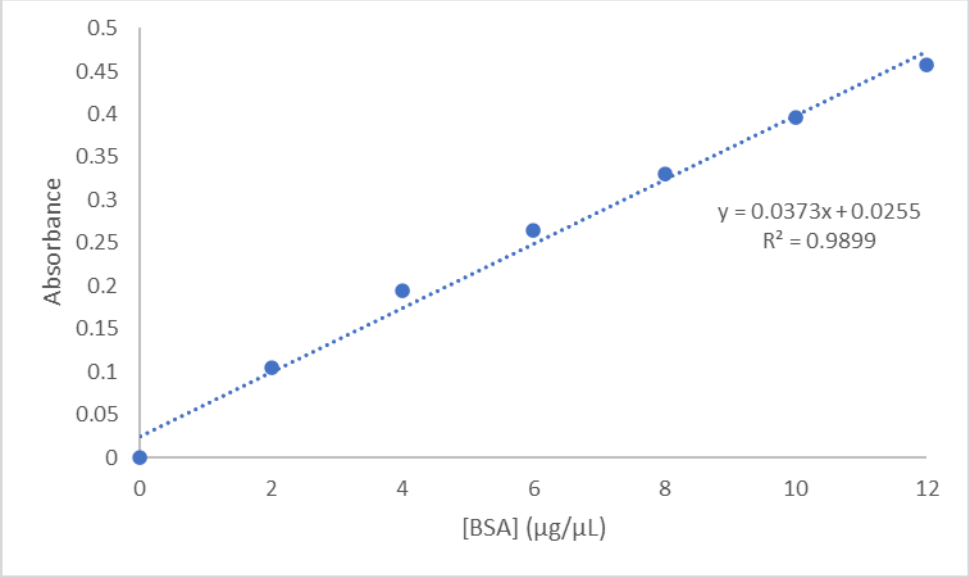

Figure 8. Standard curve of BSA concentration *vs* absorbance at 562 nm for MES buffer.

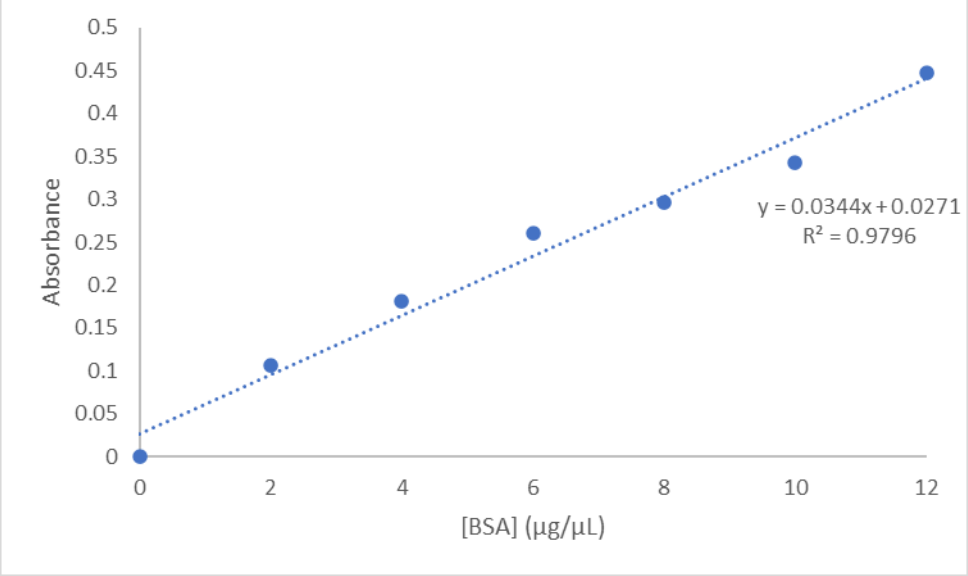

Figure 9. Standard curve of BSA concentration *vs* absorbance at 562 nm for Tris buffer.

Isolation of STEAP1 using GG microspheres

Chapter 4 – Results and Discussion

4.1. GG microspheres production

Emulsion-based techniques have become a prevalent production method for microspheres and microcapsules for a variety of applications. They can be divided into water-in-oil (W/O), oil-in-water (O/W) or more intricate systems, such as W/O/W or O/W/O, among others [140]. W/O emulsions occur when blending two immiscible liquids, an oil phase with an aqueous phase, which usually is the polymeric solution. Often, the aqueous solution is dispersed in the continuous organic phase. Upon reaching equilibrium, gel formation is initiated by either cooling, addition of ions, acids, bases or cross-linking agents [140,141]. O/W emulsions function in the same manner, but the dispersed and continuous phases are reversed. After curing, beads are recovered and washed. Emulsion methods produce microspheres with "large" diameters and large size distribution. On the other hand, these techniques are quite advantageous for industrial applications, as they are easy to scale-up [141]. As previously discussed, the GG gelation process is dependent on cooling and introduction of multivalent cations to induce helical aggregation and subsequent flocking to junction zones, to form the higher structured branched 3D network [94,100]. GG gelation requirements seem to merge seamlessly with the emulsion methodology.

Here, GG microspheres were produced by a W/O emulsification method, which had been previously optimized by our research group to yield microspheres with the lowest mean diameter possible (Figure 10; [138]), as described in section 3.2. These GG microspheres were reinforced with 2 different ions. First, nickel was selected since our research group had determined this divalent ion granted the best capture and purification for the soluble COMT, through a similar batch approach [136]. Second, calcium was selected because it is the most used GG crosslinker in the literature, with proven results in drug delivery [142], bioremediation [116] and biosynthesis [118,119]. Since nickel-crosslinked GG microspheres had already been extensively characterized by our group in previous work, they were excluded from further characterization. In contrast, calcium-crosslinked microspheres produced through W/O emulsion were characterized through semi-optical microscopy, SEM, EDX and FTIR to assess size, morphology and chemical composition, respectively.

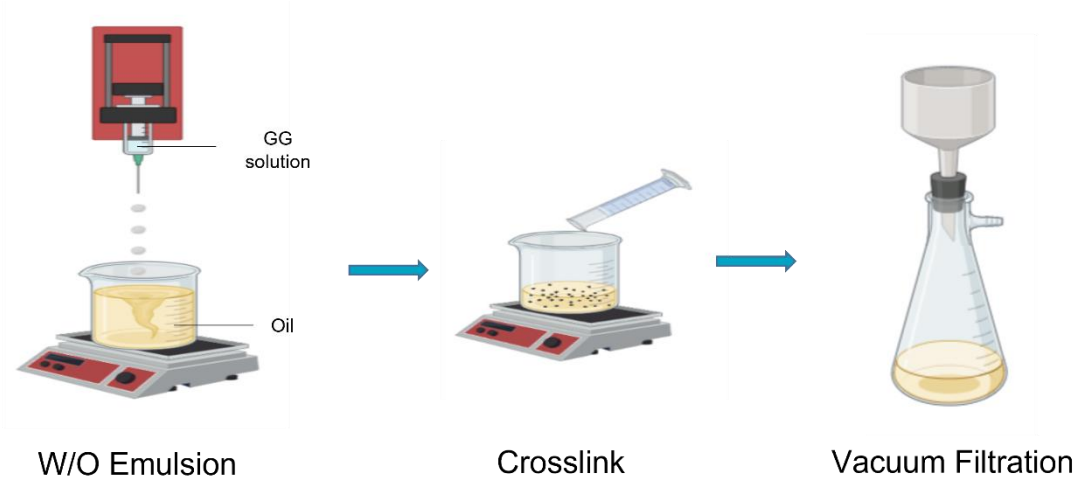

Figure 10. Schematic Representation of GG microspheres production through W/O emulsion.

4.2. GG microspheres characterization

4.2.1 Semi-optical microscopy analysis of GG microspheres

Gellan gum microspheres were analyzed through semi-optical microscopy in order to assess the mean diameter. So, six images (n = 6) were acquired with a total of 46 measurements for calcium-crosslinked GG microspheres. Representative snapshots can be found in Figure 11 and measurements are displayed in Table 4. The mean diameter obtained for calcium-crosslinked GG microspheres was of 330.37 ±11.38 μm, whereas nickel-crosslinked GG microspheres had previously been described with a mean diameter of 239.06 ± 5.43 μm [136]. Both values are lower than microspheres produced through the standard ionotropic gelation method, which can often produce beads in the mm range [109,143]. This result is relevant, since with a decrease in size, it is expected an increase of surface contact area, which could benefit the adsorption capacity of GG microspheres [88]. Abbas and Marihal reported calcium-crosslinked GG beads with sizes between 24.86 ± 1.34 μm and 52.42 ± 1.03 μm produced through a similar W/O emulsion approach. However, their purpose was the nasal administration of Almotriptan, and intranasal delivery requires lower size particles, which is why they employed 1800 rpm in the extrusion process [142]. In this work, going lower in size could be detrimental due to colloidal instability [89], which could compromise the adsorption protein profiles of GG adsorbent microspheres. Furthermore, from the get-go nickel-crosslinked GG microspheres have nearly 100 μm less in total size, which could mean they have higher potential to capture STEAP1 in the batch method, due to increase in specific surface area.

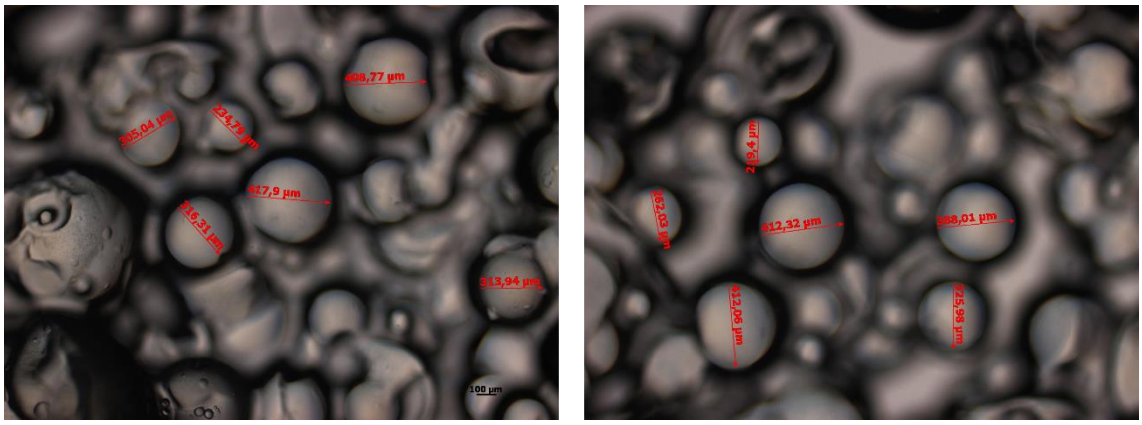

Figure 11. Representative snapshots of calcium-crosslinked GG microspheres obtained through semi-optical microscopy.

Table 4. Measurement and mean diameter obtained for calcium-crosslinked GG microspheres.

Snapshot	Measurements (µm)		Average Diameter (µm)
1	305.04	417.9	332.79
	234.79	408.77	
	316.31	313.94	
2	262.03	412.06	336.63
	219.4	388.01	
	412.32	325.98	
3	388.73	358.53	350.75
	245.68	369.99	
	318.71	507.78	
	366.53	156.94	
	443.87		
4	262.94	328.43	323.18
	406.04	250.02	
	305.84	302.48	
	406.52		
5	363.32	396.33	323.09
	536.6	404.31	
	418.37	359.51	
	207.05	204.25	
	148.4	231.12	
	284.73		
6	244.46	351.61	315.78
	255.98	392.02	
	391.75	287.67	
	286.96		
Total		**330.37 ± 11.38**	

4.2.2 SEM analysis of GG microspheres

The morphology and geometry of GG microspheres was determined by SEM. Snapshots collected for calcium-crosslinked GG microspheres are represented in Figure 12. Snapshots for nickel-crosslinked GG microspheres were adapted from [136] and are illustrated in Figure 13. Both types of microspheres present a consistent and uniform structure with spherical shape. In regards to calcium-crosslinked GG microspheres, at

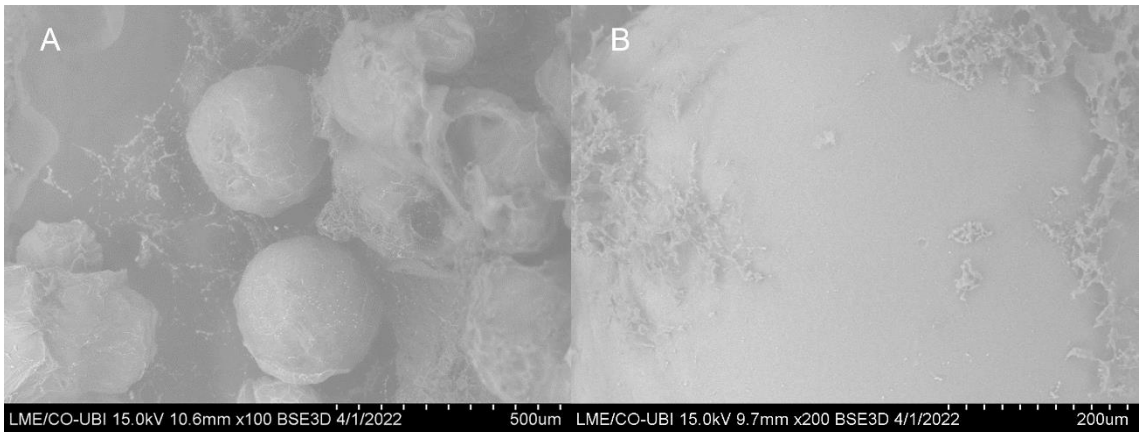

Figure 12. SEM images of calcium-crosslinked GG microspheres at x100 magnification (A) and x200 magnification (B).

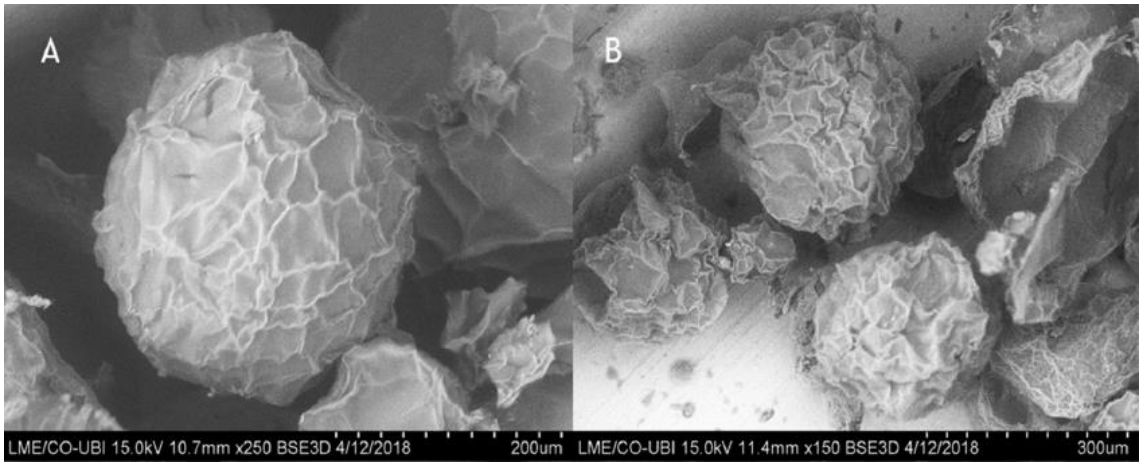

Figure 13. SEM images of nickel-crosslinked GG microspheres at x100 magnification (A) and x200 magnification (B); Adapted from [136].

first glance (x100 magnification; Figure 12. A) it appears that the microspheres are slightly rugous, however when taking a closer look at x200 magnification, it becomes evident that the surface is in fact smooth with no apparent pores, cavities or cracks. In turn, nickel-crosslinked GG microspheres present obvious rugosity and some cavities. Our group has already reported the morphology of magnesium- and copper-crosslinked GG microspheres and their morphology is closer to that of the nickel-GG microspheres, which might suggest a differential effect of calcium ions for GG topology [136,137].

Similar to calcium-crosslinked beads, nickel-crosslinked GG microspheres are also lacking in large pores, which suggest that STEAP1 binding in batch runs should occur almost exclusively at the surface of microspheres. Moreover, as opposed to GG beads produced by Bhattacharya and collaborators [144] and by Patil and coworkers [145] through ionotropic gelation, GG microspheres produced through W/O emulsion are absent of sharp edges, which reduces the possibility of occurrence of the "egg-beater effect", during batch runs [83]. In contrast, morphology of GG microspheres produced by Abbas and Marihal through W/O emulsion is in accordance with presented results in Figures 12 and 13 [142].

4.2.3 EDX analysis of GG microspheres

In sequence to SEM analysis, GG microspheres were subjected to EDX in order to uncover the main elemental composition of GG formulations and to confirm the success of the crosslinking step. Obtained results are listed in Table 5, being expressed in normalized concentration by weight percentage (C norm. [wt%]) and in atomic concentration by atomic percentage of each element (C atom. [at%]).

Table 5. Elemental Composition of GG microspheres through EDX.

Element	Calcium-crosslinked GG microspheres		Nickel-crosslinked GG microspheres	
	C norm. [wt%]	C atom. [at%]	C norm. [wt%]	C atom. [at%]
Carbon	31.87	38.72	39.19	47.13
Oxygen	66.54	60.70	57.73	52.12
Calcium	1.59	0.58	-	-
Nickel	-	-	3.08	0.76
Total	100.0	100.0	100.0	100.0
Ref.	-		[136]	

GG is composed of repeating carbohydrate units (β-D-glucose, β-D-glucuronic acid and α-L-rhamnose) [96,97], so it is not a surprise that >95% of its constitution is carbon and oxygen. Both types of microspheres incorporated the crosslinking ions, confirming success of the crosslinking stage, however nickel-crosslinked GG microspheres seem to have nearly a two fold higher ion% (C norm. [wt%] : 1.59% *vs* 3.08%; calcium *vs* nickel). Interestingly, when comparing calcium-, nickel-, magnesium- and copper-crosslinked GG microspheres produced through the same W/O emulsion by weight normalized crosslinker percentage, it appears that transition metals ions are integrated at higher percentages than alkaline earth metals in the following order: Copper > Nickel > Calcium > Magnesium (9.33 > 3.08 > 1.59 > 1.04) [136,137]. The

higher %uptake of crosslinker can result in tighter and more compact network gels, which in turn, might justify the smaller mean diameter observed for nickel-crosslinked GG microspheres [109].

4.2.4 FTIR analysis of GG microspheres

FTIR analysis was conducted to evaluate the chemical profile of GG after microsphere formulation and to detect the interaction between GG and crosslinker ions. As a result, FTIR spectra were obtained for both GG powder and calcium-crosslinked GG microspheres and are represented in Figure 14. The GG powder spectrum showed characteristic peaks at 3333 cm^{-1}, assigned to the stretching of the hydroxyl groups (-OH) from glucopyranose rings. Furthermore, the peak at 2912 cm^{-1} is attributed to -CH vibrations. Both peaks at 1605 cm^{-1} and 1400 cm^{-1}, correspond to carboxylate anions (COO^-). The peak at 1026 cm^{-1} is related to hydroxylic C-O stretching [108,146]. The calcium-crosslinked GG microspheres spectrum exhibited analogous peaks with slight variations in absorbance. For instance, the rise of a peak at 1743 cm^{-1} and the disappearance of the peak at 1400 cm^{-1} is indicative of an interaction between the carboxyl groups from GG with calcium ions. This finding is in line with the theoretical gelation process, wherein divalent cations form chemical bonds with two carboxylate groups in the glucuronate moiety [96]. Further, absorbance loss of the peak at 3333cm^{-1} might suggest that calcium can also bind in the glucopyranose rings of glucose. It appears that multiple points of GG are involved in the coordination and binding of calcium ions and the differences in FTIR spectra seem to verify EDX findings and corroborates the incorporation of calcium as a crosslinker in gellan.

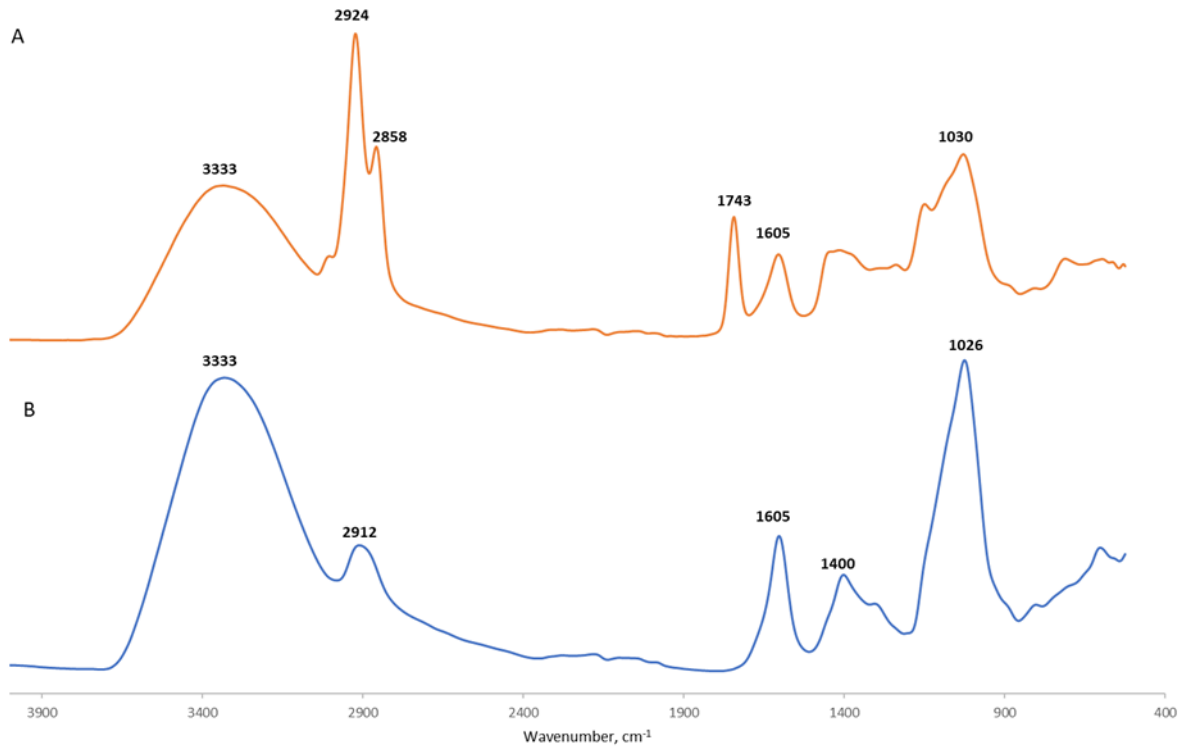

Figure 14. FTIR Spectra (Absorbance *vs* Wavenumber) of calcium-crosslinked GG microspheres (A) and GG powder (B).

4.3. Batch method for the capture of STEAP1

The batch method consists of three main sequential steps: Binding, Washing and Elution. To capture STEAP1 through the batch method, we planned to take advantage of the high STEAP1 isoelectric point of ~9.2 (Compute pI – Expasy; SIB) to isolate it from the rest of the *Komagataella pastoris* proteome with an average isoelectric point of 6.46 (Proteome-pI database; [147]). The listed *Komagataella pastoris* strain in the Proteome-pI database is strain GS115, and although we used *Komagataella pastoris* X33 Mut^{+} we did not expect major changes in overall proteome pI, since X33 is derived from strain GS115 [148]. The initial batch approach for both calcium- and nickel-crosslinked microspheres was an ionic exchange strategy. The initial binding step was designed at pH 6.2, wherein GG would always present a negative charge (pKa = 3.5; [149]) and STEAP1 would present a net positive charge and adsorption would take place mostly by electrostatic attraction, by incubation at 4◦C for 4h. Then, a centrifugation step of 500g 8 min would be conducted to recover the supernatant, representing the protein fractions that did not bind to GG microspheres. Subsequently, 10 mM Tris buffer at pH 8 would be added and incubation for 1 h would take place. Since the average pI of *K. pastoris* is 6.46, at pH 8 it was expected for a great deal of impurities to be removed from the bound protein fraction. Next, at pH 9.2 or pH >9.2 a clarified and partially purified STEAP1

fraction would be recovered either by charge neutralization or charge repulsion, respectively. Indeed, this strategy was employed in our *Initial Batch* and can be seen in Figure 15. Curiously, in all batch steps there was no STEAP1 migration in SDS-PAGE gels and only large molecular weight bands >245 kDa were observed. This is in contrast to initial control lysates, which distribute STEAP1 mostly in ~63 kDa, but also in ~48 kDa and ~35 kDa [73], and since the GG microspheres were the only new component added, we can only assume that STEAP1 had a tendency to form complexes with GG microspheres, and in turn, potentially aggregate. Tsuji had previously reported that sample boiling previous to Western blot for other membrane proteins (DMT1 and ferroportin 1) resulted in aggregation and in similar large molecular weight bands [150]. To discard this option, samples were injected into SDS-PAGE gels without boiling by leaving them at room temperature for 5 min (Figure 16). As can be seen, the lysate that was boiled at 100 ◦C for 5 mins presents STEAP1 at ~63 kDa, whereas the samples from the batch method present the same large molecular weight bands, with or without boiling, which suggests that this phenomenon occurs during the batch runs, and it is not dependent on temperature aggregation when preparing the samples for analysis by Western-Blot. Nevertheless, to improve STEAP1 stability during batch runs a series of optimizations were in order.

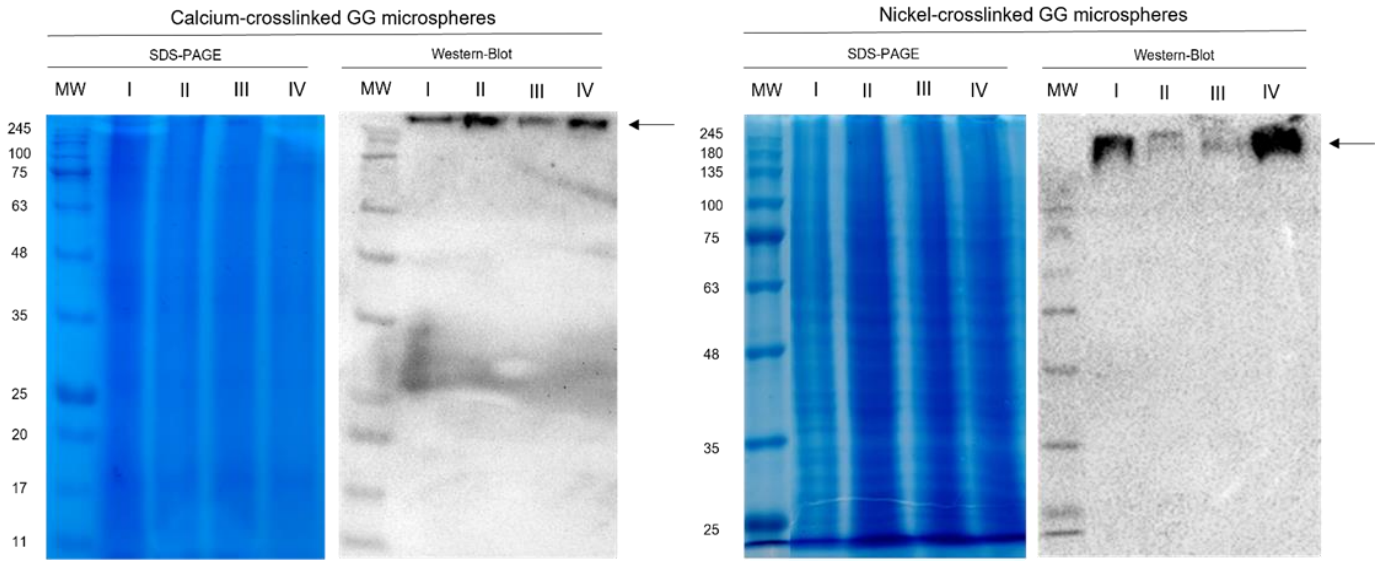

Figure 15. SDS-PAGE and Western-blot of the recovered supernatants from the *initial batch* for both calcium and nickel crosslinked microspheres (35 mL GG microspheres for both ions represented). MW – molecular weight; I – Sample that did not bind to GG microspheres at 10 mM MES pH 6.2; II – Wash step with 10 mM Tris pH 8; III – Elution step with 10 mM Tris pH 9.2; IV – Elution Step with 10 mM Tris pH 11; Arrows indicate STEAP1 complexes.

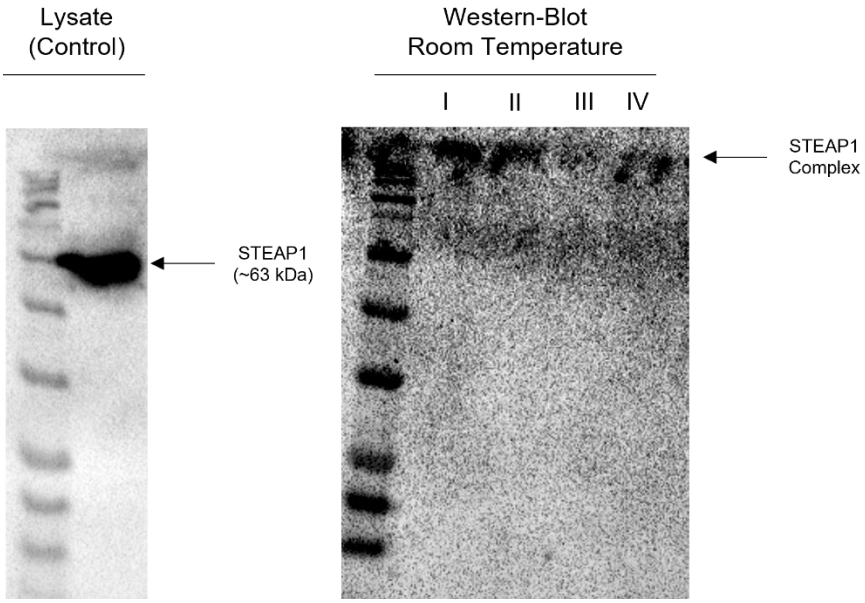

Figure 16. Western-blot of a representative control lysate and of the recovered supernatants from the *initial batch* for calcium crosslinked microspheres (35 mL GG); I – Sample that did not bind to GG microspheres at 10 mM MES pH 6.2; II – Wash step with 10 mM Tris pH 8; III – Elution step with 10 mM Tris pH 9.2; IV – Elution Step with 10 mM Tris pH 11.

4.3.1 Optimizations of the STEAP1 batch method

Solubilization of membrane proteins is essential for appropriate stabilization and conformation [151,152]. In this manner, a handful of mild nonionic detergents that our group had previously tested for STEAP1 solubilization were selected (unpublished data). These nonionic detergents were chosen because they are non-denaturant and retain biological function and native conformation of membrane proteins, as opposed to zwitterionic and ionic detergents which are harsher and can lead do deactivation or denaturation of membrane proteins, respectively [151,153]. So, after the cell recovery process described in the experimental section, pelleted lysate acquired after the 16000g centrifugation was resuspended in 10 mM MES buffer at pH 6.2 with addition of 0.1% (v/v) of either of 5-Cyclohexyl-1-Pentyl-β-D-Maltoside (CYMAL-5), n-Decyl-β-D-Maltoside (DM), Nonidet P-40 (NP-40) or Genapol X-100 (GEN). Results are depicted in Figure 17.A, and it is clear that DM solubilized STEAP1 showed the highest band signal. By signal intensity, CYMAL-5 is better than NP-40, which subsequently is better than GEN in STEAP1 solubilization. This indicates that Maltoside-based detergents are better at solubilizing the target protein. In fact, the differential performance between CYMAL-5 and DM could be attributed to different Critical Micellar Concentrations (CMC). For DM this value equates to 0.087%, while for CYMAL it is equal to 0.12% (Anatrace D322 and C325; CMC in water). The fact that we were working at 0.1% (v/v), above DMs CMC, definitely benefited it from a solubilization standpoint. Furthermore, it is not good practice to include excessive amounts of detergent in purification steps, as

this can influence subsequent biointeraction and structural characterization protocols. For instance, detergents present in protein samples can interact with dyes in thermofluor assays [154]. Therefore, DM was considered the best detergent for solubility purposes and was included at 0.1% (v/v) in all buffers for subsequent batch runs.

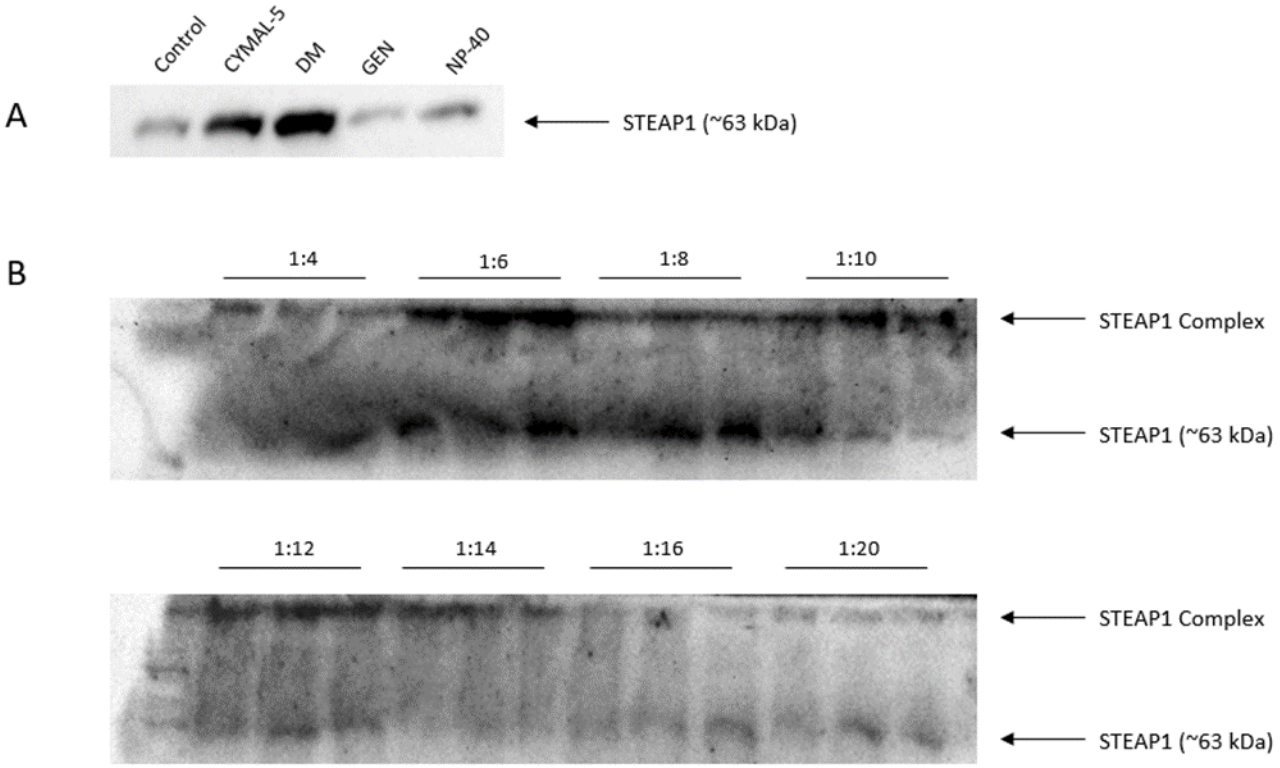

Figure 17. Detergent Screening for STEAP1 solubilization; lysates were resuspended in 10 mM MES pH 6.2 with addition of 0.1% of CYMAL-5, DM, GEN or NP-40; control represents unsolubilized lysate sample (A) and *Initial batch* lysate dilution screening following a simple three step sequence per dilution: Binding – 10 mM MES pH 6.2; Washing – 10 mM Tris pH 8; Elution – 10 mM Tris pH 11 (B).

When planning the *Initial Batch*, the initial lysate dilution of 1:4 was adapted from Gomes and coworkers [136]. However, in the present work, the production was done in a bioreactor, which yields 4-5x more total protein concentration, with an average of ~43 mg/mL. And since large molecular weight bands exceeding 245 kDa were found, it was necessary to evaluate if the initial lysate concentration was too high and led to aggregation. Thus, a shortened batch was carried out with a total of 3 steps with the following conditions: Binding – 10 mM MES pH 6.2; Washing – 10 mM Tris pH 8; Elution – 10 mM Tris pH 11. This 3 steps batch was applied to varying lysate dilutions from 1:4 to 1:20 (~10.75 to ~2.15 mg/mL of total protein concentration). The results are depicted in Figure 17.B. Indeed, similar to the *Initial Batch* a dilution of 1:4 forms large molecular weight complexes and is inadequate to proper analysis. Starting from 1:6 (~7 mg/mL) forward, some migration of STEAP1 was observed to the ~63 kDa molecular weight matching the control lysate. Moreover, these large complexes are present

throughout the whole dilution range, even at 1:20 (~2.15 mg/mL). This is odd, since a 1:20 dilution should be dilute enough to not cause such meaningful aggregation. In light of this information, we began to suspect that aggregation could play a part in the formation of the large molecular weight complexes but was not the main cause. Indeed, these results seem to indicate the formation of a polysaccharide-protein interaction. Nevertheless, since a dilution of 1:6 is sufficient to migrate STEAP1 to the appropriate molecular weight in Western Blots and since it allows us to process the highest amount of protein per batch run (~7 mg/mL), this was selected as the appropriate starting protein concentration. Application of parameters determined from both the detergent and lysate dilution screenings in combination in an *Optimization Batch* can be seen in Figure 18. When applying optimized parameters, the great majority of STEAP1 was bound to the microspheres at pH 6.2 in 10 mM MES buffer, with minimal losses in the washing step at pH 8 in 10 mM Tris. The clarified STEAP1 fraction was eluted at pH 9.2 in 10 mM Tris (line III), by charge neutralization. However, charge neutralization was not enough to recover all of STEAP1, since a smaller fraction was only recovered at pH 11 in 10 mM Tris (line IV), by charge repulsion. Moreover, up until this point 2 distinct microsphere ratios were being tested. On one side, a ratio of 20 mL GG microspheres to 6 mL binding buffer and on the other, 35 mL GG microspheres to 6 mL binding buffer. It becomes clear when analyzing the data that the samples recovered from the batch with 35 mL of calcium-crosslinked GG microspheres exhibit much stronger signal and better binding results. For this reason, this condition was selected for further batch analysis. Moreover, STEAP1 was found divided between ~35, ~48 and ~63 kDa. However, this is not a concern, since it has previously been reported that the small aggregates at ~48 and ~63 kDa are derived from the upstream production steps [73]. Kim and coworkers went as far as to refer to them as the dimeric and trimeric STEAP1 [23]. Another relevant observation is that although complexation was diminished, it is still present, and it seems to mimic the intensity of total STEAP1 concentration in each batch step.

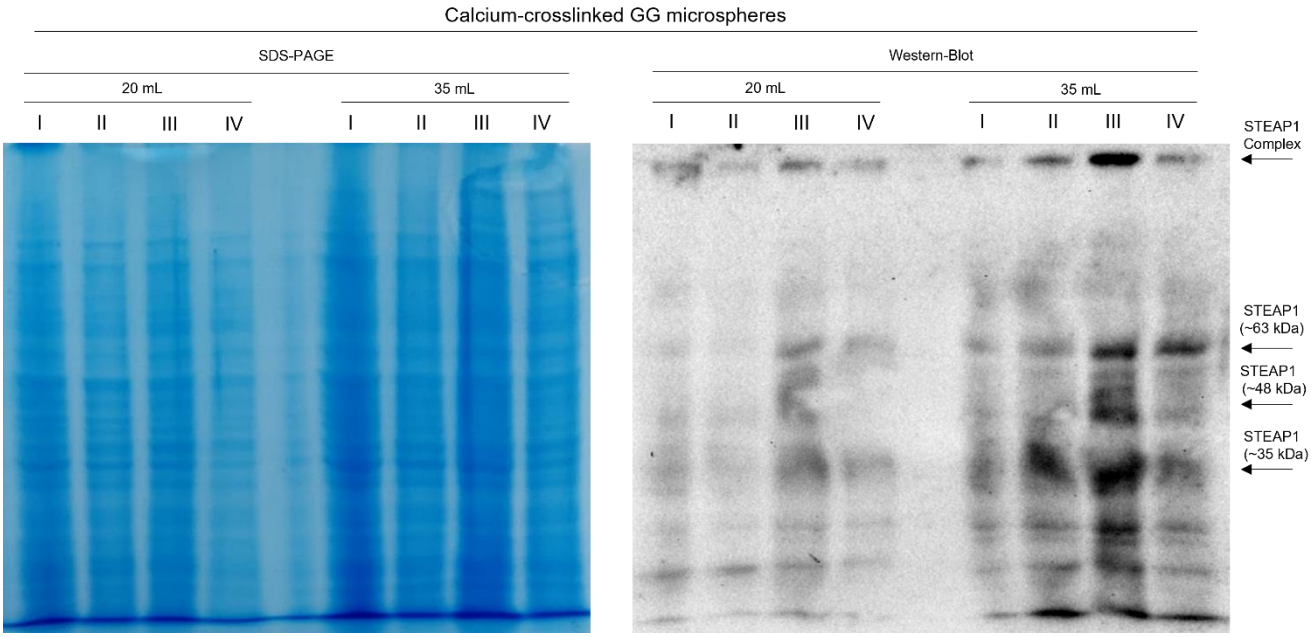

Figure 18. SDS-PAGE and Western-blot of the recovered supernatants from the *Optimization Batch* for calcium-crosslinked GG microspheres (20 and 35 mL GG microspheres); I – Sample that did not bind to GG microspheres at 10 mM MES pH 6.2; II – Wash step with 10 mM Tris pH 8; III – Elution step with 10 mM Tris pH 9.2; IV – Elution Step with 10 mM Tris pH 11.

4.3.2. Affinity strategy for STEAP1 capture

In the *Optimization Batch*, similar results were observed for both types of microspheres (Appendix 1), so it would be redundant to carry out the same approach for both calcium- and nickel-crosslinked GG microspheres. As an alternative, nickel-crosslinked GG microspheres were used in an affinity strategy to capture STEAP1 through its His-Tag, mimicking interaction mechanisms of a traditional IMAC column, wherein addition of imidazole to the elution buffers would act as a competing agent to the Histidine residues and promote STEAP1 desorption. In this assay, pH was fixed at the pI of ~9.2, to eliminate as much as possible any electrostatic interaction. As previously discussed, some degree of complexation was still present even after the optimization of batch parameters. Therefore, a moderate amount of salt was added to the batch buffers, in an attempt to stimulate a slight salting-in effect to promote the stabilization of STEAP1. A similar salt stabilization methodology was previously reported for Rhodopsin, a structurally similar transmembrane protein [155]. Furthermore, the introduction of salt would also assist in blocking electrostatic interactions in the binding step. Internal data acquired from the purification of STEAP1 in a nickel IMAC column following an imidazole stepwise profile (10 mM; 50 mM; 175 mM; 300 mM and 500 mM of imidazole) demonstrated that STEAP1 would be eluted at 175 mM imidazole and higher (unpublished data). Taking this into consideration, a *four-step affinity batch* was constructed with a binding step consisting of 10 mM Tris pH 9.2 supplemented with 150 mM NaCl and 5 mM imidazole. This small imidazole concentration was added to prevent binding of host proteins with a large amount of exposed histidine residues [156]. Next,

three consecutive elution steps were included with increasing amounts of imidazole concentration, specifically, 175, 300 and 500 mM imidazole. Results from the *four-step affinity batch* are displayed in Figure 19. It appears that the great majority of STEAP1 was bound to the nickel-crosslinked GG microspheres through an affinity approach, and alike to the IMAC profile, STEAP1 starts eluting at 175 mM imidazole. Though, 175 mM imidazole appears to not be enough to elute all of STEAP1 since the target protein is distributed evenly throughout all elution steps of 175, 300 and 500 mM imidazole.

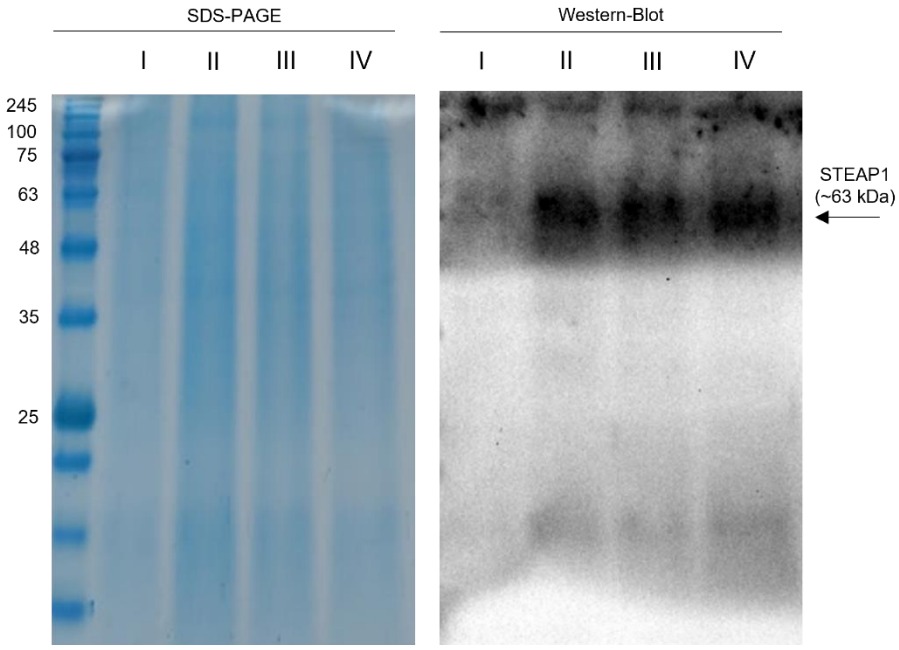

Figure 19. SDS-PAGE and Western-blot of the recovered supernatants from the *four-step affinity batch* with nickel-crosslinked GG microspheres; I – Sample that did not bind to GG microspheres at 10 mM Tris pH 9.2 with 150 mM NaCl and 5 mM imidazole; II – Wash step with 10 mM Tris pH 9.2 with 150 mM NaCl and 175 mM imidazole; III – Elution step with 10 mM Tris pH 9.2 with 150 mM NaCl and 300 mM imidazole; IV – Elution step with 10 mM tris pH 9.2 with 150 mM NaCl and 500 mM imidazole.

Furthermore, when looking at SDS-PAGE lanes II-IV, there is still quite a high density of endogenous host proteins being bound through the affinity approach, which was not expected. In order to address both issues, a *three-step condensed batch* was developed with the following scheme: Binding – 10 mM Tris pH 9.2 with 150 mM NaCl and 5 mM imidazole; Washing – 10 mM Tris pH 9.2 with 150 mM NaCl and 50 mM imidazole; Elution – 10 mM Tris pH 9.2 with 150 mM NaCl and 500 mM imidazole. With these conditions, it was expected to still bind all of STEAP1, wash non-specific bound endogenous impurities with 50 mM imidazole and then elute all of STEAP1 in a single step with 500 mM imidazole, which was the highest imidazole concentration in the *four-step affinity batch*. Results from the condensed batch are highlighted in Figure 20. In resemblance to the previous four-step batch, nearly all of STEAP1 was bound. However, at a 50 mM imidazole concentration over half of STEAP1 was being eluted, which is quite a distinct profile than what is observed in an IMAC column. This suggest that a 3.5x lower

concentration of imidazole is sufficient to elute STEAP1 in a system with adsorbent GG microspheres as opposed to the packaging material in a HisTrap™ FF Crude column. In addition, this step was not able to fully recuperate the target protein, as quite a great deal of STEAP1 is still recovered with 500 mM imidazole. However, the complexation seems to be nearly completely eliminated in the affinity strategy. Nonetheless, some degradation was observed for the first time in all batch runs, represented by the bands obtained at ~17 kDa. The combinatory effect of not being able to recuperate pre-purified STEAP1 in a single step and the occurrence of large degradation of samples lead us to exclude the affinity strategy from further purification assays.

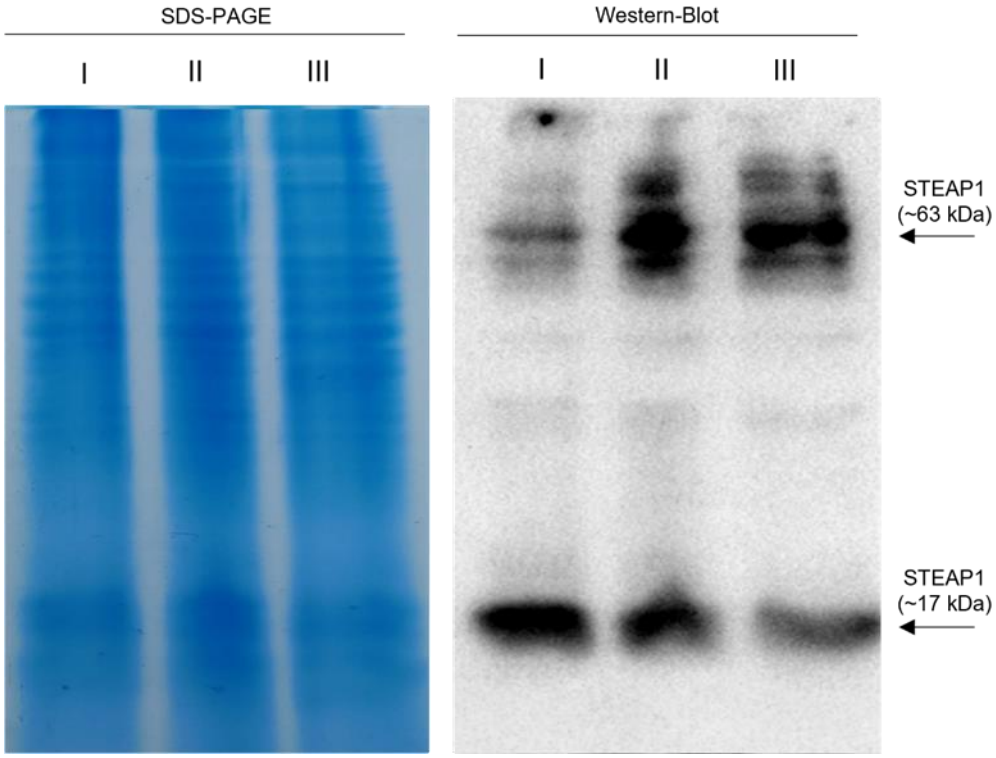

Figure 20. SDS-PAGE and Western-blot of the recovered supernatants from affinity batch with nickel-crosslinked GG microspheres; I – Sample that did not bind to GG microspheres at 10 mM Tris pH 9.2 with 150 mM NaCl and 5 mM imidazole; II – Wash step with 10 mM Tris pH 9.2 with 150 mM NaCl and 50 mM imidazole; III – Elution step with 10 mM Tris pH 9.2 with 150 mM NaCl and 500 mM imidazole.

4.3.3. Ionic strategy for STEAP1 capture

The ionic strategy using calcium-crosslinked GG microspheres displayed in the *Optimization Batch* was further developed. Similar to the affinity strategy, a moderate amount of salt was added to buffers to promote the salting-in effect. However, instead of a fixed amount of 150 mM NaCl in each step, NaCl levels were controlled in a manner that allowed the streamline of the batch process, mimicking the stepwise elution profile of a standard ion exchange chromatography. Indeed, in the *Optimization Batch,* it was observed that the majority of STEAP1 eluted at pH 9.2 (Figure 18). However, there was still a fraction that was only eluted at pH 11, by charge repulsion. In order to recover all

of STEAP1 in a single step, a slightly modified batch was developed. Here, binding took place with 10 mM MES pH 6.2, without salt. Next, a single washing step at pH 8 with 100 mM NaCl in 10 mM Tris buffer was performed, and lastly, two elution steps at pH 11, one with 100 mM NaCl and another with 500 mM NaCl in 10 mM Tris. This would allow us to analyze if pH is the driving force of the STEAP1 elution or if it is not enough, requiring higher salt amounts. Results are displayed in Figure 21. Similar to the *Optimization Batch*, most of STEAP1 is bound to the GG microspheres and a very minimal loss is

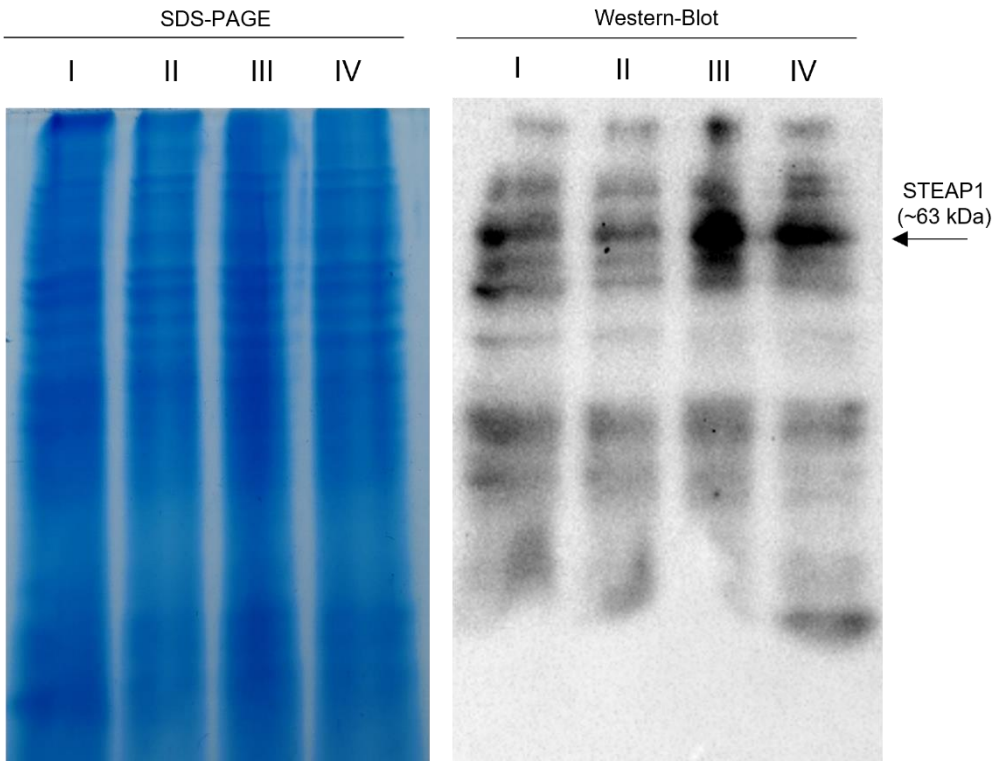

Figure 21. SDS-PAGE and Western-blot of the recovered supernatants from the ionic exchange batch for calcium-crosslinked GG microspheres; I – Sample that did not bind to GG microspheres at 10 mM MES pH 6.2; II – Wash step with 10 mM Tris pH 8 and 100 mM NaCl; III – Elution step with 10 mM Tris pH 11 and 100 mM NaCl; IV – Elution Step with 10 mM Tris pH 11 and 500 mM NaCl.

observed in the washing step even with the addition of 100 mM NaCl. The major portion of STEAP1 was eluted at pH 11 with 100 mM NaCl (line III), and since this concentration of salt had very little effect in the washing step, it can be safely assumed that elution is primarily dependent upon the charge modification of STEAP1 when transposing the isoelectric point. Still, a smaller STEAP1 fraction was only eluted under stronger salt influence (500 mM NaCl; line IV). In light of these new findings, slight changes were made to establish the *four-step ionic batch* with a single elution step. In this new configuration, the elution step at pH 11 with 100 mM NaCl in 10 mM Tris, was replaced by another washing step at pH 8 with 200 mM NaCl in 10 mM Tris, in an attempt to further clarify the protein fraction and then elute all of STEAP1 in a single elution step at pH 11 with 500 mM NaCl. Results from the *four-step ionic batch* can be seen in Figure

22.A. The profile for the binding and first washing step led to the same results, as these conditions were not modified. As expected, most of STEAP1 was recovered in the singular elution step at pH 11 + 500 mM NaCl. However, substantial losses were observed for the newly added washing step with 200 mM NaCl (line III). Furthermore, this highlights the difference that increasing NaCl concentrations can make, since the previous washing step (line II) barely resulted in any STEAP1 loss. Additionally, both the previous ionic batch (Figure 21) and *the four-step ionic batch* (Figure 22) also present much less complexation than the *Optimization Batch,* most definitely related to the stabilization of STEAP1 by NaCl. Furthermore, although this batch configuration allows us to recover a "cleaner" STEAP1 fraction at pH 11 + 500 mM NaCl, the losses at pH 8 + 200 mM NaCl can significantly affect the recovery levels. Thus, we accepted a loss in sample clarification and purification, in order to retain a higher %recovery, and tried to condense the batch into three steps, to recover as much STEAP1 as possible in a single step, by eliminating the washing step at pH 8 + 200 mM NaCl. However, mixed results were observed (Figure 22.B). For the first time in all batch runs, full STEAP1 binding was observed, and no losses were detected in the washing step. However, STEAP1 was found fully complexed in the elution step (Figure 22.B; line IV), even with all the optimizations made to the ionic batch strategy.

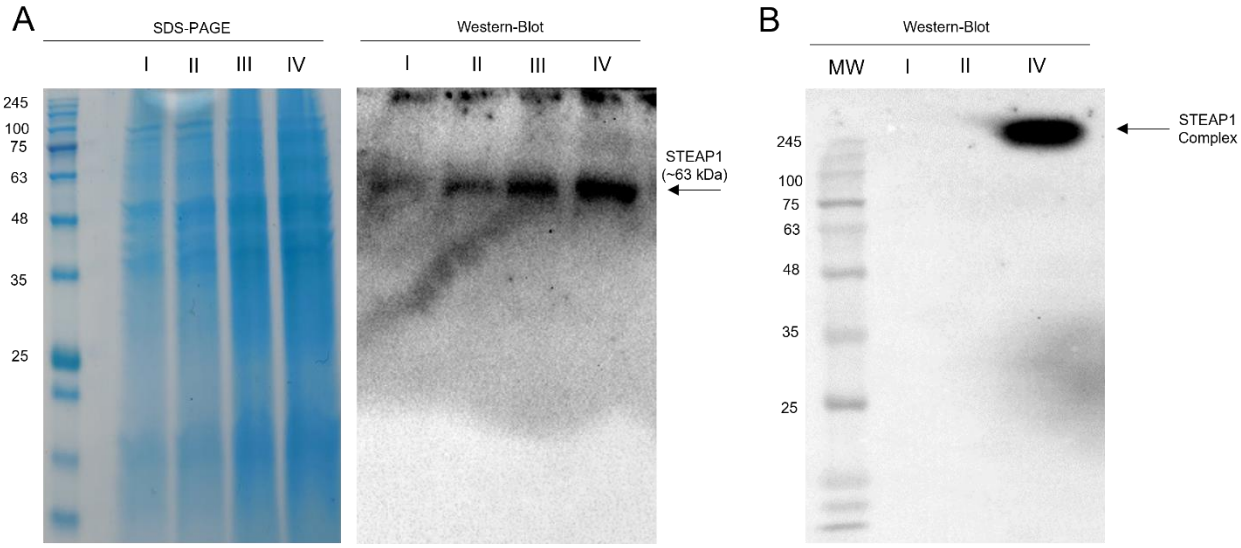

Figure 22. SDS-PAGE and Western-blot of the recovered supernatants from the ionic exchange batch for calcium-crosslinked GG microspheres for both a four-step batch (A) and Condensed batch (B) (35 mL GG microspheres); I – Sample that did not bind to GG microspheres at 10 mM MES pH 6.2; II – Wash step with 10 mM Tris pH 8 and 100 mM NaCl; III – Elution step with 10 mM Tris pH 8 and 200 mM NaCl; IV – Elution Step with 10 mM Tris pH 11 and 500 mM NaCl.

During the supernatant recovery after intra-steps centrifugations, it was observed that a portion of GG microspheres did not sediment fully and was recovered with the protein fractions. In fact, to get around this phenomenon stronger centrifugation cycles at 500g 8 min were used, as opposed to those described in the batch capture of COMT (100g for 3 min) [136], in an attempt to compact the microspheres and reduce GG

recovery. However, we were unable to identify process conditions that completely separated GG microspheres from the target protein without severely compromising batch recovery levels. Indeed, GG has a molecular weight of ~500 kDa [96], and we suspect that the formation of STEAP1-GG complexes was responsible for such high molecular weight bands in the membranes. As previously described from the SEM snapshots, GG microspheres are lacking in pores, cavities or cracks, which means than any binding that occurs, probably will be located in the surface area of GG. There is a possibility that the anti-STEAP1 antibody detects the STEAP1 molecules tightly bound to the polysaccharide, and they are reported in the high molecular weight bands >245 kDa. Further, from the FTIR spectra changes depicted in Figure 14, it appears that each GG monomer can bind several cationic moieties, which might exacerbate this detection. Moreover, a key consideration is that these STEAP1-GG complexes seem to originate outside the scope of electrostatic interactions, as at pH 11 + 500 mM NaCl, the electrostatic repulsion aided by the salt concentration should be enough to disrupt simple ionic interactions. Also, no component was added to the system which could promote covalent bonds. STEAP1 has been predicted to function as a transmembrane ionic channel, modulating the transport and concentration of small ions, calcium included [17,157]. We speculate that STEAP1 truly functions as a membrane calcium channel, and the formation of these strong complexes is mediated by some latent affinity for the calcium crosslinker. In regards to the nickel-crosslinked GG microspheres, nickel cellular uptake has been shown to be calcium dependent, with evidence suggesting that nickel crosses the plasma membrane through calcium channels [158], which might also justify the formation of STEAP1-GG complexes for these microspheres. Furthermore, STEAP1 has been associated with the Divalent Metal Transporter 1 (DMT1) in the transferrin-bound Fe uptake pathway and its heme redox potential was suitable for the reduction of metal complexes *in vivo* [20,23]. DMT1 is a known nickel transporter, and it has also been discovered that iron and nickel share and compete for absorptive pathways [159]. Perhaps the STEAP1-DMT1 relation can be extended beyond iron uptake to other metals, nickel included.

To assess the strength of the affinity-mediated STEAP1-GG complexation, fully complexed samples were coupled with a Co-IP polishing step. This technique was chosen since it is highly specific and selective in the detection of physical protein interactions [160]. The findings in Figure 23 indicate that the antibody-STEAP1 interaction is stronger than STEAP1-GG, since STEAP1 was recovered in its monomeric form (~35 kDa). This suggests that the immunoconjugates were formed, avoiding the STEAP1-GG complexes. When analyzing the SDS-PAGE, a STEAP1 fraction with a high purity degree

can be observed, although a major unidentified band was found between ~63 and ~75 kDa, which most likely corresponds to a highly overexpressed endogenous protein. Furthermore, coupling recombinant human STEAP1 lysates samples with Co-IP seems to be able to resolve the aggregation issues derived from the upstream stage (conversion of the ~63 kDa in control lysate to ~35 kDa monomeric form). Likewise, our Co-IP findings are very similar to those reported for the native STEAP1 purification workflow of hydrophobic interaction chromatography coupled with Co-IP for lysates derived from LNCaP cells [72]. This also suggests that recombinant human STEAP1 clarified and purified by the batch method with GG microspheres coupled with Co-IP retains native conformation.

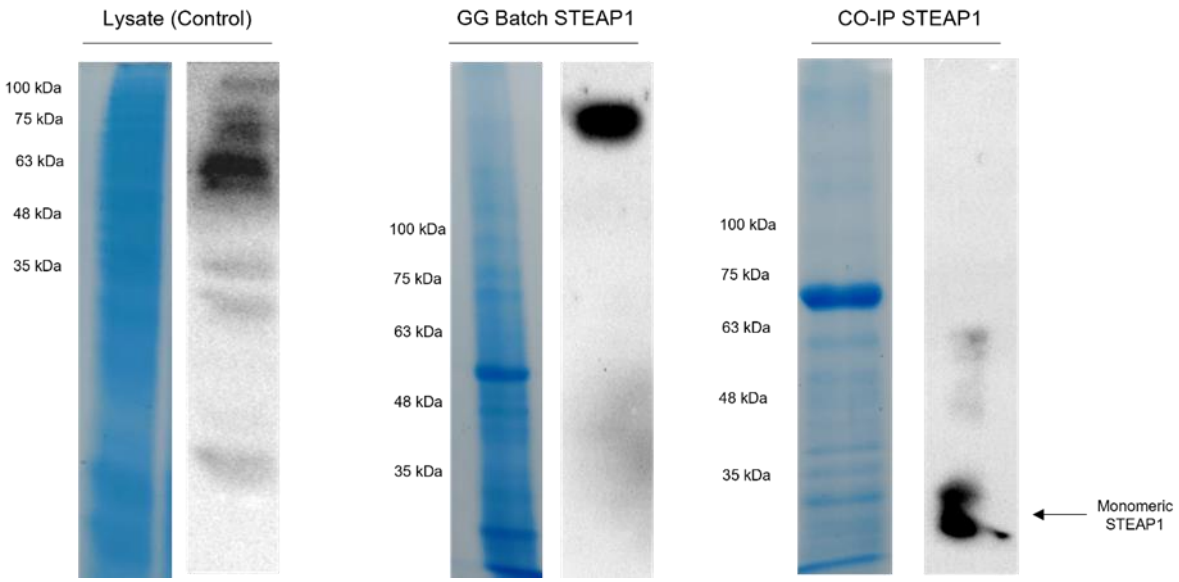

Figure 23. SDS-PAGE and Western-Blot of the entire purification workflow: the initial total protein content in *K.pastoris* lysate, the clarified sample from calcium-crosslinked GG batch and the purified co-immunoprecipitated STEAP1

Recapitulating the presented results, we can conclude that the batch method has great potential to be used as a clarification and primary capture step for STEAP1. Even in the worst case scenario, where STEAP1 is recovered in a completely complexed state from the GG batch method, these protein fractions can be coupled with Co-IP to obtain a samples with a high degree of purity.

Chapter 5 - Conclusions and future perspectives

PCa incidence is rapidly increasing, being predicted to become the most frequent cancer in males in the next decade, largely due to a “Westernized” lifestyle associated with high country developmental indexes. STEAP1 is overexpressed in PCa with a multifaceted role in the initiation and progression of PCa, with biological pathways still poorly understood or undiscovered. Currently, there are three main protein structure determination techniques: X-ray crystallography, NMR spectroscopy, and Cryo-EM. NMR spectroscopy is best suited for proteins under ~20 kDa (can determine structures up to ~35 kDa, in specific cases), while cryo-EM has been shown to not be able to determine the full STEAP1 structure, as the most flexible regions in the protein structure do not produce enough electron density. In regards to structure prediction metrics, AlphaFold produces a STEAP1 model with an overall confidence score of ~82.8% (AlphaFold2). The AlphaFold project was the highest rated prediction software in the latest Critical Assessment of protein Structure Prediction, which means even the best protein prediction AI cannot yet reach the necessary 90% confidence score to consider the structure trustworthy. As it stands, X-ray crystallography seems to be the most appropriate choice for full STEAP1 structure determination, to undertake functional and structural studies. However, this technique requires large amounts of purified protein, which current sequential chromatographic steps aren’t yielding. Further, the current purification landscape is quite complex and expensive. Therefore, the batch adsorption technique rises as a simple, fast, and low-cost alternative to the purification of STEAP1 with the advantage of being easily scaled up. Moreover, hydrogel beads have been appointed as an ideal matrix for batch adsorption. Indeed, GG is an anionic heteropolysaccharide that can form strong gels in the presence of divalent cations and is resistant to harsh processing conditions. Thus, the main objective of this work was to demonstrate for the first time, to the best of our knowledge, the suitability of GG microspheres to capture, clarify and purify STEAP1, a membrane protein, and yield high concentration fractions.

In order to achieve this goal, GG microspheres were produced through a W/O emulsion and crosslinked with two types of divalent cations: calcium and nickel. Both formulations resulted in microspheres with spherical shape and consistent structure, with lack of pores or ruptures. However, nickel-crosslinked GG microspheres presented significant rugosity as opposed to calcium-crosslinked GG microspheres. The

crosslinking and chemical integrity were evaluated by EDX and FTIR, ensuring correct microspheres production. Another key difference between both types of microspheres was that the nickel ion had a larger percentage of integration, which could justify why nickel-crosslinked GG microspheres were smaller in size, by the formation of a tighter and more compact network. Initially, both types of microspheres were employed in the batch method to capture STEAP1 from a *Komagataella pastoris* Mut X33^{+} lysate through an ionic strategy, which was based on the interaction of negative charged GG chains with positively charged STEAP1. However, it was noticed that STEAP1 formed strong complexes with GG evidenced by large molecular weight bands. To reduce complexation several relevant batch parameters were optimized. First, it was found that STEAP1 was best solubilized in 0.1% (v/v) DM detergent. Next, the ideal initial lysate concentration was found to be ~7 mg of total protein/mL (1:6 dilution) and the microsphere to buffer ratio was found to be best at 35 mL GG microspheres to 6 mL buffer. Applying optimized parameters led to similar elution profiles for calcium- and nickel-crosslinked GG microspheres. For this reason, nickel-crosslinked microspheres were applied in an affinity strategy, since nickel resins have been well documented to have strong affinity towards histidine residues, alike the His-Tag present in STEAP1. Surprisingly, all of STEAP1 can be captured through an affinity strategy towards the nickel ions crosslinking the GG backbone. However, STEAP1 captured in the batch method was much more sensitive to imidazole concentrations when compared to a standard IMAC, since it required 3.5x lower imidazole concentrations to prompt elution. Furthermore, since it was not possible to recover STEAP1 in a single step and a substantial degree of degradation was observed for this strategy it was excluded from further analysis. In regards to the ionic strategy, calcium-crosslinked GG microspheres were able to fully capture STEAP1 in a single step, with minimal losses in washing steps. Though, when employing a three-step batch method, it was observed the return of the complexes even with all the previous optimizations. Nevertheless, coupling the GG batch complexed samples with a Co-Immunoprecipitation polishing step, yields purified monomeric STEAP1 (~35 kDa). In this manner, we were able to attain the main objective, demonstrating the efficacy of a simple GG batch method to capture, clarify and purify STEAP1, when coupled with a Co-IP polishing step. Moreover, the formation of complexes seems to be STEAP1-specific, which means that similar batches can be applied to other membrane proteins.

The major limitation of this work was that the analysis was completely conducted in a qualitative approach. Indeed, the formation of STEAP1-GG complexes and the fact that GG microspheres were recovered with the protein fractions compromised

quantification. It is a known fact that reducing sugars skew protein quantification results derived from BCA or Lowry assay. Since GG is constituted by glucose monomers, these methods were automatically excluded, as to not present unreliable and false positive results. The Bradford assay is affected by detergents and for this reason was also excluded as a possibility. This leaves immunoquantification protocols, such as enzyme linked immunosorbent assay, as the last alternative. Yet, these methods are notoriously expensive, when compared to standard spectrophotometric assays. Since tackling the downstream processing costs was a secondary goal, it is imperative to develop an inexpensive colorimetric STEAP1-specific quantification method. Indeed, our research group has already planned the development of such a method, by the detection of STEAP1 iron reduction by the ferrozine reagent. The resultant absorbance will be correlated with STEAP1 concentration and hopefully we can implement this method in the future to assess the STEAP1 concentration from GG batch fractions and compare with the results present in the literature.

In future work, it is also relevant to assess the nature of such strong complexes. One option would be to explore different GG coatings, and their effect on complex formation. Alternatively, the addition of a fluorescent tag in STEAP1 in conjunction with fluorescence microscopy analysis in samples from different time points in the batch could also be beneficial for enlightening this phenomenon. Moreover, the uncertainty on whether the GG-STEAP1 complexes will develop fully or partially, makes this purification workflow not entirely reproducible. This effect will also most likely restrict the GG batch method to the Co-immunoprecipitation polishing step, since this technique was responsible for the disruption of the complexes. In future research, the addition of STEAP1 stabilizing agents in the batch buffers should be explored to tackle this issue. Additionally, the reusability of GG microspheres should be assessed. That is, how many batch runs are possible for each GG microspheres formulation stage. This factor will be very relevant when assessing the feasibility of larger scale purification systems based on the GG batch method.

Chapter 6 – Bibliography

1. Sung, H. *et al.* Global Cancer Statistics 2020: GLOBOCAN Estimates of Incidence and Mortality Worldwide for 36 Cancers in 185 Countries. *CA. Cancer J. Clin.* **71**, 209–249 (2021).
2. Sandhu, S. *et al.* Prostate cancer. *Lancet* **398**, 1075–1090 (2021).
3. Rawla, P. Epidemiology of Prostate Cancer. *World J. Oncol.* **10**, 63–89 (2019).
4. Nelson, W. G., De Marzo, A. M. & Isaacs, W. B. Prostate Cancer. *N. Engl. J. Med.* **349**, 366–381 (2003).
5. Rebello, R. J. *et al.* Prostate cancer. *Nat. Rev. Dis. Prim.* **7**, 9 (2021).
6. Davies, A., Conteduca, V., Zoubeidi, A. & Beltran, H. Biological Evolution of Castration-resistant Prostate Cancer. *Eur. Urol. Focus* **5**, 147–154 (2019).
7. Abida, W. *et al.* Prospective Genomic Profiling of Prostate Cancer Across Disease States Reveals Germline and Somatic Alterations That May Affect Clinical Decision Making. *JCO Precis. Oncol.* 1–16 (2017) doi:10.1200/PO.17.00029.
8. Abida, W. *et al.* Genomic correlates of clinical outcome in advanced prostate cancer. *Proc. Natl. Acad. Sci.* **116**, 11428–11436 (2019).
9. Abeshouse, A. *et al.* The Molecular Taxonomy of Primary Prostate Cancer. *Cell* **163**, 1011–1025 (2015).
10. Quigley, D. A. *et al.* Genomic Hallmarks and Structural Variation in Metastatic Prostate Cancer. *Cell* **174**, 758-769.e9 (2018).
11. D Mazhar, J. W. Prostate Cancer Prostate Cancer. *Abeloff's Clin. Oncol. 5/e* **8**, 938–944 (2015).
12. Hubert, R. S. *et al.* STEAP: A prostate-specific cell-surface antigen highly expressed in human prostate tumors. *Proc. Natl. Acad. Sci. U. S. A.* **96**, 14523–14528 (1999).
13. Gomes, I. M., Arinto, P., Lopes, C., Santos, C. R. & Maia, C. J. STEAP1 is overexpressed in prostate cancer and prostatic intraepithelial neoplasia lesions, and it is positively associated with Gleason score. *Urol. Oncol. Semin. Orig. Investig.* **32**, 53.e23-53.e29 (2014).
14. Porzycki, P. & Ciszkowicz, E. Modern biomarkers in prostate cancer diagnosis. *Cent. Eur. J. Urol.* **73**, 300–306 (2020).

15. Chen, W. J. *et al.* Regulatory Roles of Six-Transmembrane Epithelial Antigen of the Prostate Family Members in the Occurrence and Development of Malignant Tumors. *Front. Cell Dev. Biol.* **9**, 1–10 (2021).

16. Ihlaseh-Catalano, S. M. *et al.* STEAP1 protein overexpression is an independent marker for biochemical recurrence in prostate carcinoma. *Histopathology* **63**, 678–685 (2013).

17. Gomes, I. M., Maia, C. J. & Santos, C. R. STEAP proteins: From structure to applications in cancer therapy. *Mol. Cancer Res.* **10**, 573–587 (2012).

18. Dell'Angelica, J. S. B. and E. C. Molecular Bases for the Recognition of Tyrosine-based Sorting Signals. *Curr. Opin. Cell Biol.* **1**, 617–623 (1989).

19. Ohgami, R. S., Campagna, D. R., McDonald, A. & Fleming, M. D. The Steap proteins are metalloreductases. *Blood* **108**, 1388–1394 (2006).

20. Hare, D., Ayton, S., Bush, A. & Lei, P. A delicate balance: Iron metabolism and diseases of the brain. *Front. Aging Neurosci.* **5**, (2013).

21. Gomes, I. M., Santos, C. R. & Maia, C. J. Expression of steap1 and steap1b in prostate cell lines, and the putative regulation of steap1 by post-transcriptional and post-translational mechanisms. *Genes and Cancer* **5**, 142–151 (2014).

22. Grunewald, T. G. P., Bach, H., Cossarizza, A. & Matsumoto, I. The STEAP protein family: Versatile oxidoreductases and targets for cancer immunotherapy with overlapping and distinct cellular functions. *Biol. Cell* **104**, 641–657 (2012).

23. Kim, K. *et al.* Six-Transmembrane Epithelial Antigen of Prostate 1 (STEAP1) Has a Single b Heme and Is Capable of Reducing Metal Ion Complexes and Oxygen. *Biochemistry* **55**, 6673–6684 (2016).

24. Abubakar. Comparative transcriptional study of the effects of high intracellular zinc on prostate carcinoma cells. *Oncol. Rep.* **23**, 861–867 (2010).

25. Barroca-Ferreira, J. *et al.* Targeting STEAP1 Protein in Human Cancer: Current Trends and Future Challenges. *Curr. Cancer Drug Targets* **18**, 222–230 (2017).

26. Yamamoto, T. *et al.* Six-transmembrane epithelial antigen of the prostate-1 plays a role for in vivo tumor growth via intercellular communication. *Exp. Cell Res.* **319**, 2617–2626 (2013).

27. Esmaeili, S.-A., Nejatollahi, F. & Sahebkar, A. Inhibition of Intercellular Communication between Prostate Cancer Cells by A Specific Anti-STEAP-1 Single Chain Antibody. *Anti-Cancer Agents in Medicinal Chemistry* vol. 18 1674–1679 (2018).

28. Vaghjiani, R. J., Talma, S. & Murphy, C. L. Six-transmembrane epithelial antigen of the prostate (STEAP1 and STEAP2)-Differentially expressed by murine and human mesenchymal stem cells. *Tissue Eng. - Part A* **15**, 2073–2083 (2009).

29. Khanna, K., Salmond, N., Lynn, K. S., Leong, H. S. & Williams, K. C. Clinical significance of STEAP1 extracellular vesicles in prostate cancer. *Prostate Cancer Prostatic Dis.* **24**, 802–811 (2021).

30. Mariscal, J. *et al.* Comprehensive palmitoyl-proteomic analysis identifies distinct protein signatures for large and small cancer-derived extracellular vesicles. *J. Extracell. Vesicles* **9**, (2020).

31. Oosterheert, W. & Gros, P. Cryo-electron microscopy structure and potential enzymatic function of human six-transmembrane epithelial antigen of the prostate 1 (STEAP1). *J. Biol. Chem.* **295**, 9502–9512 (2020).

32. Mills, E., Dong, X. P., Wang, F. & Xu, H. Mechanisms of brain iron transport: Insight into neurodegeneration and CNS disorders. *Future Med. Chem.* **2**, 51–64 (2010).

33. Grunewald, T. G. P. *et al.* STEAP1 is associated with the invasive and oxidative stress phenotype of ewing tumors. *Mol. Cancer Res.* **10**, 52–65 (2012).

34. Rocha, S. M. *et al.* Promoter demethylation upregulates STEAP1 gene expression in human prostate cancer: And in silico analysis. *Life* **11**, (2021).

35. Jumper, J. *et al.* Highly accurate protein structure prediction with AlphaFold. *Nature* **596**, 583–589 (2021).

36. Wu, H. T. *et al.* The Tumor Suppressive Roles and Prognostic Values of STEAP Family Members in Breast Cancer. *Biomed Res. Int.* **2020**, (2020).

37. Azumi, M. *et al.* Six-Transmembrane Epithelial Antigen of the Prostate as an Immunotherapeutic Target for Renal Cell and Bladder Cancer. *J. Urol.* **183**, 2036–2044 (2010).

38. Nakamura, H. *et al.* Six-transmembrane epithelial antigen of the prostate 1 protects against increased oxidative stress via a nuclear erythroid 2-related factor pathway in colorectal cancer. *Cancer Gene Ther.* **26**, 313–322 (2019).

39. Sun, J. *et al.* Six-transmembrane epithelial antigen of the prostate 1 is associated with tumor invasion and migration in endometrial carcinomas. *J. Cell. Biochem.* **120**, 11172–11189 (2019).

40. Grunewald, T. G. P. *et al.* High steap1 expression is associated with improved outcome of ewing's sarcoma patients. *Ann. Oncol.* **23**, 2185–2190 (2012).

41. Wu, Y. Y., Jiang, J. N., Fang, X. D. & Ji, F. J. STEAP1 regulates tumorigenesis and chemoresistance during peritoneal metastasis of gastric cancer. *Front. Physiol.* **9**, 1–7 (2018).

42. Iijima, K. *et al.* Six-transmembrane epithelial antigen of the prostate 1 accelerates cell proliferation by targeting c-Myc in liver cancer cells. *Oncol. Lett.* **22**, 1–9 (2021).

43. Guo, Q. *et al.* Evaluation of the Prognostic Value of STEAP1 in Lung Adenocarcinoma and Insights Into Its Potential Molecular Pathways via Bioinformatic Analysis. *Front. Genet.* **11**, 1–13 (2020).

44. Jiao, Z. *et al.* Six-transmembrane epithelial antigen of the prostate 1 expression promotes ovarian cancer metastasis by aiding progression of epithelial-to-mesenchymal transition. *Histochem. Cell Biol.* **154**, 215–230 (2020).

45. Zhang, Z. *et al.* A research of STEAP1 regulated gastric cancer cell proliferation, migration and invasion in vitro and in vivos. *J. Cell. Mol. Med.* **24**, 14217–14230 (2020).

46. Zhao, Z. *et al.* Predictive potential of STEAP family for survival, immune microenvironment and therapy response in glioma. *Int. Immunopharmacol.* **101**, 108183 (2021).

47. Xie, J. *et al.* STEAP1 Inhibits Breast Cancer Metastasis and Is Associated With Epithelial–Mesenchymal Transition Procession. *Clin. Breast Cancer* **19**, e195–e207 (2019).

48. Markey, F. B., Romero, B., Parashar, V. & Batish, M. Identification of a New Transcriptional Co-Regulator of STEAP1 in Ewing's Sarcoma. *Cells* **10**, 1300 (2021).

49. Gomes, I. M. *et al.* Knockdown of STEAP1 inhibits cell growth and induces apoptosis in LNCaP prostate cancer cells counteracting the effect of androgens. *Med. Oncol.* **35**, 1–10 (2018).

50. Gomes, I. M., Santos, C. R., Socorro, S. & Maia, C. J. Six transmembrane epithelial antigen of the prostate 1 is down-regulated by sex hormones in prostate cells. *Prostate* **73**, 605–613 (2013).

51. Liu, T. *et al.* Expression and prognostic analyses of the significance of STEAP1 and STEAP2 in lung cancer. *World J. Surg. Oncol.* **20**, 1–14 (2022).

52. Carrasquillo, J. A. *et al.* Imaging patients with metastatic castration-resistant prostate cancer using 89Zr-DFO-MSTP2109A anti-STEAP1 antibody. *J. Nucl.*

Med. **60**, 1517–1523 (2019).

53. Doran, M. G. *et al.* Annotating STEAP1 regulation in prostate cancer with 89Zr immuno-PET. *J. Nucl. Med.* **55**, 2045–2049 (2014).

54. O'Donoghue, J. A. *et al.* Pharmacokinetics and biodistribution of a [89Zr]Zr-DFO-MSTP2109A Anti-STEAP1 antibody in metastatic castration-resistant prostate cancer patients. *Mol. Pharm.* **16**, 3083–3090 (2019).

55. Danila, D. C. *et al.* Phase i Study of DSTP3086S, an antibody-drug conjugate targeting six-transmembrane epithelial antigen of prostate 1, in metastatic castration-resistant prostate cancer. *J. Clin. Oncol.* **37**, 3518–3527 (2019).

56. Williams, S. P. *et al.* ImmunoPET helps predicting the efficacy of antibody-drug conjugates targeting TENB2 and STEAP1. *Oncotarget* **7**, 25103–25112 (2016).

57. Boswell, C. A. *et al.* Impact of drug conjugation on pharmacokinetics and tissue distribution of Anti-STEAP1 antibody-drug conjugates in rats. *Bioconjug. Chem.* **22**, 1994–2004 (2011).

58. Altvater, B. *et al.* Common Ewing sarcoma-associated antigens fail to induce natural T cell responses in both patients and healthy individuals. *Cancer Immunol. Immunother.* **63**, 1047–1060 (2014).

59. Altvater, B. *et al.* Activated human γδ T cells induce peptide-specific CD8+ T-cell responses to tumor-associated self-antigens. *Cancer Immunol. Immunother.* **61**, 385–396 (2012).

60. Herrmann, V. L., Wieland, D. E., Legler, D. F., Wittmann, V. & Groettrup, M. The STEAP1262-270 peptide encapsulated into PLGA microspheres elicits strong cytotoxic T cell immunity in HLA-A∗0201 transgenic mice - A new approach to immunotherapy against prostate carcinoma. *Prostate* **76**, 456–468 (2016).

61. Krupa, M. *et al.* Immunization with recombinant DNA and modified vaccinia virus Ankara (MVA) vectors delivering PSCA and STEAP1 antigens inhibits prostate cancer progression. *Vaccine* **29**, 1504–1513 (2011).

62. Thorne, A. H. *et al.* Adjuvant Screen Identifies Synthetic DNA-Encoding Flt3L and CD80 Immunotherapeutics as Candidates for Enhancing Anti-tumor T Cell Responses. *Front. Immunol.* **11**, 1–14 (2020).

63. Schober, S. J. *et al.* MHC Class I-Restricted TCR-Transgenic CD4+ T Cells Against STEAP1 Mediate Local Tumor Control of Ewing Sarcoma In Vivo. *Cells* **9**, 1–16 (2020).

64. Chen, B. *et al.* Formation and performance of high acyl gellan hydrogel affected

by the addition of physical-chemical treated insoluble soybean fiber. *Food Hydrocoll.* **101**, 105526 (2020).

65. Cappuccini, F., Stribbling, S., Pollock, E., Hill, A. V. S. & Redchenko, I. Immunogenicity and efficacy of the novel cancer vaccine based on simian adenovirus and MVA vectors alone and in combination with PD-1 mAb in a mouse model of prostate cancer. *Cancer Immunol. Immunother.* **65**, 701–713 (2016).

66. Zhang, X. *et al.* Preparation and characterization of gellan gum-chitosan polyelectrolyte complex films with the incorporation of thyme essential oil nanoemulsion. *Food Hydrocoll.* **114**, 106570 (2021).

67. Schirmer, D. *et al.* Transgenic antigen-specific, HLA-A*02:01-allo-restricted cytotoxic T cells recognize tumor-associated target antigen STEAP1 with high specificity. *Oncoimmunology* **5**, 1–11 (2016).

68. Kübler, H. *et al.* Self-adjuvanted mRNA vaccination in advanced prostate cancer patients: A first-in-man phase I/IIa study. *J. Immunother. Cancer* **3**, 1–14 (2015).

69. Maia, E. H. B., Assis, L. C., de Oliveira, T. A., da Silva, A. M. & Taranto, A. G. Structure-Based Virtual Screening: From Classical to Artificial Intelligence. *Front. Chem.* **8**, (2020).

70. Zhong, L. *et al.* Small molecules in targeted cancer therapy: advances, challenges, and future perspectives. *Signal Transduct. Target. Ther.* **6**, (2021).

71. Rabiee, M., Namaei Ghasemnia, N., Rabiee, N. & Bagherzadeh, M. Chapter 7 - Microfluidic devices and drug delivery systems. in *Biomedical Applications of Microfluidic Devices* (eds. Hamblin, M. R. & Karimi, M.) 153–186 (Academic Press, 2021). doi:https://doi.org/10.1016/B978-0-12-818791-3.00013-9.

72. Barroca-Ferreira, J. *et al.* Enhanced stability of detergent-free human native STEAP1 protein from neoplastic prostate cancer cells upon an innovative isolation procedure. *Int. J. Mol. Sci.* **22**, 1–15 (2021).

73. Duarte, D. R. *et al.* Impact of glycerol feeding profiles on STEAP1 biosynthesis by Komagataella pastoris using a methanol-inducible promoter. *Appl. Microbiol. Biotechnol.* **105**, 4635–4648 (2021).

74. Mastropietro, G., Aw, R. & Polizzi, K. M. Chapter Three - Expression of proteins in Pichia pastoris. in *Recombinant Protein Expression: Eukaryotic Hosts* (eds. O'Dell, W. B. & Kelman, Z.) vol. 660 53–80 (Academic Press, 2021).

75. Warner, T. N. & Nochumson, S. Rethinking the economics of chromatography: New technologies and hidden costs. *BioPharm Int.* **16**, 58–60 (2003).

76. Banki, M. R. & Wood, D. W. Inteins and affinity resin substitutes for protein purification and scale up. *Microb. Cell Fact.* **4**, 1–6 (2005).

77. D'Souza, R. N. *et al.* Emerging technologies for the integration and intensification of downstream bioprocesses. *Pharm. Bioprocess.* **1**, 423–440 (2013).

78. Warikoo, V. *et al.* Integrated continuous production of recombinant therapeutic proteins. *Biotechnol. Bioeng.* **109**, 3018–3029 (2012).

79. Singh, N. *et al.* Clarification technologies for monoclonal antibody manufacturing processes: Current state and future perspectives. *Biotechnol. Bioeng.* **113**, 698–716 (2016).

80. Gagaoua, M. & Hafid, K. Three Phase Partitioning System, an Emerging Non-Chromatographic Tool for Proteolytic Enzymes Recovery and Purification. *Biosens. J.* **5**, (2016).

81. Ward, W. & Swiatek, G. Protein Purification. *Curr. Anal. Chem.* **5**, 85–105 (2009).

82. Flickinger, M. C., Drew, S. W. & Wiley, J. *Encyclopedia of bioprocess technology: fermentation, biocatalysis, and bioseparation*. *Choice Reviews Online* vol. 37 (1999).

83. Hlady, V., Buijs, J. & Jennissen, H. P. Methods for studying protein adsorption. in *Molecular and Cellular Biochemistry* vol. 23 402–429 (1999).

84. Gondim, D. R. *et al.* Protein adsorption onto modified porous silica by single and binary human serum protein solutions. *Int. J. Mol. Sci.* **22**, (2021).

85. Dawes, C. C., Jewess, P. J. & Murray, D. A. Thiophilic paramagnetic particles as a batch separation medium for the purification of antibodies from various source materials. *Anal. Biochem.* **338**, 186–191 (2005).

86. Koubková, J. *et al.* Magnetic poly(glycidyl methacrylate) microspheres for protein capture. *N. Biotechnol.* **31**, 482–491 (2014).

87. Zhou, J. *et al.* Thiolactone-based conjugation assisted magnetic imprinted microspheres for specific capturing target proteins. *Chem. Eng. J.* **399**, 125767 (2020).

88. Kawaguchi, H. Functional polymer microspheres. *Prog. Polym. Sci.* **25**, 1171–1210 (2000).

89. Zhang, W. Nanoparticle aggregation: Principles and modeling. *Adv. Exp. Med. Biol.* **811**, 20–43 (2014).

90. Prajapati, V. D., Jani, G. K., Zala, B. S. & Khutliwala, T. A. An insight into the

emerging exopolysaccharide gellan gum as a novel polymer. *Carbohydr. Polym.* **93**, 670–678 (2013).

91. Giavasis, I., Harvey, L. M. & McNeil, B. Gellan gum. *Crit. Rev. Biotechnol.* **20**, 177–211 (2000).

92. Bajaj, I. B., Survase, S. A., Saudagar, P. S. & Singhal, R. S. Gellan gum: Fermentative production, downstream processing and applications. *Food Technol. Biotechnol.* **45**, 341–354 (2007).

93. Banik, R. M., Kanari, B. & Upadhyay, S. N. Exopolysaccharide of the gellan family: Prospects and potential. *World J. Microbiol. Biotechnol.* **16**, 407–414 (2000).

94. Villarreal-Otalvaro, C. & Coburn, J. M. Fabrication Methods and Form Factors of Gellan Gum-Based Materials for Drug Delivery and Anti-Cancer Applications. *ACS Biomater. Sci. Eng.* (2021) doi:10.1021/acsbiomaterials.1c00685.

95. Morris, E. R., Nishinari, K. & Rinaudo, M. Gelation of gellan - A review. *Food Hydrocoll.* **28**, 373–411 (2012).

96. Bacelar, A. H., Silva-Correia, J., Oliveira, J. M. & Reis, R. L. Recent progress in gellan gum hydrogels provided by functionalization strategies. *J. Mater. Chem. B* **4**, 6164–6174 (2016).

97. Osmałek, T., Froelich, A. & Tasarek, S. Application of gellan gum in pharmacy and medicine. *Int. J. Pharm.* **466**, 328–340 (2014).

98. Fialho, A. M. *et al.* Occurrence, production, and applications of gellan: Current state and perspectives. *Appl. Microbiol. Biotechnol.* **79**, 889–900 (2008).

99. Hishamuddin, N. I., Razali, M. H. & Amin, K. A. M. Application of Gellan Gum Biopolymer in Biomedical Applications: A Review. *Makara J. Sci.* **26**, 11–24 (2022).

100. Zia, K. M. *et al.* Recent trends on gellan gum blends with natural and synthetic polymers: A review. *Int. J. Biol. Macromol.* **109**, 1068–1087 (2018).

101. Yu, I., Kaonis, S. & Chen, R. A Study on Degradation Behavior of 3D Printed Gellan Gum Scaffolds. *Procedia CIRP* **65**, 78–83 (2017).

102. Sapper, M., Bonet, M. & Chiralt, A. Wettability of starch-gellan coatings on fruits, as affected by the incorporation of essential oil and/or surfactants. *Lwt* **116**, 108574 (2019).

103. Danalache, F., Carvalho, C. Y., Alves, V. D., Moldão-Martins, M. & Mata, P. Optimisation of gellan gum edible coating for ready-to-eat mango (Mangifera indica L.) bars. *Int. J. Biol. Macromol.* **84**, 43–53 (2016).

104. Tomadoni, B., Moreira, M. R., Pereda, M. & Ponce, A. G. Gellan-based coatings incorporated with natural antimicrobials in fresh-cut strawberries: Microbiological and sensory evaluation through refrigerated storage. *Lwt* **97**, 384–389 (2018).

105. Criado, P., Fraschini, C., Shankar, S., Salmieri, S. & Lacroix, M. Influence of cellulose nanocrystals gellan gum-based coating on color and respiration rate of Agaricus bisporus mushrooms. *J. Food Sci.* **86**, 420–425 (2021).

106. Wei, Y. C., Cheng, C. H., Ho, Y. C., Tsai, M. L. & Mi, F. L. Active gellan gum/purple sweet potato composite films capable of monitoring pH variations. *Food Hydrocoll.* **69**, 491–502 (2017).

107. Sajna, K. V., Gottumukkala, L. D., Sukumaran, R. K. & Pandey, A. *White Biotechnology in Cosmetics*. *Industrial Biorefineries and White Biotechnology* (Elsevier B.V., 2015). doi:10.1016/B978-0-444-63453-5.00020-3.

108. Dhanka, M., Shetty, C. & Srivastava, R. Methotrexate loaded gellan gum microparticles for drug delivery. *Int. J. Biol. Macromol.* **110**, 346–356 (2018).

109. Babu, R., Sathigari, S., Kumar, M. & Pandit, J. Formulation of Controlled Release Gellan Gum Macro Beads of Amoxicillin. *Curr. Drug Deliv.* **7**, 36–43 (2010).

110. Prezotti, F. G., Cury, B. S. F. & Evangelista, R. C. Mucoadhesive beads of gellan gum/pectin intended to controlled delivery of drugs. *Carbohydr. Polym.* **113**, 286–295 (2014).

111. Boni, F. I., Prezotti, F. G. & Cury, B. S. F. Gellan gum microspheres crosslinked with trivalent ion: effect of polymer and crosslinker concentrations on drug release and mucoadhesive properties. *Drug Dev. Ind. Pharm.* **42**, 1283–1290 (2016).

112. Liang, L. *et al.* Carboxymethyl konjac glucomannan mechanically reinforcing gellan gum microspheres for uranium removal. *Int. J. Biol. Macromol.* **145**, 535–546 (2020).

113. Tran, T. P. A., Cho, H., Cho, G. C., Han, J. I. & Chang, I. Nickel (Ni2+) removal from water using gellan gum–sand mixture as a filter material. *Appl. Sci.* **11**, (2021).

114. Liu, X. *et al.* Fully Biomass-Based Hybrid Hydrogel for Efficient Solar Desalination with Salt Self-Cleaning Property. *ACS Appl. Mater. Interfaces* (2021) doi:10.1021/acsami.1c11636.

115. Mustapha, M. U., Halimoon, N., Johari, W. L. W. & Shukor, M. Y. A. Enhanced

carbofuran degradation using immobilized and free cells of Enterobacter sp. isolated from soil. *Molecules* **25**, (2020).

116. Park, H. *et al.* Enhanced biodegradation of hydrocarbons by Pseudomonas aeruginosa-encapsulated alginate/gellan gum microbeads. *J. Hazard. Mater.* **406**, (2021).

117. Shabani, S. & Dinari, M. Ag/LDH-itaconic acid-gellan gam nanocomposites: Facile and green synthesis, characterization, and excellent catalytic reduction of 4-nitrophenol. *Int. J. Biol. Macromol.* **193**, 1645–1652 (2021).

118. Fan, Y., Yi, J., Hua, X., Zhang, Y. & Yang, R. Preparation and characterization of gellan gum microspheres containing a cold-adapted β-galactosidase from Rahnella sp. R3. *Carbohydr. Polym.* **162**, 10–15 (2017).

119. Lyu, C. J. *et al.* Biosynthesis of γ-aminobutyrate by engineered Lactobacillus brevis cells immobilized in gellan gum gel beads. *J. Biosci. Bioeng.* **128**, 123–128 (2019).

120. Iurciuc (Tincu), C. E. *et al.* Yeast cells immobilized in spherical gellan particles cross-linked with magnesium acetate. *J. Biotechnol.* **236**, 45–56 (2016).

121. Milivojevic, M., Pajic-Lijakovic, I., Bugarski, B., Nayak, A. K. & Hasnain, M. S. *Gellan gum in drug delivery applications*. *Natural Polysaccharides in Drug Delivery and Biomedical Applications* (Elsevier Inc., 2019). doi:10.1016/B978-0-12-817055-7.00006-6.

122. Homayun, B., Lin, X. & Choi, H.-J. Challenges and Recent Progress in Oral Drug Delivery Systems for Biopharmaceuticals. *Pharmaceutics* **11**, 129 (2019).

123. Göttel, B. *et al.* In situ Gelling Amphotericin B Nanofibers: A New Option for the Treatment of Keratomycosis. *Front. Bioeng. Biotechnol.* **8**, 1–16 (2020).

124. Gizurarson, S. The Effect of Cilia and the Mucociliary Clearance on Successful Drug Delivery. *Biol. Pharm. Bull.* **38**, 497–506 (2015).

125. Mahajan, H. S. & Gattani, S. G. Nasal administration of ondansetron using a novel microspheres delivery system. *Pharm. Dev. Technol.* **14**, 226–232 (2009).

126. Cho, H. H. *et al.* Comparative Study on the Effect of the Different Harvesting Sources of Demineralized Bone Particles on the Bone Regeneration of a Composite Gellan Gum Scaffold for Bone Tissue Engineering Applications. *ACS Appl. Bio Mater.* **4**, 1900–1911 (2021).

127. Aadil, K. R., Nathani, A., Sharma, C. S., Lenka, N. & Gupta, P. Investigation of poly(vinyl) alcohol-gellan gum based nanofiber as scaffolds for tissue engineering

applications. *J. Drug Deliv. Sci. Technol.* **54**, 101276 (2019).

128. Ismail, N. A., Amin, K. A. M., Majid, F. A. A. & Razali, M. H. Gellan gum incorporating titanium dioxide nanoparticles biofilm as wound dressing: Physicochemical, mechanical, antibacterial properties and wound healing studies. *Mater. Sci. Eng. C* **103**, 109770 (2019).

129. Jiang, J. *et al.* Dual functional modification of gellan gum hydrogel by introduction of methyl methacrylate and RGD contained polypeptide. *Mater. Lett.* **264**, 127341 (2020).

130. Trucco, D. *et al.* Graphene Oxide-Doped Gellan Gum–PEGDA Bilayered Hydrogel Mimicking the Mechanical and Lubrication Properties of Articular Cartilage. *Adv. Healthc. Mater.* **10**, (2021).

131. De Souza, F. S. *et al.* Evaluation of different methods to prepare superabsorbent hydrogels based on deacetylated gellan. *Carbohydr. Polym.* **148**, 309–317 (2016).

132. ter Horst, B. *et al.* A gellan-based fluid gel carrier to enhance topical spray delivery. *Acta Biomater.* **89**, 166–179 (2019).

133. Dohle, E. *et al.* Co-culture Model for Cutaneous Wound Healing to Assess a Porous Fiber-Based Drug Delivery System. *Tissue Eng. - Part C Methods* **26**, 475–484 (2020).

134. Xu, L. *et al.* Preparation and characterisation of a gellan gum-based hydrogel enabling osteogenesis and inhibiting Enterococcus faecalis. *Int. J. Biol. Macromol.* **165**, 2964–2973 (2020).

135. Gonçalves, A. I. C., Rocha, L. A., Dias, J. M. L., Passarinha, L. A. & Sousa, A. Optimization of a chromatographic stationary phase based on gellan gum using central composite design. *J. Chromatogr. B Anal. Technol. Biomed. Life Sci.* **957**, 46–52 (2014).

136. Gomes, D. *et al.* Applications of gellan natural polymer microspheres in recombinant catechol-O-methyltransferase direct capture from a Komagataella pastoris lysate. *Int. J. Biol. Macromol.* **172**, 186–196 (2021).

137. Gomes, D., Costa, D., Queiroz, J. A., Passarinha, L. A. & Sousa, A. A new insight in gellan microspheres application to capture a plasmid DNA vaccine from an Escherichia coli lysate. *Sep. Purif. Technol.* **274**, 119013 (2021).

138. Coelho, J. *et al.* Biosynthesis and isolation of gellan polysaccharide to formulate microspheres for protein capture. *Carbohydr. Polym.* **220**, 236–246 (2019).

139. Laemmli, U. K. Cleavage of structural proteins during the assembly of the head of

bacteriophage T4. *Nature* **227**, 680–685 (1970).

140. Joye, I. J. & McClements, D. J. Biopolymer-based nanoparticles and microparticles: Fabrication, characterization, and application. *Curr. Opin. Colloid Interface Sci.* **19**, 417–427 (2014).

141. Rabanel, J. M., Banquy, X., Zouaoui, H., Mokhtar, M. & Hildgen, P. Progress technology in microencapsulation methods for Cell therapy. *Biotechnol. Prog.* **25**, 946–963 (2009).

142. Abbas, Z. & Marihal, S. Gellan gum-based mucoadhesive microspheres of almotriptan for nasal administration: Formulation optimization using factorial design, characterization, and in vitro evaluation. *J. Pharm. Bioallied Sci.* **6**, 267 (2014).

143. Narkar, M., Sher, P. & Pawar, A. Stomach-Specific Controlled Release Gellan Beads of Acid-Soluble Drug Prepared by Ionotropic Gelation Method. *AAPS PharmSciTech* **11**, 267–277 (2010).

144. Bhattacharya, S. S. *et al.* Tranexamic acid loaded gellan gum-based polymeric microbeads for controlled release: In vitro and in vivo assessment. *Colloids Surfaces B Biointerfaces* **112**, 483–491 (2013).

145. Patil, S., Sharma, S., Nimbalkar, A. & Pawar, A. Study of Formulation Variables on Properties of Drug-Gellan Beads by Factorial Design. *Drug Dev. Ind. Pharm.* **32**, 315–326 (2006).

146. Agnihotri, S. A. & Aminabhavi, T. M. Development of Novel Interpenetrating Network Gellan Gum-Poly(vinyl alcohol) Hydrogel Microspheres for the Controlled Release of Carvedilol. *Drug Dev. Ind. Pharm.* **31**, 491–503 (2005).

147. Kozlowski, L. P. Proteome-pI: Proteome isoelectric point database. *Nucleic Acids Res.* **45**, D1112–D1116 (2017).

148. Blanchard, V. *et al.* High-level expression of biologically active glycoprotein hormones in Pichia pastoris strains - Selection of strain GS115, and not X-33, for the production of biologically active N-glycosylated 15N-labeled phCG. *Glycoconj. J.* **25**, 245–257 (2008).

149. Cassanelli, M., Prosapio, V., Norton, I. & Mills, T. Acidified/basified gellan gum gels: The role of the structure in drying/rehydration mechanisms. *Food Hydrocoll.* **82**, 346–354 (2018).

150. Tsuji, Y. Transmembrane protein western blotting: Impact of sample preparation on detection of SLC11A2 (DMT1) and SLC40A1 (ferroportin). *PLoS One* **15**, 1–18

(2020).

151. Seddon, A. M., Curnow, P. & Booth, P. J. Membrane proteins, lipids and detergents: Not just a soap opera. *Biochim. Biophys. Acta - Biomembr.* **1666**, 105–117 (2004).

152. Kalipatnapu, S. & Chattopadhyay, A. Membrane protein solubilization: Recent advances and challenges in solubilization of serotonin1A receptors. *IUBMB Life* **57**, 505–512 (2005).

153. Kermani, A. A. A guide to membrane protein X-ray crystallography. *FEBS J.* **288**, 5788–5804 (2021).

154. Boivin, S., Kozak, S. & Meijers, R. Optimization of protein purification and characterization using Thermofluor screens. *Protein Expr. Purif.* **91**, 192–206 (2013).

155. Reyes-Alcaraz, A., Martínez-Archundia, M., Ramon, E. & Garriga, P. Salt effects on the conformational stability of the visual G-protein-coupled receptor rhodopsin. *Biophys. J.* **101**, 2798–2806 (2011).

156. Cytiva. Affinity Chromatography Vol. 2: Tagged proteins. **2**, (2021).

157. Barroca-Ferreira, J. *et al.* Targeting STEAP1 Protein in Human Cancer: Current Trends and Future Challenges. *Curr. Cancer Drug Targets* **18**, 222–230 (2018).

158. Muñoz, A. & Costa, M. Elucidating the mechanisms of nickel compound uptake: A review of particulate and nano-nickel endocytosis and toxicity. *Toxicol. Appl. Pharmacol.* **260**, 1–16 (2012).

159. Tallkvist, J., Bowlus, C. L. & Lönnerdal, B. Effect of iron treatment on nickel absorption and gene expression of the Divalent Metal Transporter (DMT1) by human intestinal Caco-2 cells. *Pharmacol. Toxicol.* **92**, 121–124 (2003).

160. Poetz, O., Luckert, K., Herget, T. & Joos, T. O. Microsphere-based co-immunoprecipitation in multiplex. *Anal. Biochem.* **395**, 244–248 (2009).

Isolation of STEAP1 using GG microspheres

Chapter 7 – Appendices

Appendix 1 – Optimization batch capture comparison for nickel- and calcium-crosslinked GG microspheres

The differential capture performance for nickel- and calcium-crosslinked microspheres for the ionic exchange strategy was assessed according to the *Optimization Batch* conditions outlined in section 4.3.1, following the optimized parameters for detergent solubilization, lysate concentration and microsphere to buffer ratios. However, instead of the typical 35 mL GG microspheres to 6 mL buffer, the following comparison was conducted under reduced ratios of 6 mL GG microspheres to 1 mL buffer. The results from the *Comparison Batch* can be seen Figure 1. The capture and elution profiles were very similar for both types of microspheres. However, calcium-crosslinked GG microspheres appear to have had less complexation than their nickel counterpart.

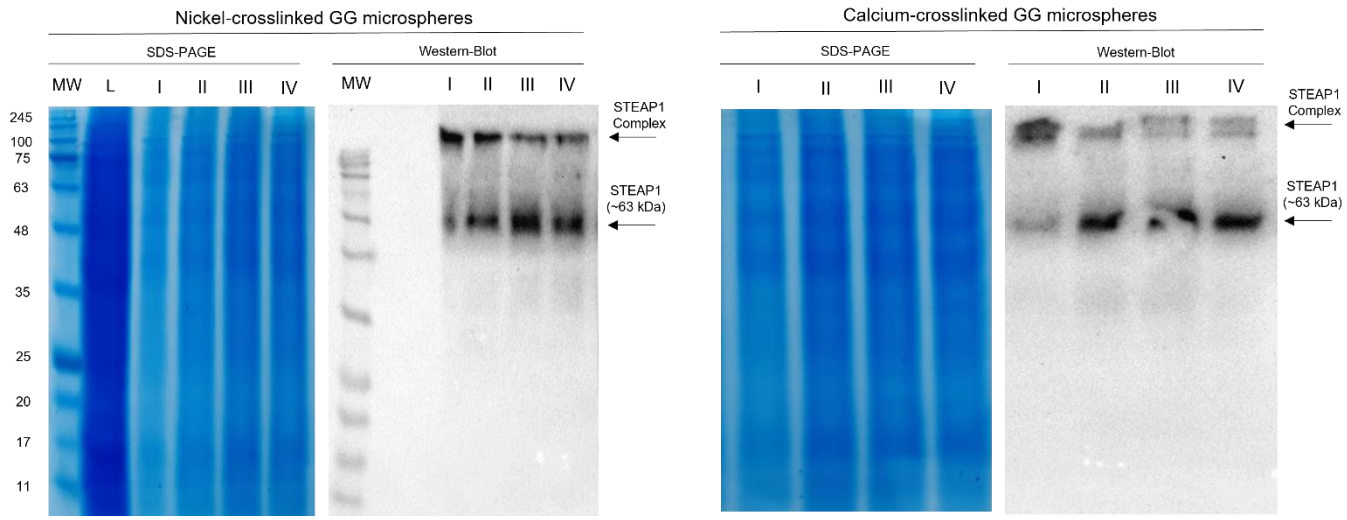

Figure 1. SDS-PAGE and Western-blot of the recovered supernatants from the *Comparison Batch* for nickel- and calcium-crosslinked GG microspheres; L – control lysate; I – Sample that did not bind to GG microspheres at 10 mM MES pH 6.2; II – Washing step with 10 mM Tris pH 8; III – Elution step with 10 mM Tris pH 9.2; IV – Elution Step with 10 mM Tris pH 11.

Note: The lysate band in the western-blot membrane for nickel-crosslinked GG microspheres (between MW and line I; not displayed) was "hiding" the signal from the batch samples, so we had to cover it. In turn, this caused the line I in the membrane to also be slightly hidden.

Isolation of STEAP1 using GG microspheres

Chapter 8 – Annexes

Annex 1 - Gellan gum microspheres and their applications in the biomedical industry

D. Gomes[1,2,3], J.P. Batista-Silva[1], J. Barroca-Ferreira[1,2,3], D. Costa[1], A. Sousa[1]*, L.A. Passarinha [1,2,3,4]*

[1]CICS-UBI - Health Sciences Research Centre, University of Beira Interior, 6201-506, Covilhã, Portugal

[2]UCIBIO–Applied Molecular Biosciences Unit, Department of Chemistry, NOVA School of Science and Technology, Universidade NOVA de Lisboa, Caparica 2829-516, Portugal

[3]Associate Laboratory i4HB - Institute for Health and Bioeconomy, NOVA School of Science and Technology, Universidade NOVA, 2819-516 Caparica, Portugal

[4]Laboratório de Fármaco-Toxicologia-UBIMedical, Universidade da Beira Interior, Covilhã, Portugal

*Corresponding authors:

L.A. Passarinha

Postal address: UCIBIO – Applied Molecular Biosciences Unit, Department of Chemistry, NOVA School of Science and Technology, Universidade NOVA de Lisboa, 2819-516 Caparica, Portugal.
Phone: +351 275 329 002
Fax: +351 275 329 099
E-mail: lpassarinha@fcsaude.ubi.pt

A. Sousa

Postal adress: CICS-UBI - Health Sciences Research Centre, University of Beira Interior, 6201-506, Covilhã, Portugal

Phone: +351 275 329 002
E-mail: angela@fcsaude.ubi.pt

Abstract

Gellan gum is a natural anionic exopolysaccharide composed of a tetrasaccharide structure of glucose, glucuronic acid, and rhamnose units. It is available in two forms, high acyl, and low acyl gellan gum, and has been used to produce different types of materials, from hydrogels to microspheres. The growing interest in gellan gum microspheres in pharmaceutical and biomedical research confirms their potential use as an effective matrix for drug delivery systems and tissue engineering. Among the well-known gellan gum properties the biocompatibility, mucoadhesive capacity, gelling, malleability, and versatile texture remain the most attractive. This chapter gives an overview of the characteristics and methods for gellan gum microspheres' production, as well as, a comprehensive discussion on both microspheres' applicability in the biomedical field and on current efforts of its suitable translation to industry.

1. Introduction

Natural polymers, such as polysaccharides, have become increasingly important over the last decade due to their wide range of industrial applications, ranging from food (1, 2) to medicine (3, 4). Specifically, microbial polysaccharides are ubiquitous in nature, nontoxic, biodegradable, environment friendly, and continue active at extreme conditions of temperature, pH, and salinity. Due to their superior properties, they are excellent alternatives to replace synthetic and other natural gums. In fact, their inherent biocompatibility and apparent non-toxicity allow natural polymers to be used in a variety of medical applications, such as scaffolds or matrices in tissue engineering, drug delivery methods, and wound dressings. These characteristics make them more appealing when compared to polysaccharides derived from microalgae or plants (5, 6). These water-soluble polymers can be ionic or non-ionic and are composed of long monosaccharide unit chains linked by glycosidic bonds. Among the heteropolysaccharides, Xanthan Gum and Gellan Gum (GG) are the most studied in terms of food, cosmetics, pharmaceutic and biomedicine (7-10).

Gellan Gum is a linear, anionic exopolysaccharide, mainly produced by *Sphingomonas paucimobilis* (11) and *Sphingomoas elodea (12),* being composed of a tetrasaccharide repeating unit. This unit consists of two residues of β-D-glucose, one of β-D-glucuronate and one of α-L-rhamnose, which corresponds to 60% of glucose, 20% of rhamnose, and 20% of glucuronate (12, 13). In its native form, GG presents L-glyceryl substituents on O_2 and an acetyl group at O_6 of the same glucose residue. This gellan form is known as high acyl GG, but after commercial production, GG can be transformed into a deacetylated or low acyl gum. This conversion occurs by hydrolyzation of L-glyceryl and acetyl groups when GG is exposed to high temperatures and alkaline treatment, as represented in Figure 1 (14, 15).

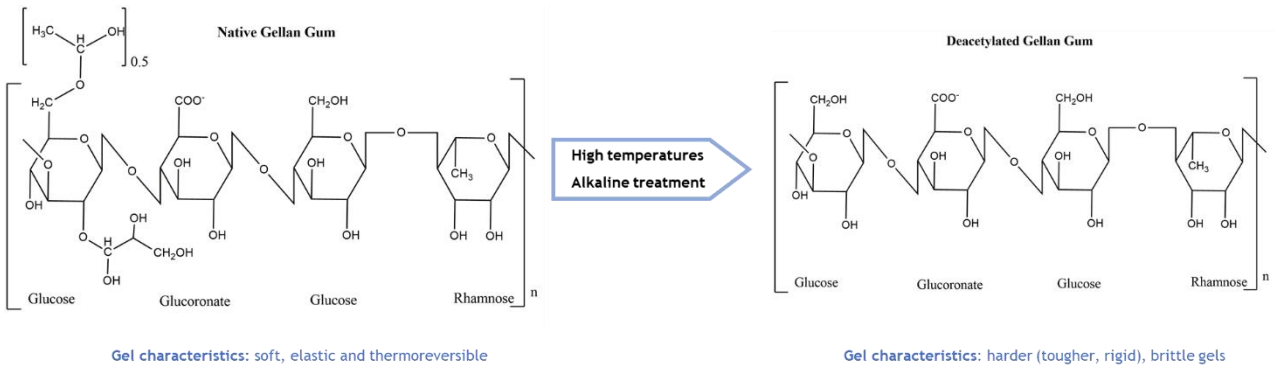

Figure 1. Influence of alkaline treatment and high temperatures on gellan gum chemical structure and its gel performance.

As other natural polymers, GG suffers from sol-gel transitions when its solution is heated and then cooled (16). Through this physical manipulation molecules of GG changed from a roughly coiled shape to highly ordered double helices. In this way, first, gellan molecules will look like random coil polymers, when dispersed in water and heated. These coils will establish hydrogen bonds and van der Waals forces with the proximate chain, creating double-helical structures on cooling. In second, the double helices aggregate and form the cation-mediated junction zone in the presence of gel-promoting cations. These cross-linkages will lead to the construction of strong gel channels, once the ions decrease the repulsive forces between the same electrostatic charges from the gellan molecule (13, 17). The hydrogel conformation and structure are affected by polymer concentration, temperature and aqueous environment, due to the type and concentration of ions present in the solution (7, 13). Gellan gum major properties include gelling, malleability and versatile texture that allow adjustable gel elasticity, biocompatibility, biodegradability and excellent thermal and acid stability (12, 13). Therefore, this polysaccharide is being explored and applied in a wide range of industries, namely in food, biotechnological, cosmetics, pharmaceutical and biomedical (3, 14). On this way, this book chapter presents and discusses general application areas of GG, different methods employed for GG microspheres production, as well as the microspheres applicability in the biomedical field and the endeavours or attempts towards translation to the industry.

2. Gellan gum applications

Gellan Gum has been widely applied in the food industry as a thickening and gelling agent. In 1992, GG was approved by the FDA to be used as a food additive, and for that reason, this is the most well-known application of GG. However, this polymer has also been explored in the cosmetic industry, among others, by its incorporation in lotions, creams, toothpaste (personal care) as a stabilizer and suspending agent due to its unique properties. The main industries, applications, and functions of GG are presented in Table 1.

Table 1. Main applications and functions of GG according to the different types of industry.

Industry	Main Applications/Products	Functions	References
Food	Beverages; Confectionary and bakery products; Dairy products; Films/coatings; Jam and Jellies; Pasteurization process; Pet and fabricated foods; Pie fillings and puddings; Water-based desserts and aspic;	Bulking, gelling and binding agent; Emulsifier; Stabilizer; Texturizer; Thickener;	(15, 18)
Pharmaceutical	Ophthalmic and Nasal formulations; Oral drug delivery;	Adherence; Delivery (sustained-release) and encapsulating agent;	(3, 7)
Cosmetics	Creams; Face masks; Haircare products; Lotion; Toothpaste	Stabilizer; Suspending agent;	(14)
Biomedical	Surgery; Tissue Engineering; Wound healing	Encapsulating agent; Injectable carrier; Scar formation prevention;	(13)
Biotechnology	Microbiological media; Plant tissue culture; Recovery of therapeutic biomolecules	Gellifier; Capturing agent; Chromatographic matrix;	(7, 14) (19-21) (22)

For the food industry, GG adds structure to confectionary and bakery products, shortens the setting time of starch jellies, and prevents moisture fluctuations in sugary foods (15, 18). Typically, the GG concentration required to produce the aforementioned products corresponds to one-fifth of the agar used (18). GG can also be applied to replace pectin in jam and gelatin in water-based gels at low concentrations (about 0.4 %). In addition, GG is used to provide a structural consistency by partially replacing starches in pie fillings and puddings, as well as to give shape to fabricated food (pet food, fruit pieces, or meat chunks), because gellan gum does not melt during pasteurization, allowing the preservation of the product organoleptic characteristics. Nowadays, GG can be considered an outstanding multifunctional agent, based on the applications discussed above, since it is resistant to a variety of environmental conditions (7, 14, 18).

For biomedical and pharmaceutical industries, GG has been blended with several polymers and used in gene therapy (23), as biocides in the prevention of spreading of microbial infections (24), in scaffolds for bone and cartilage regeneration (25, 26), in wound healing cell adhesion (27, 28), and as a pharmaceutical excipient for nasal (29, 30), ocular (31), gastric (32), and colonic drug delivery (33). Moreover, GG can be used

in the manufacture of easy-to-swallow solid dosage forms such as gels and coated tablets, as well as in oral drug delivery as a disintegrating agent in instantaneous release tablets (3, 14). Besides acting as a disintegrating agent, hydrocolloid beads based on GG are easily used for controlled, nonstop, or slow release of a variety of drugs by modifying the rate of active ingredient release (7, 13). Gellan gum can also be used to regulate the bioavailability of ophthalmic solutions, allowing a longer residence time in tear fluid than typical saline solutions.

In the last decades, GG has been used in tissue engineering for cartilage reconstruction due to its mechanical properties, as well as in 3D scaffolds via the production of polycaprolactone-based blends (12). Recently, GG has been investigated as an injectable carrier for autologous cells, such as bone marrow cells or chondrocytes, due to its ability to gel inside the body and efficiently adapt to the deficiency site to renovate the cartilage. As a result of its biocompatibility and non-toxicity, gellan can be incorporated in wound dressing designed to prevent postsurgical adhesion and scar formation (3, 14). Besides these characteristics, GG also presents important properties for its use in chromatography as hydrophilicity, porosity, high binding capacity, and negative charge to establish ionic interactions with charged biomolecules (17, 22).

Considering that the GG market is expected to grow from 43.92 million dollars (2018) to 54.47 million dollars in 2025 (34), we can claim that this polysaccharide has gained importance among several industries. Furthermore, its unique properties, versatility, stability, biocompatibility, and biodegradability, the wide range of applications, as well as, the great and increasing number of patents filing suggest that GG has been adopted as one of the most important commercialized bacterial exopolysaccharides.

3. Methodologies for the microspheres production

Microparticles, microspheres, or microcapsules are usually applied as drug delivery systems due to their great structural and functional advantages, which allow acceptable drug administration through numerous routes (35). Microspheres with an average particle size ranging from 1-1000 μm can be characterized as either a homogenous or heterogeneous structure, depending on the processing from a variety of synthetic and natural materials by applying different strategies. Figure 2 depicts some methods for the microspheres formulation.

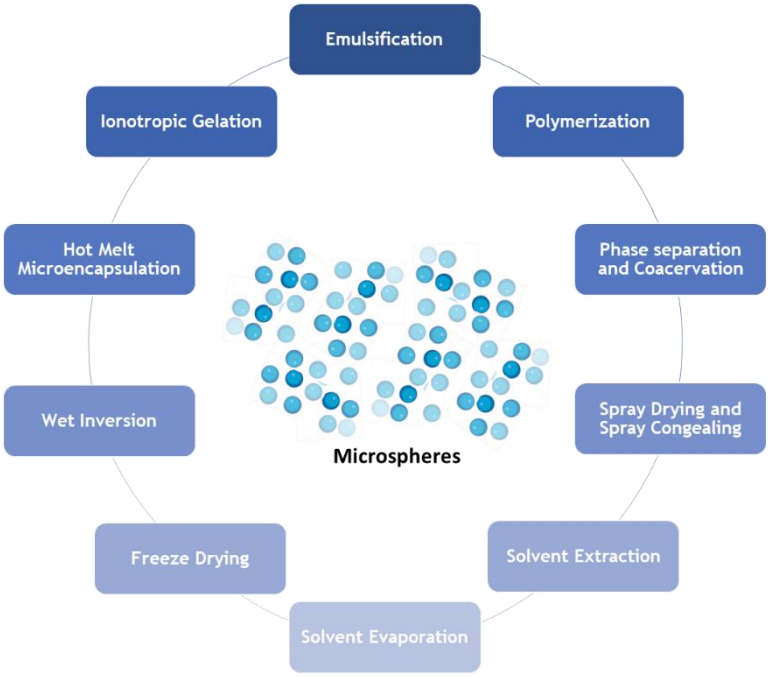

Figure 2. Typical methods for microspheres formulation.

The selection of the method for the preparation of the microspheres depends mainly on the polymer nature, drug characteristics, therapy duration, and reproducibility. When preparing microspheres, some factors as particle size requirement, polymer/drug ratio, stability, and morphology are important to control (36). The most important and applied methods for the GG microspheres formulation consist of emulsification, ionotropic gelation, and spray drying, as represented in Figure 3.

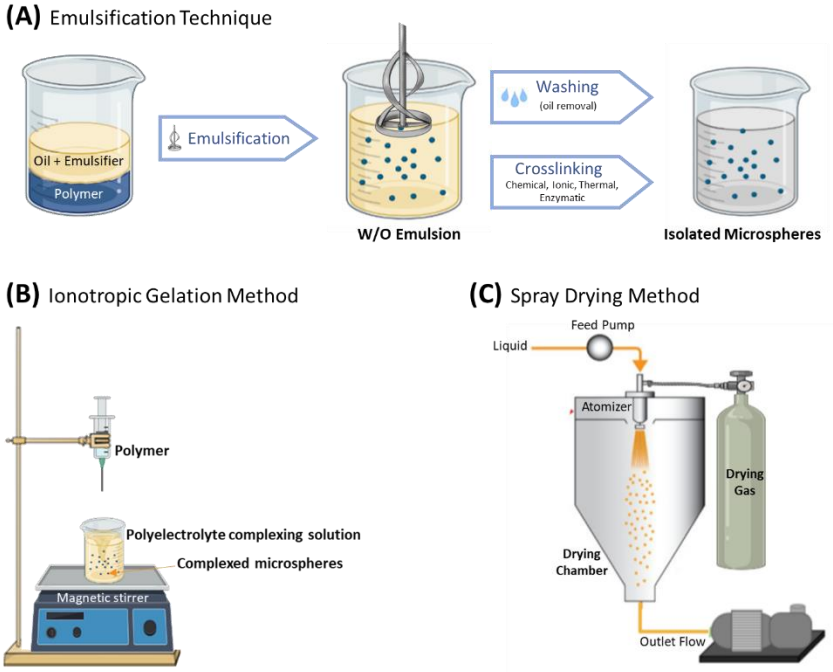

Figure 9. Most used methods for the GG microspheres formulation.

In general, the emulsification technique is used to prepare natural polymer-based carriers such as proteins and carbohydrates. Usually, the respective polymers are dissolved or dispersed in an aqueous medium before being dispersed in a non-aqueous medium, such as oil. This dissolution and addition order leads to the formation of a two-phase system, in which droplets of one liquid are dispersed into droplets of another (37). An oil-in-water (O/W) emulsion contains oil droplets dispersed in an aqueous phase, whereas a water-in-oil (W/O) emulsion contains water droplets dispersed in an oil phase (38) usually formed by agitation. For the GG microparticles preparation, it can either be applied an O/W emulsion (39) or a W/O emulsion (20, 40). This technique is very useful for industrial applications because it can be easily scaled up, but the emulsions are produced with a wide distribution of sizes and due to the strong shear conditions the incorporation of sensitive active molecules in a formulation can be difficult. The particles formed can then be crosslinked by an ionic, chemical or enzymatic method, where the most applied in GG microparticles is the crosslinking with calcium chloride (40). Furthermore, while temperature-dependent hydrogels have several advantages, including a fast gelation process in an aqueous environment, the high-water content results in potential dissolution and poor mechanical integrity. Thermal gelation and chemical crosslinking with glutaraldehyde or formaldehyde have been combined to produce stable particles in order to mitigate these drawbacks (41). For instance, Oliveira and co-workers applied a dual crosslinking with a trivalent cation and glutaraldehyde to modulate the mechanical properties of gellan/starch hydrogels (42).

Another common method applied for the GG microspheres production is ionotropic gelation due to its low cost, easiness, simplicity, and nontoxicity. It is based on the ability of polyelectrolytes to crosslink in the presence of counter ions to form hydrogel particles known as microspheres (43). As result, biomolecules can be loaded into these microspheres while still retaining their three-dimensional structure (44-47). Microspheres are spherical crosslinked hydrophilic polymeric entities capable of extensive gelation and swelling in simulated biological fluids, with drug release controlled by polymer relaxation. External and internal gelation are two types of ionotropic gelation. The main difference between these methods is the position of crosslinking ion used (external gelation – crosslinking ion is positioned externally and consequently the gelling kinetic is not diffusion-controlled, internal gelation - crosslinking ion is incorporated within the polymer solution) (48).

More recently, the spray-drying process has been used to convert particle suspensions into dry powder. It is a one-step process that can be used continuously (49). This method has been applied to form microparticles based on GG as a suitable nasal delivery system, once it is simple and reproducible (50, 51). Spray drying begins with the

polymer dissolution in a suitable volatile organic solvent, such as acetone or dichloromethane. Small droplets or a fine mist are formed when the dispersion is atomized by a stream of hot air. The evaporation step removes the respective solvent, resulting in the formation of microspheres. The cyclone module separates microparticles, which are then vacuum dried. This process has several advantages, including the ability to operate under aseptic conditions, the ability to quickly perform the process, the possibility of size/diameter microsphere control, and a homogeneous porous distribution (51, 52). Despite numerous advantages, some drawbacks emerged and are related to a low yield of microspheres and the fact that the high temperature used during the atomization process causes the inactivation of temperature-sensitive bioactive compounds (37).

4. Gellan gum-based microspheres applications

4.1. Delivery systems

Since the beginning of the 21st century, microsphere-based drug delivery systems have attracted great attention, since they offer numerous advantages based on their structural and functional abilities, over conventional drug delivery systems (such as tablets, capsules, sachets, and suspensions) (35). These “novel” systems provide controlled, sustained, and targeted delivery of drugs, minimizing fluctuations of plasma drug concentration, reducing dosing frequency and dose dumping, thereby improving patient compliance. Furthermore, they enhance the biological half-life performance of several drugs, solving physiological instability and bioavailability issues. Moreover, they exhibit more reproducible drug absorption, can mask both the taste and smell of pharmaceuticals, protect the drug from harsh physiological conditions and avoid first pass metabolism (35, 53-55). In fact, microspheres have proven to be a potent drug delivery system for specific tissue distribution due to the lower frequency of clearance by immune cells, allowing for prolonged retention time and drug release, when compared to highly researched systems, such as nanoparticles. Additionally, due to the greater size of microspheres, they can entrap larger amounts of the drug, favouring a more prolonged and constant therapeutic effect (35, 53-56).

Recently, natural hydrophilic polymers attracted the attention of researchers as they have extreme potential in the field of controlled drug delivery, due to their natural abundance, hydrophilicity (which allows swelling properties), excellent biocompatibility, cost-effective production methods, biodegradability, and sustainability (56-58). Among naturally occurring biodegradable polymers, GG has stood out for drug delivery applications in the form of microspheres. GG is an anionic heteropolysaccharide

possessing all the aforementioned characteristics, as well as adequate gelling properties and astonishing mucoadhesive capacity, surpassing those of commonly used polymers, such as chitosan (58, 59). Furthermore, GG structure is rich in functional groups (carboxyl and hydroxyl) that can be physically or chemically modified, in order to tailor drug release rate to the desired profiles (58).

When devising a GG-based drug delivery system, there are several parameters that need to be considered in order to obtain the desired particle size and distribution, drug entrapment efficiency, swelling properties, mucoadhesion and drug release rate. Typically, the most common methods for GG microsphere formulation for drug delivery applications are ionotropic gelation and W/O emulsion. In order to achieve desired microsphere characteristics through these methods, it is essential to regulate polymer concentration, crosslinker levels, crosslinking time and drug: polymer ratio (60). Fine tune control of these variables has been exhaustively reported towards the successful controlled release of several therapeutic agents, such as anti-inflammatory (58, 59, 61), antibiotics (62), triptan drug (63), antioxidant compounds (33), β-blockers (64), hypoglycemic agents (65), anti-fibrinolytic agents (66), among others. Furthermore, polymer and crosslinker concentration seem to play a key role in drug release kinetics. The GG microsphere release can be expressed as a complex system depending on the extent and rate of GG swelling, rate of drug diffusion from the GG matrix and the GG microsphere dissolution/erosion. The general tendency is that an increase in polymer concentration will result in the improvement of the swelling capacity, resulting in a diminished drug diffusion and leading to a delay on GG matrix erosion (60). Also, an increase in crosslinker concentration can be able to delay the GG erosion, by the formation of a denser and more compact polymer network, resulting in a more prolonged release of the therapeutic compound (57).

Recently, Dhanka and coworkers developed Methotrexate loaded GG microparticles (MTX-GG MPs) for drug delivery applications through a simple W/O emulsion solvent diffusion method with homogenization (56). The prepared MTX-GG MPs were spherical with a rough surface and a mean size of 4.22 μm. Additionally, the Encapsulation Efficiency (EE) of MTX-GG MPs was found to be up to 84.8%, highlighting the desirable EE. The MTX-GG MPs were able to produce a sustained and controlled release for over 24h, releasing 84% of total MTX. Furthermore, the microsphere system was biocompatible with L929 fibroblast cells and hemocompatible with human red blood cells (56). The authors underlined the future applicability of the *in vivo* MTX-GG MPs injection. Notwithstanding, GG-based systems, owing to their excellent mucoadhesive and *in situ* gelation features, have been mostly explored in routes of administration where a mucous membrane is present, in particular, the oral and nasal route. In fact, this

just accentuates the versatility and potential of GG microspheres as a controlled release drug delivery system.

4.1.1 Nasal Formulations

Traditionally, the nasal cavity was mostly used for the treatment of local diseases, such as rhinitis, nasal congestion, and allergic symptoms (62, 63). In the past few years, the nasal route has grown in popularity as a convenient and suitable route with many therapeutic advantages for the systemic delivery of drugs. These advantages include, but are not limited to, a large surface area, the porosity of the endothelial basement membrane minimizing the physical barrier aspect and the presence of a highly vascularized epithelial layer, which in turn, enhances blood flow (63). Furthermore, it avoids liver first pass metabolism, harsh gastrointestinal tract (GIT) conditions (pH and enzymatic degradation), allowing thusly improved patient compliance (62). Moreover, the nasal route is non-invasive and has been shown to bypass the blood-brain barrier, directly targeting the central nervous system (50). The major drawback of nasal drug delivery is the rapid and efficient nasal mucociliary clearance. This system is in place to protect the respiratory system from damage/toxicity from inhaled substances. In fact, it has been reported that the half-life of clearance can be near 15 minutes (67). This mechanism severely limits the drug absorption, and, by consequence, a very low nasal bioavailability is observed (68).

To circumvent this issue, mucoadhesive microsphere drug delivery systems arise as a promising tool to control the rate of nasal clearance and improve drug absorption. Naturally, GG-based microspheres have been employed to overcome these constraints. Nasal administration of dry powdered GG microspheres results in rapid swelling of microspheres as they absorb water from the nasal mucosa. In addition, GG microspheres interact with cations present in the nasal fluid, promoting an *in situ* gelation, forming a highly viscous gel (60, 63). As the nasal mucosa gets dehydrated due to moisture uptake by GG microspheres, a process of cell shrinkage occurs, providing temporary physical separation of the tight junction, which in response, increases the drug absorption rate (63). Therefore, the formed GG gel can reduce mucociliary clearance, leading to a high retention time of formulations, favouring a controlled and prolonged release of the target drug (60, 63, 69).

Almotriptan malate loaded GG microspheres (ALM-GG MPs) have been formulated by W/O emulsification cross-linking technique (with $CaCl_2$ as the cross-linking agent) for the acute treatment of migraines (63). A design of experiments tool was employed to obtain an optimized formulation, which exhibited microsphere yield and drug incorporation efficiency of 93.16% and 91.65%, respectively. The produced

microspheres had a mean size of 24.86 μm and were found to be spherical in shape with a smooth surface, lacking in pores or ruptures. Such structure had previously been reported as ideal to minimize clearance time and obtain a good deposition pattern in the nasal cavity (63). The ALM-GG MPs were negatively charged, due to the anionic character of GG. This characteristic is desirable since anionic polymers have been proven to be more effective in bioadhesive endeavours over polycations or non-ionic polymers. This morphology resulted in the adhesion of 95.48% of the formulations onto a strip of sheep nasal mucosa. This large mucoadhesion resulted in an *in vitro* controlled release of ALM throughout 8 h. Furthermore, storage stability tests revealed that ALM-GG MPs do not undergo degradation upon storage, making them a suitable carrier for the nasal administration of ALM (63).

Mahajan and colleagues reported the preparation of a novel GG microspheres system for the intranasal delivery of Ondansetron, through a standard spray-drying method (67). The prepared microspheres ranged from 9.5-11.5 μm and possessed a spherical shape with smooth surface morphology. The most prominent formulation encapsulated 94.03% of total drug content, exhibited large mucoadhesive capacity and sustained the *in vitro* release of Ondansetron beyond 5 h (67). The *in vivo* performance of GG microspheres was tested at a later time and compared to an oral and intravenous formulation (70). The results show that Ondansetron peak concentration was significantly higher than that exhibited by the oral route. In addition, *in vivo* performance of GG microspheres demonstrated enhanced bioavailability in comparison to oral administration ($AUC_{0\text{-}240}$ 44.04 and $AUC_{0\text{-}240}$ 26.54, respectively) and comparable to that after intravenous administration, although slightly lower. Nonetheless, Mahajan and colleagues were able to show that Ondansetron loaded GG microspheres are able to astonishingly improve drug bioavailability and prolong residence time on the nasal cavity (70). This research group have also employed the spray-drying method for the formulation of GG microspheres for the nasal delivery of metoclopramide (51). The aforementioned GG microspheres exhibited very similar parameters as those loaded with Ondansetron, also yielding controlled release for over 5 h. Likewise, histopathological studies revealed that GG microspheres do not cause any detrimental effect or toxic response in the nasal mucosal cavity even when the exposure time is prolonged (51).

Gangane and his team have been leading the charge in the development of Donepezil Hydrochloride loaded GG microspheres for the management of Alzheimer's symptoms (69). They reported the formulation of a drug delivery system through a W/O emulsion cross-linking (with $CaCl_2$) method, for the intranasal delivery of Donepezil. GG microspheres ranged from 14.3 μm to 18.3 μm, which is in the ideal size range for nasal administration (69, 71, 72). Entrapment efficiency was as high as 53.6% and

formulations swelled rapidly in Simulated Nasal Fluid, which in turn, resulted in good mucoadhesion power upon a cut of goat nasal mucosa. The optimal formulation was able to sustain the controlled release of Donepezil for over 5 h, both *in vitro* and *ex vivo* experiments (69). Furthermore, GG microspheres were proven to show no damaging traits over the goat nasal mucosa. More recently, Gangane and his group were able to improve upon the GG microspheres system previously described, by employing a spray drying formulation technique (50). Donepezil loaded GG microspheres prepared through a spray drying technique were shown to be able to ensnare 86.48% of the total drug amount and significantly improve upon mucoadhesion potency (50). In addition, *ex vivo* permeation was found to be adequate (84.92%) after 4 h. The formulation was stable following 6 months of storage, as particle size, swelling capacity and mucoadhesion potential remained constant throughout this period. To sum up, GG microspheres appear to be a promising drug delivery vehicle for the intranasal administration towards the management and therapy of Alzheimer's related symptoms.

4.1.2. Oral Formulations

The oral route has been for a long time considered the most convenient and safe way of delivering therapeutic agents. The ease of administration, flexibility of formulations and enhanced patient compliance, confers to this pathway a great potential for drug delivery (60). Also, the large surface area (>300 m^2) lined with viscous mucosa opens the way for strong bioadhesion and subsequent drug absorption, resulting in efficacious drug concentrations in systemic circulation for prolonged time intervals, boosting therapeutic effect (73). Conversely, conventional oral dosage formulations can suffer from high first pass metabolism, minimizing bioavailability, as well as either low gastric retention time or rapid gastric release, resulting in local toxicity. Coupled with this, the drug can also suffer enzymatic degradation upon reaching the lower GIT, severely hindering its main effect (60, 73). Due to attributes of GG formulations, several attempts have been made with the intent of formulating and optimizing GG microspheres for oral drug delivery, by the adjustment of key process parameters (Table 2). Although general trends can be observed, it seems that drug related properties (i.e., polarity and solubility), the target site of delivery, type and degree of crosslinking, as well as drug to polymer affinities and drug to crosslinker interactions might be able to alter the entrapment efficiency and drug release kinetics.

Gellan Gum microspheres loaded with tranexamic acid (TA) have been prepared by a simple sol-gel transition induced by ionic crosslinking with aluminum (66). Spherical TA-GG microparticles (EE ranging from 71.15% to 89.12%) presented a very low cumulative release of only around 10% in acidic media (pH 1.2) after 2 h. Upon

switching to an alkaline media (pH 7.4), the release rate was increased, resulting in controlled TA release for over 8 h. This data was in agreement with swelling data, meaning that GG microspheres swelled rapidly in pH 7.4 and remained somewhat unphased in acidic media (66). This behavior can indicate that GG microspheres have the ability to transverse gastric fluid largely unscathed and reach the intestinal portion of the GIT, where site-specific drug release could be achieved. The *in vivo* pharmacokinetic evaluation revealed that GG microspheres were able to double circulation time in rabbits, as the elimination rate constant was approximately halved, along with significantly improving bioavailability (66). These results are very similar to those reported by Allam and coworkers for Metformin (MT) loaded in GG microbeads (74). As a matter of fact, the MT-GG microspheres formulation F5 performance was compared to commercially available MT extended-release tablets and MT immediate-release tablets, in healthy human volunteers. MT-GG-F5 exhibited the lowest elimination rate constant, the highest bioavailability (AUC_{0-24} (mg) of 246.74 ± 26.81) and the highest biological half-life, exceeding the marketed products. In fact, $t_{1/2}$ was 5 fold that of an average MT oral solution (74).

Recently, quercetin loaded GG microspheres were developed by ionotropic gelation in an attempt to improve quercetin intestinal stability and anticancer activity (75). Quercetin incorporation efficiencies ranged from 58.56-93.71%, increasing with the improvement in crosslinker ($CaCl_2$) concentration. Swelling and drug release profiles followed the trend of TA and MT containing GG microspheres, exhibiting pH-dependent behaviour, sustaining quercetin release for over 32 h (75). Furthermore, GG microspheres were able to enhance the chemical stability of quercetin in Simulated Gastric Fluid (SGF) and Simulated Intestinal Fluid (SIF) in comparison with free quercetin (remaining quercetin in SGF after 8 h: 99.37% *vs* 57.49% and SIF after 48 h: 50.47% *vs* 24.59%) (75).

Table 2. Impact of process variables on EE and Drug Release Profile.

Delivery System	*Production Method*	*Model Drug*	*Main findings*	*Reference*
GG Microspheres	Ionotropic Gelation with Al^{3+} crosslinking	Ketoprofen	High polymer concentration (1% to 2%) led to increase in particle size and circularity and enhanced EE; Low Al^{3+} concentration (3%) benefited drug EE; Drug release was pH-dependent and GG microspheres severely reduced release rate *vs* free drug.	(59)
	Ionotropic Gelation with $MgCl_2$, $BaCl_2$, $CaCl_2$, $CuCl_2$ and $ZnCl_2$	Azathioprine	Between metal ions, Mg^{2+} and Ba^{2+} significantly decreased the drug solubility; EE of GG beads is higher in the presence of transition elements (Cu^{2+} and Zn^{2+}) than to alkaline earth metal ions; EE tends to increase with a decrease in the pH of the ionotropic medium.	(76)
	W/O Emulsion Crosslinking with Ca^{2+}	Rifampicin	Increase in crosslinker concentration (up to 5%) caused an improvement in EE, while variations in curing time and pH did not impact EE significantly; Increase in drug:polymer ratio had a negative effect on EE; Drug release was pH-sensitive and was similar to marketed formulation.	(77)
	Ionotropic Gelation with Ca^{2+} crosslinking	Diclofenac Sodium	EE was high at low pH of the ionotropic solution, low agitation and low drug quantity; GG beads produced with low pH of the ionotropic medium and low drug:polymer ratio demonstrated a more controlled drug release profile, whereas agitation did not influence significantly the drug release profile.	(78)
	Ionotropic Gelation with Ca^{2+} and Zn^{2+} crosslinking	Cephalexin	Increase in drug loading and pH of ionotropic medium significantly enhanced EE, as well as an increase in particle size; Drug release rates were high when the % of drug loading is more accentuated; GG Beads prepared in basic pH media were able to sustain a slow cephalexin release.	(79)
Sodium Alginate: GG Microspheres	W/O Emulsion Crosslinking with Ca^{2+}	Metformin HCl	Higher GG concentration led to an increase in EE and decrease in drug release (sustained release for 8 h);Increase in Ca^{2+} % and crosslinking time had a negative effect in EE, although high Ca^{2+} % can also decrease the rate of drug release.	(65)

In turn, 5-Fluorouracil loaded gellan gum-ethyl cellulose (5-FU GG-EC) microspheres were produced by a simple O/W emulsion technique by dripping 5-FU GG-EC emulsion into a counter ion solution comprised of calcium chloride and zinc sulfate (80). As GG and EC concentration increased, so did entrapment efficiency, particle size and sustained drug release, spanning over 12 h. Cytotoxicity analysis on HT-29 human colon cancer cell lines indicated that the designed formulations decreased cell viability gradually and continuously, enhancing the anticancer activity of 5-FU, reducing systemic toxicity and unwanted side effects (80). Considering that quercetin has been shown to synergistically induce sensitivity to 5-FU through p53 modulation in colorectal cancer cells (81), a combinatorial approach of delivery of quercetin loaded GG microspheres, followed by 5-FU GG-EC microspheres could significantly enhance site-specific therapeutic effect in colorectal cancer. Not only quercetin, but other polyphenols can be employed in the proposed strategy. Resveratrol plays a chemopreventive role on colorectal cancer and it has been shown that 5-FU resistant colorectal cancer cells are more susceptible to the effect of 5-FU when Resveratrol is employed in a combined formulation (82). Prezotti and collaborators have explored the colon-targeted delivery of Resveratrol employing GG**:**Pectin microspheres (33). GG:P (4:1) microbeads, produced through ionotropic gelation, were able to encapsulate 75.7%±0.8% of Resveratrol and minimize release in acidic media, seeing as only 17.6% of the drug was released after 120 min. Upon reaching enteric pH (6.8), GG:P microparticles were shown to control the drug release upwards of 48 h without burst effects (33). The encapsulation of Resveratrol in the GG:P microsystem was biocompatible with Caco-2 and HT29-MX intestinal cell lines, besides substantially reducing drug permeation in an *in vitro* triple co-culture cell model, mimicking the human intestinal epithelium, phenomenon that may favour the accumulation of Resveratrol in the colon (33).

Several attempts have been made in order to develop GG-based systems to encapsulate a variety of drugs for delivery to the upper portion of the GIT. However, low drug incorporation, reduced floating time, extended floating lag time and burst release have been serious challenges (83). So, GG drug delivery systems with the addition of low density oil (84), modified surfaces (85) and incorporation of effervescent materials (86) have been designed in order to deal with the drawbacks described above. GG microspheres, loaded with acetohydroxamic acid and calcium carbonate with a chitosan coating, were developed with the stomach site-specific delivery in mind for the treatment of *Helicobacter pylori* infections (86). Formulated microspheres showed adequate drug EE, which increased with high polymer concentrations, and presented an exceptional floating ability with a floating lag time as low as 4.89 min. Upon contact with an acidic medium, the calcium carbonate effervesced, releasing carbon dioxide, which imparted

the microspheres with buoyancy (86). The overall bulk density of GG formulations became lower than that of the gastric fluid and without affecting gastric emptying rate, they remained buoyant in the stomach (53), which allowed for controlled release of acetohydroxamic acid for over 8 h. Furthermore, the *in vivo* floating efficiency was appropriate, and microbeads were able to achieve complete growth inhibition of *H. pylori* after only 12 h (86). On the other hand, a blend of Sodium Alginate and GG with an EC coating was prepared to provide gastroretentive delivery of Amoxicillin for *H. pylori* treatment (85). Immediately after exposure to SGF, entrapped calcium ions leak out of microspheres, leaving small cavities on the network surface, resulting in a buoyant *in situ* porous microballon system, which in combination with the small size of formulations, allowed for buoyancy efficiency upwards of 98%. The *in vivo* mucoadhesion was approximately 80% and gastrorentetive drug release from SA:GG-EC formulations was found to be exceptional, considering that the total drug concentration from formulated microspheres was nearly 7-fold higher than plain amoxicillin in rats gastric mucosa. In addition, buoyant formulations showed 100% bacterial clearance in gerbils post 3 days of the administration, unlike plain amoxicillin (85). The mucoadhesion potency and *in vitro* growth inhibition are in line with previously reported Amoxicillin loaded GG microspheres coated with 1% chitosan (62).

The conjugation of different polymers with individual properties that can act synergistically in the final formulation, whether it be blends, coatings, or InterPenetrating Networks (IPN), can impart steric bulkiness to the polymers which provide protection to the matrix and alters dissolution/erosion rates, resulting in sustained drug release (64, 83, 87). In addition, the large free matrix volume present contributes to easy and high drug loading onto the microspheres (58, 88). Several GG-based structures have been developed with these advantages in mind. A drug delivery system based on GG/pectin blend was found to be efficacious in encapsulation of ketoprofen and, consequently, the sustained release for a total of 6 h (58). Also, GG microspheres coated with chitosan presented much higher drug encapsulation and controlled release when compared to GG blank microspheres (44). Furthermore, GG/Xanthan Gum microspheres obtained through an emulsion technique have been added to a Collagen/Gelatin/Hydroxyethyl Cellulose porous matrix (89). The incorporation of the microspheres modulated the porosity, density and swelling properties of the Collagen/Gelatin/Hydroxyethyl Cellulose sponges (89). The abovementioned strategy could be employed in a combinatory tissue engineering and drug delivery perspective. The sponge could be used as a primary hydrogel-like wound healing agent, while the microspheres deliver anti-inflammatory and anti-bacterial/anti-viral drugs. In fact, a similar tactic was employed for the delivery of Stavudine, a drug

highly utilized in the treatment of HIV infection (90). Stavudine loaded Eudragit RSPO microspheres, prepared by a solvent evaporation procedure, were further embedded in GG microbeads by a simple ionotropic gelation method. Drug entrapment efficiency from composite microbeads was 6.5 times higher than to GG microsphere models. The *in vitro* drug release analysis indicated that embedded microspheres were able to considerably slow the release rate and sustain it for at least 9 h. The GG matrix acts as a secondary carrier to the diffusion of Stavudine from the core of Eudragit RSPO, thusly resulting in an enhanced gradual and continuous effect (90).

Jana and collaborators described the preparation of Aceclofenac loaded unsaturated esterified Alginate/GG microspheres. Briefly, a uniform dispersion containing Sodium Alginate, GG and Aceclofenac was extruded dropwise into a counter-ion solution containing maleic anhydride, aluminum chloride or both compounds (61). As soon as the dispersion is extruded into the counter-ion solution, maleic anhydride-induced esterification takes place, resulting in covalently crosslinked gels, carrying unsaturated substituents (i.e., maleate semi-esters) on the polysaccharide backbone. This chemical composition can be the reason to produce stronger gels and reduce the drug release rate. This behavior was observed by these authors, as the optimal formulation F10 (1% (w/v) SA; 1% (w/v) GG; 1% (w/v) Aceclofenac; 3% (w/v) maleic anhydride) encapsulated 98.46±0.40% of Aceclofenac and slowed the release rate noticeably, sustaining it for 6 h, far surpassing the results observed by standard ionotropic gelation with Aluminium (61). Furthermore, after release from F10 microspheres in plasma, the Aceclofenac absorption was sustained for over 7 h in white rabbits and exhibited potent anti-inflammatory activity in carrageenan-induced rats for a prolonged time, as it significantly inhibited paw swelling, far exceeding pure Aceclofenac (61). More recently, Jana *and coworkers* reported a novel IPN for the Aceclofenac delivery. The microspheres were prepared through a dual crosslinking method by extruding a blend of GG/Polyvinyl alcohol into a mixture of zinc and glutaraldehyde (91). Dually crosslinked GG/PVA IPN with a polymer ratio (1:1) entrapped 91.26±1.38% of the active agent and showed a sustained and controlled release of approximately 68% at the 6 h mark. The IPN formation was crucial, considering that the GG microspheres model exhibited burst release of Aceclofenac in phosphate buffer (91). The application of a dual crosslink scheme had been previously attempted for the oral delivery of Diltiazem HCl (88). Diltiazem was bound to a cation exchange resin, forming a drug-resin complex. The resinate was then entrapped within GG/Egg Albumin microcapsules, produced by either ionotropic gelation or by a covalent crosslinking method with calcium and glutaraldehyde. Although the dual crosslinked IPN microbeads were less efficient in the loading of Diltiazem, the larger extent of

crosslinking resulted in a more controlled swelling and in turn drug release pattern. In fact, GG-ALB IPNs, produced through ionotropic gelation with only calcium crosslinking, were capable of releasing the drug up to 9 h, whereas dual crosslinking IPNs extended this time up to 15 h (88).

The development of GG/PVA IPNs for the Carvedilol controlled release has also been reported for the treatment of hypertension (64). Briefly, GG, PVA and Carvedilol were mixed to get a uniform suspension. This solid-in-water suspension was emulsified into light liquid paraffin with 0.5% Span 80. Then, glutaraldehyde was added to form the final IPNs. Carvedilol was encapsulated up to 87% in the IPN matrix. The IPN tensile strength was nearly 6-fold higher than bare GG, highlighting the enhanced mechanical properties of composite microspheres. Both an increase in GG and glutaraldehyde concentration led to a decrease in swelling and total *in vitro* drug release, the latter being maintained up to 12 h (64). In addition, GG based IPNs have also been explored for other anti-hypertensive drugs. Mundargi and coworkers reported the loading of Atenolol onto Thermo-Responsive Semi-Interpenetrating Network Microspheres of GG-Poly(N-isopropylacrylamide) (92). These formulations exhibited higher swelling at 25 ºC than 37 ºC, and consequently, the Atenolol release was also fast at 25 ºC, owing to the fact that a mixture of diffusion and swelling were the responsible mechanisms for drug release. It seems that Poly(N-isopropylacrylamide) has the propensity for transition from a swollen state to a collapsed state above 32 ºC. This feature was shown to be able to work as an "on-off" cycle, by changing the temperature from 25 ºC to 37 ºC. The semi-IPN was able to sustain the release of Atenolol beyond 12 h and given the fact that drug delivery rates can be freely altered by a slight change in temperature. This Semi-IPN Microspheres of GG-Poly(N-isopropylacrylamide) can be viewed as a temperature-responsive delivery system of emergent potential (92).

Moreover, extended release composite microbeads of tamarind seed gum (TSG)-hydrolyzed-polymethacrylamide-g-GG (h-Pmaa-g-GG) have been prepared by ionotropic gelation for the oral delivery of Diclofenac sodium (87). The grafting of h-Pmaa into the GG backbone generated several ionotropical crosslinking sites, which resulted in an extensively crosslinked IPN after the addition of calcium chloride. This finding was essential, since the optimized formulation derived from a 3^2 full factorial design, was obtained with an increase in crosslinker concentration and a decrease in the h-Pmaa-g-GG:TSG ratio. The optimized formulation presented a drug EE of 93.25% and was able to lengthen drug release to a total of 10 h (87). It seems that the polymethacrylamide grafting on GG and the IPN formation allowed for improved performance over formerly related bare GG microbeads for Diclofenac delivery (78).

Additionally, a blend of whey protein isolate (WPI) and GG was investigated with the purpose of encapsulating flaxseed oil and flaxseed protein hydrolysate (FPH) through an O/W emulsion method (93). The amphiphilic character of proteins led them to the O/W interface, while the polar character of GG guided it towards the external surface, coating the microspheres. The microbeads remained stable at different salt concentrations of calcium chloride, not releasing any of the oil droplets (93). The *in vitro* digestion process was evaluated using simulated buccal (salivary) media, SGF and SIF. The microspheres were impervious to SGF, since no changes in size distribution and morphology were seen. However, they were degraded in the SIF due to the presence of pancreatin and bile extract, releasing flaxseed oil and FPH. The composite microspheres are in this manner appropriate for the small intestine site-specific delivery of bioactive compounds, assuring their functionality (93).

4.2. Tissue Engineering

Versatile properties of GG place this polymer in the spotlight for several Tissue Engineering (TE) fields. Particularly, different polymeric systems reinforced with GG-based microparticles arise as new approaches for application in cell encapsulation, creating larger surface area and mechanically improved systems, which are capable to deliver biomolecules, drugs, or cells into the injured spot. Furthermore, the non-cytotoxicity, semi-permeability, and immune protection given by these systems strengthen the promising character of their use in feasible biomedical approaches. In this topic, several clinical applications of GG microparticles will be explored.

Wang and coworkers designed a novel GG hydrogel-based microspherical cell carrier, fabricated via W/O emulsion process followed by consecutive oxidation-reduction crosslinking treatments (94). Then, a covalent coating with gelatin layers was applied to microspheres as surface-modifying ligands, to create binding affinity for human anchorage-dependent cells (ADCs). The final construct was made of a variety of gellatin-grafter-GG microspherical cell carriers (TriG) which can be accurately manipulated concerning their injectability, which permits to retain the advantages of hydrogel material and to enhance their cell affinity (94). Here, a common ADC model of human dermal fibroblasts (HDFs) and human fetal osteoblasts (hFOBs) properly attached and grew onto the surfaces of TriG, indicating a clear beneficial structure for the formation of new tissue with improved integrity and mechanical sustainability (94). Additionally, these findings suggest that TriG microspheres can assist therapeutic ADCs adhesion, proliferation, and differentiation, to further have an important role in clinical regenerative medicine for musculoskeletal, wound healing, and skin regeneration fields.

Moreover, GG-based hydrogels have been developed for tissue engineering strategies to be applied as Nucleus Pulposus (NP) substitutes in the regeneration of Intervertebral

Disc (IVD). Pereira and coworkers developed an innovative strategy based on the reinforcement of hydrogel matrix with GG microparticles under mild temperature and non-toxic conditions coupled to the absence of harsh reagents (95). In fact, the incorporation of these microparticles drastically improved the mechanical performance of the hydrogel disc (95). Similarly, these GG microparticles had the capacity to encapsulate cells or biomolecules, with a consistent distribution all over the hydrogel matrix, and to enhance its biological performance and tailor the degradation rate (95). Furthermore, the developed GG-loaded microparticles formulation revealed to be nontoxic to cells, which reinforces its role as a suitable strategy for developing substitutes for efficient regeneration of NP.

In turn, Ku and collaborators fabricated novel bioactive and biodegradable microspheres composed of Collagen I, GG, and β-TCP, by W/O emulsion method, for use as bone graft scaffold materials for bone tissue engineering applications (96). As bone repair materials, these constructs should provide appropriate mechanical properties and preserve the function of the target bone tissues. Indeed, the composite Collagen I/GG/β-TCP microspheres displayed a proper spheric surface and size, improved mechanical strength, and an excellent rate of biocompatibility (96). Despite preliminary and requiring a more detailed evaluation, this study clearly highlights the potential use of Collagen I/GG/β-TCP microspheres in bone regeneration.

Rosellini and coworkers developed a novel formulation of Gelatin/GG microparticles to be used as a cell carrier injectable scaffold in cardiac tissue engineering, particularly, for the repair and regeneration of infarcted myocardium (97). These microparticles were produced by W/O emulsion using phosphatidylcholine as a surfactant and calcium ions as crosslinker (97). Interestingly, this Gelatin/GG-based formulation was capable of mimicking the interactions that occur between proteins and polysaccharides and are found in the extracellular matrix of human natural tissues, which indicates enhanced cell compatibility (97). Furthermore, its degradation rate was compatible with the expected kinetic of cardiac tissue regeneration, offering enough support to cell growth. Also, its viscosity was suitable for injection, once it was verified increased retention of microparticles at the injection site (97). Additionally, at a biological level and in the presence of Gelatin/GG microparticles, cardiac progenitor cells preferentially adhere to the smallest to form stem cells-typical spherical aggregates, then maintaining cellular viability, integrity, and growth capacity (97). Altogether, these results suggest that gelatin/GG-based microparticles could have a promising character to be used as injectable scaffolds for myocardial regeneration, although *in vivo* models trials might be needed to confirm their appropriateness for tissue engineering.

On the other hand, Hsu and his team purposed a GG-based transarterial chemoembolization agent for liver cancer (40). In this experiment, GG was the substrate for developing a drug-carrier, being prepared into microspheres by using the W/O emulsification method, which was further merged the nano-sized drug delivery system with short-chain hyaluronic acid-histidine, polyethyleneimine-histidine, and doxorubicin nanoparticles to prepare a multifunctional complex (sHH/PH/Dox) (40). The GG-based sHH/PH/Dox nanoparticles were revealed to be suitable for long-acting vascular embolization with excellent biocompatibility (40). Likewise, this construct promptly improved the stability of the therapeutic agent doxorubicin and simultaneously increased the availability of the drug and its affinity towards cancer cells (40). This standpoint was further proved upon the analysis of the embolization behavior of GG-sHH/PH/Dox nanoparticles. Indeed, around completely ischemic necrotic tissues, these compounds achieved embolization efficacy, which indicates a promising application in the treatment of liver cancer or prostatomegaly as an embolization agent.

More recently, Zhang and coworkers constructed a novel type of biodegradable hydrogel extremely effective in preventing wound infection (98). This wound dressing material was developed by embedding drug-loaded GG microspheres within a hydrogel, previously assembled by Schiff base-mediated crosslinking between oxidized GG and carboxymethyl chitosan (98). The addition of GG microspheres, besides improving the mechanical properties of the construct, did not affect its swelling ability nor increased the crosslink density (98). These characteristics were favorable to a highly stable mechanical structure and confirmed the capacity for absorbing wound exudate and providing oxygen and nutrients to cells throughout the wound healing process (98). Moreover, GG-based microspheres greatly contributed to the release of antibacterial drugs, such as tetracycline hydrochloride, and silver sulfadiazine, in a sustained profile and with delayed-release properties, unveiling an exceptional long-term antibacterial activity against *E. coli* and *S. aureus* (98). These results support the idea that this bioactive composite hydrogel can be employed as a promising injectable scaffold for a wide variety of applications, aiming to promote wound regeneration and drug delivery under an anti-bacterial environment.

4.3. Capture strategies of therapeutic biomolecules

The biopharmaceutical market is one of the largest industrial sectors and has a huge positive impact on society, with a predicted global market of nearly 500 billion dollars in 2026 (99). Biopharmaceuticals correspond to any biologically synthesized molecule applied to treat or manage disorders and account for more than 30% of drugs in the drug pipeline (100), with hundreds of approved products on the market. Biopharmaceutical

products include monoclonal antibodies, recombinant growth factors, purified proteins, recombinant proteins, recombinant hormones, vaccines, recombinant enzymes, synthetic immunomodulators, cell and gene therapies, between other products. Proteins play an important role in clinical practice, once they can be used as a therapeutic target or applied in a specific treatment for a variety of pathologies. Nevertheless, human proteins with a great pharmaceutical value are very hard to obtain from their natural sources, being recombinant technology a very powerful tool for their production under higher amounts and low costs. In fact, the recombinant protein industry has expanded rapidly, and more than 130 recombinant proteins were approved by FDA for clinical use. However, over 170 recombinant proteins are produced and used in medicine around the world (101). On the other hand, non-viral vectors, such as plasmid DNA (pDNA), are being studied and considered in several ongoing clinical trials for gene therapy or DNA vaccine applications. pDNA vectors are particularly valuable in terms of safety since they cannot revert to virulent forms and the stability of pDNA eases its storage and shipping. Moreover, these vectors are simple to manufacture by changing nucleic acid sequences, and so, large-scale production and isolation are possible with a reduced processing time. Thus, the biotechnological platform for pDNA production is a highly cost-effective procedure (102).

The typical biopharmaceutical manufacturing follows a similar pattern of unit operations divided into two categories: upstream and downstream. Upstream unit operations usually include cell culture and harvest steps, while downstream unit operations include clarification, purification with multiple chromatographies, filtration, and diafiltration steps. Chromatography has been widely applied in biomolecules purification, since it allows the exploration of different properties of the target molecule, like charge, size, hydrophobicity and recognition of a specific ligand (103). Nevertheless, some of the applied chromatographic strategies cannot manage ‘dirty’/complex samples, since colloidal impurities commonly plug the packed-bed columns (104). The combination of a previous clarification step, using a more cost-effective technique (105, 106), with a chromatographic step can ensure the required final purity, simplify the downstream process as well as reduce the costs and the sample manipulation. The batch method has been applied for studying the purification or clarification of a crude lysate sample, applying cell beads (107), and is also suited for beaded materials, like gel beads (105). Therefore, GG becomes a great polymer to be explored as a chromatographic matrix or in capture strategies due to its porosity, hydrophilicity, high binding capacity, and ability to form gels.

Gomes and co-workers applied GG microspheres produced by a W/O emulsion, previously optimized by a design of experiments tool (20), and reinforced with several

metal ions to further application in batch methods, as alternatives to chromatographic procedures, (as presented in Figure 4 (A)). Different applications were explored with these GG microspheres. First, the direct capture of the human soluble catechol-*O*-methyltransferase (hSCOMT), an important biopharmaceutical target associated with some human dementias, from complex *K. pastoris* lysates, was accomplished by establishing two different strategies (19). The GG microspheres were reinforced with nickel ions, presenting a spherical shape with a size of 239 μm. By mimicking an immobilized metal affinity chromatography (IMAC) approach and manipulating pH and ionic strength the recovered hSCOMT bioactivity was about 200% with a purification degree of 77%. In the other strategy, gellan microspheres were crosslinked with magnesium ions, once it is known to be a cofactor of hSCOMT, thereby suggesting a natural affinity for the protein. The magnesium-crosslinked microspheres with about 300 μm diameter recovered hSCOMT with 19% of bioactivity and a purification degree of 0.73%. These findings suggest that the application of GG microspheres in a simple batch method for the direct capture of the hSCOMT from the *K. pastoris lysate* is a viable, useful, rapid, and cost-effective alternative technique to traditional clarification methods (19).

Given the interesting results and versatility of the GG microspheres in the protein capture study, the same authors explore the microspheres applicability in the direct capture of a pDNA vaccine, encoding HPV E7 oncoprotein (pDNA-E7), from an *Escherichia coli* (*E. coli*) complex lysate (21), (Figure 4 (B)). Two capture approaches were studied to take advantage of divalent copper cations used in the microspheres reinforcement and the amino groups added by the polyethyleneimine (PEI) used in the GG microspheres functionalization. Both GG microsphere formulations presented a spherical shape with a size range of 250-370 μm. Copper-crosslinked microspheres captured 15.61% of pDNA (≈15 fold more pDNA than in *Escherichia coli* lysate) with 2.42% of purity, while the copper-crosslinked microspheres functionalized with PEI improved pDNA recovery to 88.09%, with 3.18% of purity. The GG microspheres demonstrated that they can be applied in pDNA capture from crude *E. coli* lysates, without the need of using organic solvents, once they allowed to clarify and increase the pDNA recovery yield of the final sample (21).

Overall, the biotechnological industry, and in particular the isolation of therapeutic biomolecules, is a recent promising area for innovation in the design of GG. Moreover, the methods applied in these studies are simple, fast, cost-effective, which are advantages for a successful scale-up.

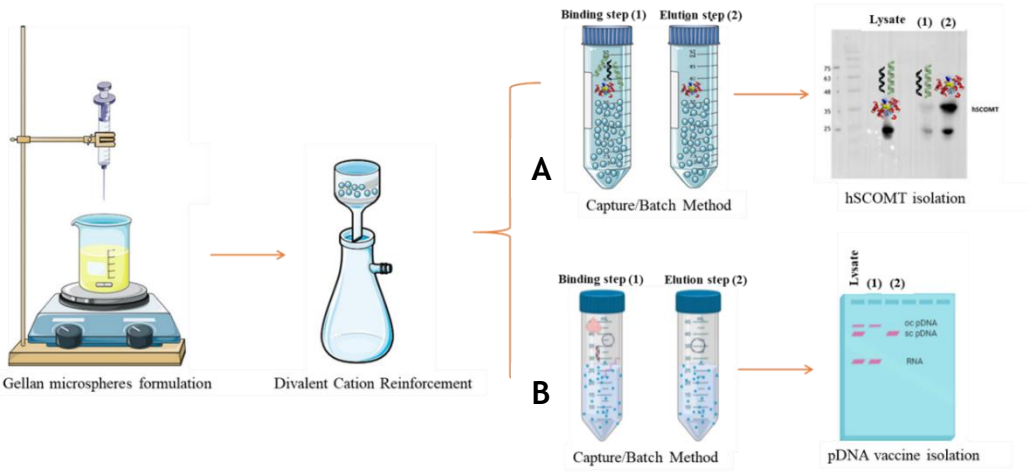

Figure 4. Schematic representation of the GG production and application to capture therapeutic biomolecules; (A) hSCOMT and (B) pDNA vaccine [adapted from (19, 21)].

5. Conclusions and Future Perspectives

Gellan gum has sparked significant research interest in a variety of fields, including biomedical and clinical applications, over the last few decades. Gellan gum has a wide range of properties, including easy bio-fabrication, tunable mechanical, cell adhesion, biocompatibility, biodegradability, gelling ability, simple functionalization, and mucoadhesion. Indeed, it is an ideal candidate for the administration and controlled release of therapeutic agents, as well as a material suitable for regenerative medicine and tissue engineering. Nonetheless, in physiological conditions, GG presents poor mechanical strength and stability, leading researchers to combine GG with other polymers to improve the GG physicochemical properties.

This chapter provides readers with information on the general applications of GG and more extensively the contemporary biomedical applications of GG microspheres, mainly in drug delivery systems, tissue engineering, and recovery of therapeutic biomolecules. We have also addressed the most commonly applied methods for GG microspheres production that are usually chosen taking into consideration the required function. These methods resulted in satisfactory yields of microspheres in terms of size and sphericity, however, some challenges remain to be solved. The main challenge consists of microspheres' large-scale production, where the key factor will be the strict control over the microsphere’s geometrical features. This is an important question that needs to be addressed in a near future to instigate translation of microspheres applicability from the lab to the industry. In addition, GG microspheres have proven to be a potent drug delivery system for local delivery since they can entrap larger amounts of the drug, favouring a more prolonged and constant therapeutic effect, reducing the dosing frequency and therefore improving patient compliance. The great variety of

studies as well as the steadily increasing number of researchers engaged in using GG-based microspheres in the biomedical field, due to their unique properties, have suggested that GG potential will be even more significant in the future. For example, GG-based microspheres can be a promising drug delivery vehicle for intranasal and oral administration, as well as, for tissue engineering due to their unique characteristics such as biocompatibility, non-toxicity, stability, and biodegradability. In addition, the application of GG microspheres as a clarification step to recover therapeutic biomolecules shows once more the great versatility of GG. This specific application has been explored recently and can be extended to other recombinant therapeutic biomolecules as a simple, fast, economic, useful and environmentally friendly way to clarify complex samples without resorting to organic solvents. All these applications strengthen the great versatility of GG mentioned throughout this chapter. The characterization and study of GG microspheres for application in the biomedical field will allow the understanding of crucial aspects of its use in drug delivery, tissue engineering, and the capture of therapeutic biomolecules. This knowledge will provide guidance for its scale-up and possible application in the biomedical industry, in particular, providing a starting point for the *in vivo* studies, followed by the clinical trials.

Finally, research in this field will undoubtedly result in many more advanced products that could be beneficial to humans in different areas in the future. Microspheres are beginning to represent a promising use in biomedical applications, being several companies already exploiting them in the pharmaceutical and health care industry.

Acknowledgments

This work was supported by FEDER funds through the POCI - COMPETE 2020 - Operational Programme Competitiveness and Internationalization in Axis I - Strengthening research, technological development and innovation (Project POCI-01-0145-FEDER-007491) and National Funds by FCT - Foundation for Science and Technology (Project UID/Multi /00709/2019). This work was also supported by the Applied Molecular Biosciences Unit UCIBIO (UIDB/04378/2020 and UIDP/04378/2020) and the Associate Laboratory Institute for Health and Bioeconomy – i4HB (project LA/P/0140/2020) which are financed by National Funds from FCT/MCTES. L.A. Passarinha acknowledges a sabbatical fellowship (SFRH/BSAB/150376/2019) from the Portuguese Foundation for Science and Technology (FCT) within the scope of POCH – Advanced Formation programs co-funded by European Social Fund and MCTES. Diana Gomes and Jorge Ferreira acknowledges, respectively, the doctoral fellowships 2020.06792.BD and SFRH/BD/130068/2017 from FCT.

References

1. Sworn G. Gellan gum. Handbook of Hydrocolloids 2009. p. 204-27.
2. Jindal N, Khattar JS. Chapter 4: Microbial Polysaccharides in Food Industry. In: Grumezescu AM, Holban AM, editors. Biopolymers for Food Design: Academic Press, Elsevier; 2018. p. 95-123.
3. Osmalek T, Froelich A, Tasarek S. Application of gellan gum in pharmacy and medicine. Int J Pharm. 2014;466(1-2):328-40.
4. Dumitriu S. Polysaccharides In Medicinal Applications. 1st Edition ed. Dumitriu S, editor: CRC Press Inc; 1996.
5. Mende S, Rohm H, Jaros D. Influence of exopolysaccharides on the structure, texture, stability and sensory properties of yoghurt and related products. Int Dairy J. 2016;52:57–71.
6. Ogaji IJ, Nep EI, Audu-peter JD. Pharmaceutica Advances in Natural Polymers as Pharmaceutical Excipients. Pharmaceutica Analytica Acta. 2012;3:1-16.
7. Bajaj IB, Survase, S. A., Saudagar, P. S., Singhal, R. S. Gellan Gum: Fermentative Production, Downstream Processing and Applications. Food Technol Biotechnol. 2007;45(4):341–54.
8. Pérez-Ramos A, Nácher-Vázquez M, Notararigo S, López P, Mohedano ML. Part II - Probiotics in Food. In: Ronald Ross Watson VRP, editor. Probiotics, Prebiotics, and Synbiotics: Elsevier Inc.; 2016. p. 329-44.
9. Hamcerencu M, Popa M, Riess G, Desbrières J. Chemically modified xanthan and gellan for preparation of biomaterials for ophthalmic applications. Polymer International. 2020;69:1051-7.
10. Ateş Ö, Toksoy Öner E. Chapter 7 - Microbial Xanthan, Levan, Gellan, and Curdlan as Food Additives. In: Gupta VK, Treichel H, Shapaval V, Antonio de Oliveirai L, Tuohy MG, editors. Microbial Functional Foods and Nutraceuticals: John Wiley & Sons, Ltd; 2017. p. 149-73.
11. Banik RM, Santhiagu A, Upadhyay SN. Optimization of nutrients for gellan gum production by Sphingomonas paucimobilis ATCC-31461 in molasses based medium using response surface methodology. Bioresource Technology Reports. 2007;98:792-7.
12. Fialho AM, Moreira LM, Granja AT, Popescu AO, Hoffmann K, Sa-Correia I. Occurrence, production, and applications of gellan: current state and perspectives. Appl Microbiol Biotechnol. 2008;79(6):889-900.
13. Zia KM, Tabasum S, Khan MF, Akram N, Akhter N, Noreen A, et al. Recent trends on gellan gum blends with natural and synthetic polymers: A review. Int J Biol Macromol. 2018;109:1068-87.

14. Prajapati VD, Jani GK, Zala BS, Khutliwala TA. An insight into the emerging exopolysaccharide gellan gum as a novel polymer. Carbohydr Polym. 2013;93(2):670-8.
15. BeMiller JN. Gellans, Curdlan, Dextrans, Levans, and Pullulan. In: BeMiller JN, editor. Carbohydrate Chemistry for Food Scientists. Third ed: Elsevier Inc.; 2019. p. 271-8.
16. Pérez-Campos SJ, Chavarría-Hernández N, Tecante A, Ramírez-Gilly M, Rodríguez-Hernández AI. Gelation and microstructure of dilute gellan solutions with calcium ions. Food Hydrocolloids. 2012;28(2):291-300.
17. Morris ER, Nishinari K, Rinaudo M. Gelation of gellan – A review. Food Hydrocolloids. 2012;28(2):373-411.
18. loannis Giavasis LMH, and Brian McNeil. Gellan Gum. Critical Reviews in Biotechnology. 2000;20(3):177-211.
19. Gomes D, Gonçalves C, Gonçalves AM, Queiroz JA, Sousa A, Passarinha LA. Applications of gellan natural polymer microspheres in recombinant catechol-O-methyltransferase direct capture from a Komagataella pastoris lysate. Int J Biol Macromol. 2021;172:186-96.
20. Coelho J, Eusebio D, Gomes D, Frias F, Passarinha LA, Sousa A. Biosynthesis and isolation of gellan polysaccharide to formulate microspheres for protein capture. Carbohydrate Polymers. 2019;220:236-46.
21. Gomes D, Costa D, Queiroz JA, Passarinha LA, Sousa A. A new insight in gellan microspheres application to capture a plasmid DNA vaccine from an Escherichia coli lysate. Separation and Purification Technology. 2021;274:119013.
22. Goncalves AI, Rocha LA, Dias JM, Passarinha LA, Sousa A. Optimization of a chromatographic stationary phase based on gellan gum using central composite design. Journal of Chromatography B. 2014;957:46-52.
23. Goyal R, Tripathi SK, Tyagi S, Ravi Ram K, Ansari KM, Shukla Y, et al. Gellan gum blended PEI nanocomposites as gene delivery agents: Evidences from in vitro and in vivo studies. European Journal of Pharmaceutics and Biopharmaceutics. 2011;79(1):3-14.
24. Novac O, Lisa G, Profire L, Tuchilus C, Popa MI. Antibacterial quaternized gellan gum based particles for controlled release of ciprofloxacin with potential dermal applications. Materials Science and Engineering: C. 2014;35:291-9.
25. Oliveira JT, Martins L, Picciochi R, Malafaya PB, Sousa RA, Neves NM, et al. Gellan gum: a new biomaterial for cartilage tissue engineering applications. Journal of biomedical materials research Part A. 2010;93(3):852-63.
26. Bellini D, Cencetti C, Meraner J, Stoppoloni D, D'Abusco AS, Matricardi P. An in situ gelling system for bone regeneration of osteochondral defects. European Polymer Journal. 2015;72:642-50.

27. Kuo SM, Chang SJ, Wang H-Y, Tang SC, Yang S-W. Evaluation of the ability of xanthan gum/gellan gum/hyaluronan hydrogel membranes to prevent the adhesion of postrepaired tendons. Carbohydrate Polymers. 2014;114:230-7.
28. Lee MW, Tsai HF, Wen SM, Huang CH. Photocrosslinkable gellan gum film as an anti-adhesion barrier. Carbohydr Polym. 2012;90(2):1132-8.
29. Cao SL, Zhang QZ, Jiang XG. Preparation of ion-activated in situ gel systems of scopolamine hydrobromide and evaluation of its antimotion sickness efficacy. Acta pharmacologica Sinica. 2007;28(4):584-90.
30. Sonje AG, Mahajan HS. Nasal inserts containing ondansetron hydrochloride based on Chitosan–gellan gum polyelectrolyte complex: In vitro–in vivo studies. Materials Science and Engineering: C. 2016;64:329-35.
31. Tayel SA, El-Nabarawi MA, Tadros MI, Abd-Elsalam WH. Promising ion-sensitive in situ ocular nanoemulsion gels of terbinafine hydrochloride: design, in vitro characterization and in vivo estimation of the ocular irritation and drug pharmacokinetics in the aqueous humor of rabbits. Int J Pharm. 2013;443(1-2):293-305.
32. Emeje MO, Franklin-Ude PI, Ofoefule SI. Evaluation of the fluid uptake kinetics and drug release from gellan gum tablets containing metronidazole. International Journal of Biological Macromolecules. 2010;47(2):158-63.
33. Prezotti FG, Boni FI, Ferreira NN, Silva DDSe, Campana-Filho SP, Almeida A, et al. Gellan Gum/Pectin Beads Are Safe and Efficient for the Targeted Colonic Delivery of Resveratrol. Polymers. 2018;10(1):50.
34. Forecast MD. Gellan Gum Market By Product Type (High Acyl Content, Low Acyl Content), By Application (Food(Confectionary, Jams and Jellies, Fabricated Foods, Water-based Gels, Pie Fillings and Puddings, Dairy Products, Processed Meats, Beverages), Personal Care and Cosmetics, Industrial and Household Cleaners, Pharmaceuticals, and Others), and By Region (North America, Europe, Asia Pacific, Latin America, and Middle East & Africa) – Global Industry Analysis, Size, Share, Growth, Trends, and Competitive Analysis Forecasts Report 2021-2026. Market Data Forecast; 2021.
35. Lengyel M, Kállai-Szabó N, Antal V, Laki AJ, Antal I. Microparticles, Microspheres, and Microcapsules for Advanced Drug Delivery. Scientia Pharmaceutica. 2019;87(3):20.
36. Bansal H, kaur SP, Gupta AK. Microsphere: Methods of preparation and applivations; A comparative study. International Journal of Pharmaceutical Sciences Review and Research. 2011;10:69-78.
37. Aguero L, Zaldivar-Silva D, Pena L, Dias ML. Alginate microparticles as oral colon drug delivery device: A review. Carbohydr Polym. 2017;168:32-43.

38. Yamashita Y, Miyahara R, Sakamoto K. Emulsion and Emulsification Technology: Theoretical Principles and Applications. In: Kazutami Sakamoto RYL, Howard I. Maibach, Yuji Yamashita, editor. Cosmetic Science and Technology: Elsevier Inc.; 2017. p. 489-506.
39. Sosa-Herrera MG, Berli CLA, Martínez-Padilla LP. Physicochemical and rheological properties of oil-in-water emulsions prepared with sodium caseinate/gellan gum mixtures. Food Hydrocolloids. 2008;22(5):934-42.
40. Hsu MF, Tyan YS, Chien YC, Lee MW. Hyaluronic acid-based nano-sized drug carrier-containing Gellan gum microspheres as potential multifunctional embolic agent. Sci Rep. 2018;8(1):731.
41. Joye IJ, McClements DJ. Biopolymer-based nanoparticles and microparticles: Fabrication, characterization, and application. Current Opinion in Colloid & Interface Science. 2014;19(5):417-27.
42. Oliveira Cardoso VM, Stringhetti Ferreira Cury B, Evangelista RC, Daflon Gremião MP. Development and characterization of cross-linked gellan gum and retrograded starch blend hydrogels for drug delivery applications. Journal of the mechanical behavior of biomedical materials. 2017;65:317-33.
43. Das B, Devi JR. Microparticulate drug delivery system - a review. World Journal of Pharmaceutical and Life Sciences. 2016;2(6):243-58.
44. Patil JS, Kamalapur MV, Marapur SC, Shiralshetti SS. Ionotropically Gelled Novel Hydrogel Beads: Preparation, Characterization and In vitro Evaluation. Indian J Pharm Sci. 2011;73(5):504-9.
45. Shirsath NR, Goswami AK. Vildagliptin-loaded gellan gum mucoadhesive beads for sustained drug delivery: design, optimisation and evaluation. Materials Technology. 2021;36(11):647-59.
46. Adrover A, Paolicelli P, Petralito S, Di Muzio L, Trilli J, Cesa S, et al. Gellan Gum/Laponite Beads for the Modified Release of Drugs: Experimental and Modeling Study of Gastrointestinal Release. Pharmaceutics. 2019;11(4).
47. Wahba MI. Processed gellan gum beads as covalent immobilization carriers. Biocatalysis and Agricultural Biotechnology. 2018;14:270-8.
48. Ahirrao SP, Gide PS, Shrivastav, Sharma P. Ionotropic Gelation: A Promising Cross Linking Technique for Hydrogels. Research & Reviews: Journal of Pharmaceutics and Nanotechnology. 2014;2(1):1-6.
49. Lopes M, Abrahim B, Veiga F, Seiça R, Cabral LM, Arnaud P, et al. Preparation methods and applications behind alginate-based particles. Expert opinion on drug delivery. 2017;14(6):769-82.

50. Gangane PS, Kawtikwar PS. Development of Donepezil Hydrochloride Loaded Gellan Gum Based Nasal Mucoadhesive Microspheres by Spray Drying Method. Indian Journal of Pharmaceutical Education and Research. 2020.
51. Mahajan HS, Gattani SG. Gellan gum based microparticles of metoclopromide hydrochloride for intranasal delivery: development and evaluation. Chemical & pharmaceutical bulletin. 2009;57(4):388-92.
52. Malik A, Parvez N, Sharma PK. Novel Methods of Microsphere Formulation. World Applied Sciences Journal. 2014;32(5):839-47.
53. Nv P, Nv W, Ss T, Sudarshan US, editors. Microspheres: A Novel Drug Delivery System2020.
54. Sharma N, Purwar N, Gupta PC. Microspheres as drug carriers for controlled drug delivery: a review. Int J Pharm Sci Res. 2015;6:4579–87.
55. Solanki N. Microspheres an innovative approach in drug delivery system. MOJ Bioequiv Availab. 2018;5:56-8.
56. Dhanka M, Shetty C, Srivastava R. Methotrexate loaded gellan gum microparticles for drug delivery. Int J Biol Macromol. 2018;110:346-56.
57. Babu RJ, Sathigari S, Kumar MT, Pandit JK. Formulation of controlled release gellan gum macro beads of amoxicillin. Current drug delivery. 2010;7(1):36-43.
58. Prezotti FG, Cury BSF, Evangelista RC. Mucoadhesive beads of gellan gum/pectin intended to controlled delivery of drugs. Carbohydrate Polymers. 2014;113:286-95.
59. Boni FI, Prezotti FG, Cury BS. Gellan gum microspheres crosslinked with trivalent ion: effect of polymer and crosslinker concentrations on drug release and mucoadhesive properties. Drug Dev Ind Pharm. 2016;42(8):1283-90.
60. Milivojevic M, Pajic-Lijakovic I, Bugarski B, Nayak AK, Hasnain MS. Chapter 6 - Gellan gum in drug delivery applications. In: Hasnain MS, Nayak AK, editors. Natural Polysaccharides in Drug Delivery and Biomedical Applications: Academic Press; 2019. p. 145-86.
61. Jana S, Das A, Nayak AK, Sen KK, Basu SK. Aceclofenac-loaded unsaturated esterified alginate/gellan gum microspheres: in vitro and in vivo assessment. Int J Biol Macromol. 2013;57:129-37.
62. Narkar M, Sher P, Pawar A. Stomach-specific controlled release gellan beads of acid-soluble drug prepared by ionotropic gelation method. AAPS PharmSciTech. 2010;11(1):267-77.
63. Abbas Z, Marihal S. Gellan gum-based mucoadhesive microspheres of almotriptan for nasal administration: Formulation optimization using factorial design, characterization, and in vitro evaluation. J Pharm Bioallied Sci. 2014;6(4):267-77.

64. Agnihotri SA, Aminabhavi TM. Development of Novel Interpenetrating Network Gellan Gum-Poly(vinyl alcohol) Hydrogel Microspheres for the Controlled Release of Carvedilol. Drug Development and Industrial Pharmacy. 2005;31(6):491-503.
65. Balasubramaniam J, Rao VU, Vasudha M, Babu J, Rajinikanth PS. Sodium alginate microspheres of metformin HCl: formulation and in vitro evaluation. Current drug delivery. 2007;4(3):249-56.
66. Bhattacharya SS, Banerjee S, Chowdhury P, Ghosh A, Hegde RR, Mondal R. Tranexamic acid loaded gellan gum-based polymeric microbeads for controlled release: in vitro and in vivo assessment. Colloids Surf B Biointerfaces. 2013;112:483-91.
67. Mahajan HS, Gattani SG. Nasal administration of ondansetron using a novel microspheres delivery system. Pharmaceutical development and technology. 2009;14(2):226-32.
68. Gizurarson S. The effect of cilia and the mucociliary clearance on successful drug delivery. Biological & pharmaceutical bulletin. 2015;38(4):497-506.
69. Gangane PS, Ghormare NV, Mahapatra DK, Mahajan NM. Gellan Gum Assisted Fabrication and Characterization of Donepezil Hydrochloride Mucoadhesive Intranasal Microspheres. International journal of current research and review. 2020;12:105-15.
70. Mahajan HS, Gattani SG. Nasal administration of ondansetron using a novel microspheres delivery system Part II: ex vivo and in vivo studies. Pharmaceutical development and technology. 2010;15(6):653-7.
71. Shekunov BY, Chattopadhyay P, Tong HH, Chow AH. Particle size analysis in pharmaceutics: principles, methods and applications. Pharm Res. 2007;24(2):203-27.
72. Yarragudi SB, Kumar H, Jain R, Tawhai M, Rizwan S. Olfactory Targeting of Microparticles Through Inhalation and Bi-directional Airflow: Effect of Particle Size and Nasal Anatomy. Journal of aerosol medicine and pulmonary drug delivery. 2020;33(5):258-70.
73. Homayun B, Lin X, Choi HJ. Challenges and Recent Progress in Oral Drug Delivery Systems for Biopharmaceuticals. Pharmaceutics. 2019;11(3).
74. Allam AN, Mehanna MM. Formulation, physicochemical characterization and in-vivo evaluation of ion-sensitive metformin loaded-biopolymeric beads. Drug Dev Ind Pharm. 2016;42(3):497-505.
75. Dey M, Ghosh B, Giri TK. Enhanced intestinal stability and pH sensitive release of quercetin in GIT through gellan gum hydrogels. Colloids Surf B Biointerfaces. 2020;196:111341.
76. Singh BN, Kim KH. Effects of divalent cations on drug encapsulation efficiency of deacylated gellan gum. J Microencapsul. 2005;22(7):761-71.

77. Rastogi R, Aqil M, Ali A, Sultana Y. Gelrite microgels for sustained oral drug delivery-formulation and evaluation. Current drug delivery. 2008;5(2):97-101.
78. Patil S, Sharma S, Nimbalkar A, Pawar A. Study of formulation variables on properties of drug-gellan beads by factorial design. Drug Dev Ind Pharm. 2006;32(3):315-26.
79. Agnihotri SA, Jawalkar SS, Aminabhavi TM. Controlled release of cephalexin through gellan gum beads: Effect of formulation parameters on entrapment efficiency, size, and drug release. European Journal of Pharmaceutics and Biopharmaceutics. 2006;63(3):249-61.
80. Sahoo SK, Sahoo SK, Behera A, Patil SV, Panda SK. Formulation, in vitro drug release study and anticancer activity of 5-fluorouracil loaded gellan gum microbeads. Acta poloniae pharmaceutica. 2013;70(1):123-7.
81. Xavier CP, Lima CF, Rohde M, Pereira-Wilson C. Quercetin enhances 5-fluorouracil-induced apoptosis in MSI colorectal cancer cells through p53 modulation. Cancer chemotherapy and pharmacology. 2011;68(6):1449-57.
82. Honari M, Shafabakhsh R, Reiter RJ, Mirzaei H, Asemi Z. Resveratrol is a promising agent for colorectal cancer prevention and treatment: focus on molecular mechanisms. Cancer cell international. 2019;19:180.
83. Chaturvedi K, Ganguly K, More UA, Reddy KR, Dugge T, Naik B, et al. Chapter 3 - Sodium alginate in drug delivery and biomedical areas. In: Hasnain MS, Nayak AK, editors. Natural Polysaccharides in Drug Delivery and Biomedical Applications: Academic Press; 2019. p. 59-100.
84. Bera H, Kumar S, Maiti S. Facile synthesis and characterization of tailor-made pectin-gellan gum-bionanofiller composites as intragastric drug delivery shuttles. Int J Biol Macromol. 2018;118(Pt A):149-59.
85. Tripathi GK, Singh S, Nath G, Dubey RK. Evaluation of pH triggers in situ porous controlled release micro balloon delivery of amoxicillin for eradication of Helicobacter pylori. Current drug delivery. 2011;8(6):667-77.
86. Rajinikanth PS, Mishra B. Preparation and in vitro characterization of gellan based floating beads of acetohydroxamic acid for eradication of H. pylori. Acta pharmaceutica (Zagreb, Croatia). 2007;57(4):413-27.
87. Nandi G, Nandi AK, Khan NS, Pal S, Dey S. Tamarind seed gum-hydrolyzed polymethacrylamide-g-gellan beads for extended release of diclofenac sodium using 3(2) full factorial design. Int J Biol Macromol. 2018;114:214-25.
88. Kulkarni RV, Mangond BS, Mutalik S, Sa B. Interpenetrating polymer network microcapsules of gellan gum and egg albumin entrapped with diltiazem resin complex for controlled release application. Carbohydrate Polymers. 2011;83:1001-7.

89. Kozlowska J, Prus-Walendziak W, Stachowiak N, Bajek A, Kazmierski L, Tylkowski B. Modification of Collagen/Gelatin/Hydroxyethyl Cellulose-Based Materials by Addition of Herbal Extract-Loaded Microspheres Made from Gellan Gum and Xanthan Gum. Materials. 2020;13(16):3507.
90. Sahoo SK, Swain S, Sen R, Sahoo D. Microspheres Embedded In Microbeads: A Novel Approach to Improve Various Controlled Release Characteristics of Highly Water Soluble Drug through Ionic Gelation Method. Indian J Pharm Educ Res. 2015;49:140–5.
91. Jana S, Sen KK. Gellan gum/PVA Interpenetrating Network Micro-beads for Sustained Drug Delivery. Materials Today: Proceedings. 2019;11:614-9.
92. Mundargi RC, Shelke NB, Babu VR, Patel P, Rangaswamy V, Aminabhavi TM. Novel thermo-responsive semi-interpenetrating network microspheres of gellan gum-poly(N-isopropylacrylamide) for controlled release of atenolol. Journal of Applied Polymer Science. 2010;116(3):1832-41.
93. Kuhn KR, e Silva FGD, Netto FM, da Cunha RL. Production of whey protein isolate – gellan microbeads for encapsulation and release of flaxseed bioactive compounds. Journal of Food Engineering. 2019;247:104-14.
94. Wang C, Gong Y, Lin Y, Shen J, Wang DA. A novel gellan gel-based microcarrier for anchorage-dependent cell delivery. Acta Biomater. 2008;4(5):1226-34.
95. Pereira DR, Silva-Correia J, Caridade SG, Oliveira JT, Sousa RA, Salgado AJ, et al. Development of gellan gum-based microparticles/hydrogel matrices for application in the intervertebral disc regeneration. Tissue engineering Part C, Methods. 2011;17(10):961-72.
96. Ku K, Lee M, Kuo SM, Yao C, Chang S, editors. Preparation and evaluation of collagen I/ gellan Gum/β-TCP microspheres as bone graft substitute materials. 2013 35th Annual International Conference of the IEEE Engineering in Medicine and Biology Society (EMBC); 2013 3-7 July 2013.
97. Rosellini E, Barbani N, Frati C, Madeddu D, Massai D, Morbiducci U, et al. Influence of injectable microparticle size on cardiac progenitor cell response. Journal of applied biomaterials & functional materials. 2018;16(4):241-51.
98. Zhang X, Pan Y, Li S, Xing L, Du S, Yuan G, et al. Doubly crosslinked biodegradable hydrogels based on gellan gum and chitosan for drug delivery and wound dressing. International Journal of Biological Macromolecules. 2020;164:2204-14.
99. Intelligence M. Biopharmaceuticals Market - Growth, Trends, COVID-19 Impact, And Forecasts (2021 - 2026). Hyderabad, India; 2021.
100. PLC I. Pharmaprojects Pharma R&D Annual Review 2016. London, United Kingdom: Informa PLC; 2016

101. Pham PV. Chapter 19 - Medical Biotechnology: Techniques and Applications. In: Barh D, Azevedo V, editors. Omics Technologies and Bio-Engineering: Academic Press; 2018. p. 449-69.
102. Abdulrahman A, Ghanem A. Recent advances in chromatographic purification of plasmid DNA for gene therapy and DNA vaccines: A review. Anal Chim Acta. 2018;1025:41-57.
103. Coskun O. Separation techniques: Chromatography. North Clin Istanb. 2016;3(2):156-60.
104. Tüzmen N, Akdoğan F, Kalburcu T, Akgöl S, Denizli A. Development of the magnetic beads for dye ligand affinity chromatography and application to magnetically stabilized fluidized bed system. Process Biochemistry. 2010;45(4):556-62.
105. Hlady V, Buijs J, Jennissen PH. Methods for Studying Protein Adsorption. Methods in Enzimology. 309: Academic Press; 1999. p. 402-29.
106. Mesgari-Shadi A, Sarrafzadeh M-H, Divband B, Barar J, Omidi Y. Batch adsorption/desorption for purification of scFv antibodies using nanozeolite microspheres. Microporous and Mesoporous Materials. 2018;264:167-75.
107. Deshmukh NR, Lali AM. Adsorptive purification of pDNA on superporous rigid cross-linked cellulose matrix. J Chromatogr B Analyt Technol Biomed Life Sci. 2005;818(1):5-10.

Annex 2 - Specific Six-transmembrane Epithelial Antigen of the Prostate 1 Capture with Gellan Gum Microspheres: Design, Optimization and Integration

Batista-Silva JP[1], Gomes D[1,2,3], Barroca-Ferreira J[1,2,3], Sousa A[1], Passarinha LA[1,2,3,4*]

[1]CICS-UBI – Health Sciences Research Centre, University of Beira Interior, 6201-506 Covilhã, Portugal

[2]Associate Laboratory i4HB - Institute for Health and Bioeconomy, NOVA School of Science and Technology, Universidade NOVA de Lisboa, 2829-516 Caparica, Portugal

[3]UCIBIO – Applied Molecular Biosciences Unit, Department of Chemistry, NOVA School of Science and Technology, Universidade NOVA de Lisboa, 2829-516 Caparica, Portugal

[4]Laboratório de Fármaco-Toxicologia - UBIMedical, University of Beira Interior, 6201-284 Covilhã, Portugal

*Address correspondent to this author at UCIBIO – Applied Molecular Biosciences Unit, Department of Chemistry, NOVA School of Science and Technology, Universidade NOVA de Lisboa, 2829-516 Caparica, Portugal.

Tel.: +351 275 329 069, Fax: +351 275 329 099, E-mail: lpassarinha@fcsaude.ubi.pt.

Abstract

The present work demonstrates the potential of calcium- and nickel-crosslinked gellan gum microspheres to capture the Six-Transmembrane Epithelial Antigen of the Prostate 1 (STEAP1) directly from complex *Komagataella pastoris* mini-bioreactor lysates in a simple batch method. Calcium-crosslinked microspheres were applied in an ionic exchange strategy, by manipulation of pH and ionic strength, whereas nickel-crosslinked microspheres were applied in an affinity strategy, mirroring a standard immobilized metal affinity chromatography. Both batch methods were optimized in regard to detergent solubilization, lysate concentrations, microsphere ratios and elution profiles. The most promising results were obtained for the ionic strategy, being able to completely bind STEAP1 in lysate samples at pH 6.2 in 10 mM MES buffer. The target protein was eluted in a complexed state at pH 11 with 500 mM NaCl in 10 mM Tris buffer, in a single step with minimal losses. Coupling the batch clarified sample with a Co-immunoprecipitation polishing step yields a sample of monomeric STEAP1 with a high degree of purity. Herein and for the first time, we demonstrate the potential of a gellan batch method to function as a clarification and primary capture method towards STEAP1, a membrane protein, simplifying and reducing the costs of standard purification workflows.

Keywords: STEAP1; Gellan Gum microspheres; Batch method; Capture; Co-immunoprecipitation

1. Introduction

Prostate cancer (PCa) is the second most frequently occurring cancer in males worldwide. According to Globocan, PCa is predicted to rise and become the most prevalent malignancy in males in 2040 with upwards of 2.4 million new cases per year (Sung et al., 2021). Indeed, PCa is diagnosed through the levels of prostate-specific antigen (PSA). However, PSA often fails to distinguish between PCa and benign prostatic hyperplasia or prostatitis, giving rise to false positives (I. M. Gomes, Arinto, et al., 2014; Hubert et al., 1999). Current treatment options, such as, prostatectomy, androgen ablation, radiation and chemotherapy seem to work for early stage PCa. Nevertheless, when PCa progresses to an androgen-independent metastatic phase or in the case of biochemical recurrence, these treatments become largely ineffective and low overall survivability is observed, making new approaches an imperative necessity (W. J. Chen et al., 2021; Ihlaseh-Catalano et al., 2013).

The Six-Transmembrane Epithelial Antigen of the Prostate 1 (STEAP1), first discovered in 1999 (Hubert et al., 1999), is a membrane protein overexpressed in PCa, while being mostly absent from other tissues or vital organs (I. M. Gomes et al., 2012; Hubert et al., 1999). Due to the secondary structure of STEAP1 and localization at the cell surface in tight- and gap-junctions it has been suggested to function as a transmembrane channel, transporting ions and small molecules, while also playing a role in cell adhesion and intercellular communication (W. J. Chen et al., 2021; Esmaeili et al., 2018; I. M. Gomes et al., 2012; Yamamoto et al., 2013). Further, when associated in heterotrimers with other STEAP family members, it seems to have metaloredutase functions, being involved in the reduction and uptake of iron and copper (Kim et al., 2016; Ohgami et al., 2006; Oosterheert & Gros, 2020). Moreover, STEAP1 has been linked with oxidative stress responses and elevated levels of reactive oxygen species, which in turn, activate redox-sensitive and pro-invasive genes (Grunewald et al., 2012). Also, STEAP1 overexpression has been suggested to be a driving force for tumor initiation and progression (I. M. Gomes, Arinto, et al., 2014). Overall, STEAP1 seems to enhance tumor proliferation and aggressiveness, making it a potential PCa biomarker and therapeutic target. Indeed, STEAP1 has been appointed as a tumor-associated antigen that can function as a target for immunotherapy. In fact, [^{89}Zr]Zr-DFO-MSTP2109A anti-STEAP1 antibody proved to be well tolerated and adequate for positron emission tomography bioimaging in PCa, being able to track changes in STEAP1 expression, and consequently, tracking the progression of PCa (Carrasquillo et al., 2019; Doran et al., 2014; O'Donoghue et al., 2019). Further, the conjugation of anti-STEAP1 antibodies with monomethyl auristatin E, a potent antimitotic agent, has shown potential in reducing tumor volume and delaying castration-resistant PCa (Boswell et

al., 2011; Danila et al., 2019; Williams et al., 2016). Another emerging strategy is the priming of cytotoxic T lymphocytes with STEAP1-derived epitopes for enhanced immune response. This approach has been associated with higher T cell infiltration in the tumor microenvironment (Krupa et al., 2011), reduced metastases (Schober et al., 2020) and tumor inhibition (X. Chen et al., 2019). Although promising, the development of immunotherapies is in its early days, and the efficacy is modest, being only a matter of time until the immunosuppressive nature of the tumor microenvironment rejects these therapeutics. It has also been shown that STEAP1 directly contributes to this immunosuppression (Zhao et al., 2021). Furthermore, although a STEAP1 structure has been deposited in the Protein Data Bank (PDB; https://www.rcsb.org/; Accessed in 28/09/2022) with the accession code 6Y9B (Oosterheert & Gros, 2020), it is incomplete, lacking both N- and C-terminals. Indeed, several sites have been predicted in both these domains for post translational modifications (PTM) (I. M. Gomes, Santos, et al., 2014). PTMs have also been proposed as one of the major differences between non-neoplastic PNT1A and neoplastic LNCaP cells, the latter being far more stable (I. M. Gomes, Santos, et al., 2014). Thus, a complete crystallized STEAP1 structure is mandatory, both for *in silico* modeling, as well as to potentially increase the effectiveness of current immunotherapy approaches through better structural understanding. However, current purification approaches are scarce and seem to be mostly based on sequential chromatographic steps of immobilized metal affinity chromatography (IMAC) and size exclusion chromatography (SEC) (Kim et al., 2016; Oosterheert & Gros, 2020). This purification workflow has shown promise in the crystallization of other membrane proteins (Löw et al., 2013). For instance, stable crystals were obtained from lysine-specific permease (Nji et al., 2014) and CdsD (Merilaïnen & Wierenga, 2014) extracts purified by IMAC and SEC in preliminary X-ray diffraction studies. Nonetheless, in the case of STEAP1, this approach appears to not be yielding enough protein concentration for crystallization studies, prompting the development of new isolation bioprocesses.

Gellan Gum (GG) is a natural linear anionic exopolysaccharide secreted by *Sphingomonas paucimobilis,* which consists of four repeating carbohydrates, including two β-D-glucoses, one α-L-rhamnose, and one β-D-glucuronic acid (Thangavelu Muthukumar, 2019; Zia et al., 2018). Due to its properties of biocompatibility, biodegradability, hydrophilicity, mucoadhesive features and good gelling capacity, GG has found remarkable success in the fields of food (Danalache et al., 2016), tissue engineering (Vieira et al., 2019), bioremediation (Park et al., 2021), biosynthesis (Lyu et al., 2019) and drug delivery (Villarreal-Otalvaro & Coburn, 2021). Indeed, GG-based materials have been shown to promote strong adsorption of small drug molecules (Racovita et al., 2016). Recently, our research group demonstrated that GG microspheres

can efficiently capture soluble catechol-O-methyltransferase (COMT) (D. Gomes, Gonçalves, et al., 2021) and plasmid DNA (D. Gomes, Costa, et al., 2021). Current microsphere-based methods being developed for protein capture are mostly based on magnetic microspheres, which quickly enhance complexity and cost of bioprocesses (Koubková et al., 2014; Lei et al., 2021, 2022; Zhou et al., 2020). Contrarily, GG microspheres are cost-effective and production methods are easier to scale up (Mahajan & Gattani, 2009). Further and until now, protein capture mediated through microparticles seems to be solely restricted to soluble proteins. Certainly, the difficulties associated with membrane protein purification, such as loss of stability and natural conformation, act as a deterrent for new capture procedures (Lin & Guidotti, 2009). In fact, out of 195858 structures deposited in PDB, only 10229 correspond to membrane proteins (Accessed on 28/09/2022). Nonetheless, membrane proteins play a pivotal role in biological processes and emerging capture and purification strategies should be explored towards structural determination.

Considering the necessity for novel bioprocesses and the efficacy previously demonstrated by GG microspheres in the capture of other biomolecules, the main purpose of the present work was to explore the potential of GG microspheres to capture recombinant human STEAP1, a highly relevant membrane protein from *Komagataella pastoris* lysates, through a simple batch method. To achieve this, GG microspheres were reinforced with calcium and nickel ions, and two different approaches were studied. For calcium-crosslinked GG an ionic exchange strategy was conducted by the manipulation of pH and ionic strength. For nickel-crosslinked GG an affinity approach was performed, mirroring IMAC.

2. Experimental

2.1 Materials

Ultrapure reagent-grade water was obtained from a Milli-Q system from Millipore/Waters. Gellan Gum (Gelzan™, Gelrite®), glass beads, lysozyme, deoxyribonuclease I (DNase), bromophenol blue, MES hydrate and MES sodium salt were acquired from Sigma-Aldrich Co. (St. Louis, MO, USA). Tris-base, tween-20, glycine, imidazole, sodium chloride (NaCl), nickel chloride hexahydrate ($NiCl_2.6H_2O$) and methanol were purchased from ThermoFischer Scientific (Waltham, MA, USA). Calcium Chloride dihydrate ($CaCl_2.2H_2O$) and sodium dodecyl sulfate (SDS) were obtained from PanReac Applichem (Darmstadt, Germany). β-mercaptoethanol and *N*,*N*,*N′*,*N′*-Tetramethylethylenediamine (TEMED) were acquired from Merck (Darmstadt, Germany). Bis-Acrylamide/Acrylamide 40% and NZYColour Protein Marker II were obtained from GRiSP Research Solutions (Oporto, Portugal) and NZYTech (Lisbon, Portugal), respectively. All other reagents and supplies were of analytical grade.

2.2 Methods

2.2.1 Gellan microspheres production

GG microspheres were produced through a water-in-oil (W/O) emulsion method, previously optimized by our research group through a design of experiments approach (Coelho et al., 2019). Briefly, we dissolved a 1.41% GG solution at 90 ◦C and 300 rpm for 15 min. Then, the GG solution was extruded drop by drop from a syringe with a 21G needle attached to a syringe pump (Harvard Apparatus, UK). The flow rate was set to 75 μL/min and the solution was dripped from a height of approximately 20 cm into 100% vegetable cooking oil previously heated to 100 ◦C under strong agitation. Next, the microspheres were reinforced with either Ca^{2+} or Ni^{2+}, by the addition of a 200 mM crosslinker solution to the emulsions at 750 rpm and room temperature during 30 min. Subsequently, excess oil was removed with 70% ethanol in a vacuum filtration system with 11 μm pore size filter paper (VWR, USA). Finally, GG microspheres were dried with water and stored in 10 mM MES buffer pH 6.2, at 4 ◦C, until they were used in capture trials.

2.2.2 Gellan microspheres characterization

2.2.2.1 Semi-optical microscopy

First, the average diameter of GG microspheres was assessed through semi-optical microscopy. So, microspheres were seated into microscope slides and visualized at 10x magnification. Six different images (n = 6) with a total of 46 measurements were obtained and the mean diameter was assessed.

2.2.2.2 Scanning electron microscopy (SEM)

Surface morphology of GG microspheres was evaluated through SEM, using a Hitachi S-3400 N microscope (Tokyo, Japan). The microspheres were distributed onto an aluminum support with a carbon base and frozen at -20 ◦C. Then, several representative images were taken using different magnifications, with a backscattered electron (BSE) 3D detector.

2.2.2.3 Elemental Analysis and Chemical Composition

To shed light on the elemental composition of produced microspheres, and confirm the incorporation of calcium, energy dispersive X-ray spectroscopy (EDX) was conducted. Still frozen, post SEM snapshot acquisitions, microspheres were analyzed via a QUANTAX 400 detector (Bruker, USA).

2.2.2.4 Fourier-transformed Infrared Spectroscopy (FTIR)

FTIR was utilized to gauge the appropriate formation of GG microspheres and to ensure divalent ion crosslinking. For this, samples were lyophilized, and spectra were acquired using a FTIR spectrophotometer (Nicolet iS10, ThermoFischer Scientific) for both GG powder and GG microspheres. The equipment was managed in the OMNIC Spectra software (ThermoFischer Scientific), and spectra were collected operating in ATR mode with an average of 120 scans on wavenumbers ranging from 400-4000 cm^{-1}, at a resolution of 32 cm^{-1}.

2.2.3 *Mini-bioreactor production and recovery of STEAP1*

The production and lysis of recombinant STEAP1 was performed as described by Duarte and coworkers (Duarte et al., 2021). Briefly, *Komagataella pastoris* X-33 Mut$^+$ were selected on yeast peptone dextrose (YPD) plates, at 30 ◦C. Then, a single colony was chosen and transferred to shaker flasks with 100 mL of Buffered minimal glycerol medium (BMGH) and grown overnight at 30◦C and 250 rpm until OD_{600nm} reached a value between 5-6. Then, an appropriate volume was collected so that the initial fermentation OD_{600nm} was equivalent to 0.5 and was deposited into 750 mL vessels from a mini bioreactors platform with 250 mL of basal salt medium (BSM) supplemented with Zeocin™ and a trace metal solution (SMT). The STEAP1 biosynthesis was divided into 3 main stages. First, a standard batch occurred until depletion of glycerol, detected by a sharp increase in dissolved oxygen. After, a glycerol fed-batch phase was carried out for 2h, in order to improve biomass levels, followed by a 1h transition phase where methanol was introduced to the feed to prepare the culture for a new carbon source. The third stage consists of a methanol feed strategy inducing the AOX promoter in the cells and stimulating the expression of His-tagged recombinant human STEAP1 (rhSTEAP1). Finally, the cells were retrieved by centrifugation for 10 min at 1500g and 4◦C.

To recover STEAP1, *K. Pastoris* cells were resuspended in lysis buffer (50 mM Tris, 150 mM NaCl, pH 7.8) supplemented with a protease inhibitor cocktail (Hoffmann-La Roche, Basel, Switzerland). Lysozyme (1 mg/mL) was added to the mix at room temperature for 15 min. After enzymatic digestion, the mixture was transferred to a falcon with glass beads in a ratio of 1:2:2, respectively, 1 g biomass, 2 mL of lysis buffer and 2 g of beads. Subsequently, mechanical lysis was executed through seven vortex cycles, interposed by 1 min intervals on ice. Next, the cell fragments and glass beads were separated by a 5 min 500g centrifugation at 4◦C. The pellet was resuspended in lysis buffer supplemented with DNase (1 mg/mL) and centrifuged at 16000g for 30 min at 4◦C. The supernatant was discarded, and the pellet was resuspended in the appropriate binding buffer for the batch method capture step. The total protein content in the lysates was quantified by Pierce BCA Protein Assay Kit (ThermoFischer Scientific) following manufacturer's instructions.

2.2.4 Batch method for the STEAP1 capture

The employed batch method was adapted from the batch described by Gomes and coworkers for the capture of COMT (D. Gomes, Gonçalves, et al., 2021). First, GG microspheres were equilibrated with an appropriate buffer for the capture step. Then,

the batch consisted in three main stages: Binding, Washing and Elution. The binding or capture step was initiated by the addition of the lysate in an appropriate dilution to the microspheres. This step was carried out for a total of 4h, at 4◦C under gentle tube agitation. This was followed by a centrifugation at 500g for 8 min and recovery of the supernatant. The washing and elution steps follow the same profile with adequate buffers during 1h. The batch was applied to GG microspheres crosslinked with calcium or nickel ions. For calcium, an ionic exchange strategy was chosen, by manipulation of pH, ranging from 6.2 to 11, and ionic strength, by manipulation of NaCl concentrations ranging from 0 to 500 mM, in order to recover STEAP1. For nickel, an affinity method similar to Immobilized metal affinity chromatography was used, where STEAP1 was bound to the microspheres through its His-Tag and eluted by varying imidazole concentrations, ranging from 5 to 500 mM in total concentration. The recovered fractions were concentrated and desalted with Vivaspin concentrators (10000 MWCO) and stored at 4◦C until further purity or immunoreactivity analysis.

2.2.5 Co-Immunoprecipitation

The clarified sample from the batch method was coupled with a final polishing Co-Immunoprecipitation (Co-IP) step. Co-IP was performed following manufacturer's protocol for Protein A/G PLUS-Agarose Immunoprecipitation Reagent (sc-2003, Santa Cruz Biotechnology, Dallas, TX, USA) with slight modifications. Succinctly, STEAP1 clarified samples were incubated for 1 h at 4◦C with anti-STEAP1 mouse monoclonal antibody (B-4, Santa Cruz Biotechnology, Dallas, TX, USA), followed by overnight incubation with agarose beads with constant stirring. Conjugated complexes were recuperated by centrifugation at 1000g for 5 min at 4◦C. Supernatant was discarded, the complexes were washed with PBS and then resuspended in electrophoresis loading buffer (refer to section 2.2.6). The agarose beads were separated from the antibody-STEAP1 complexes by the combinatory effect of sample boiling at 100◦C and 5% (v/v) β-mercaptoethanol.

2.2.6 SDS-PAGE and Western Blot

Reducing SDS-polyacrylamide gel electrophoresis (SDS-PAGE) was performed according to the Laemmli method (Laemmli, 1970). In essence, samples from the batch method were boiled for 5 min at 100◦C and resolved in two 12.5% SDS-PAGE gels at 120 V. Then, one gel was stained by Coomassie blue solution, while the other was transferred into a PVDF membrane (GE Healthcare,Wauwatosa, WI, USA) at 750 mA for 90 min at

4 ◦C. The membranes were blocked in 5% non-fat milk and incubated overnight with anti-STEAP1 mouse monoclonal antibody 1:300. Afterwards, following a 2 h incubation with goat anti-mouse IgG-HRP 1:5000 (sc-2005, Santa Cruz Biotechnology, Dallas, TX, USA), STEAP1 immunoreactivity was analyzed with ChemiDoc™ MP Imaging System after incubation with ECL substrate (Bio-Rad, Hercules, CA, USA).

3.Results

3.1 *Characterization of gellan gum microspheres*

GG microspheres produced through W/O emulsion were crosslinked with calcium and nickel ions. Calcium was chosen as it is the most widely used crosslinker for GG microspheres by researchers, with proven efficacy in drug delivery (Abbas & Marihal, 2014), immobilization of cells and enzymes (Fan et al., 2017; Lyu et al., 2019) and degradation of pollutants (Park et al., 2021). Nickel was selected since our research group had previously demonstrated this ion yielded the best capture and purification results for COMT, through a similar GG batch method (D. Gomes, Gonçalves, et al., 2021). Indeed, because nickel-crosslinked GG microspheres had already been described elsewhere, they were excluded from further characterization. Calcium-crosslinked GG microspheres were characterized in regard to size, morphology, and elemental composition, through semi-optical microscopy, SEM, EDX and FTIR.

The mean diameter for calcium-crosslinked GG microspheres was attained through the average of six (n = 6) snapshots from semi-optical microscopy. The obtained

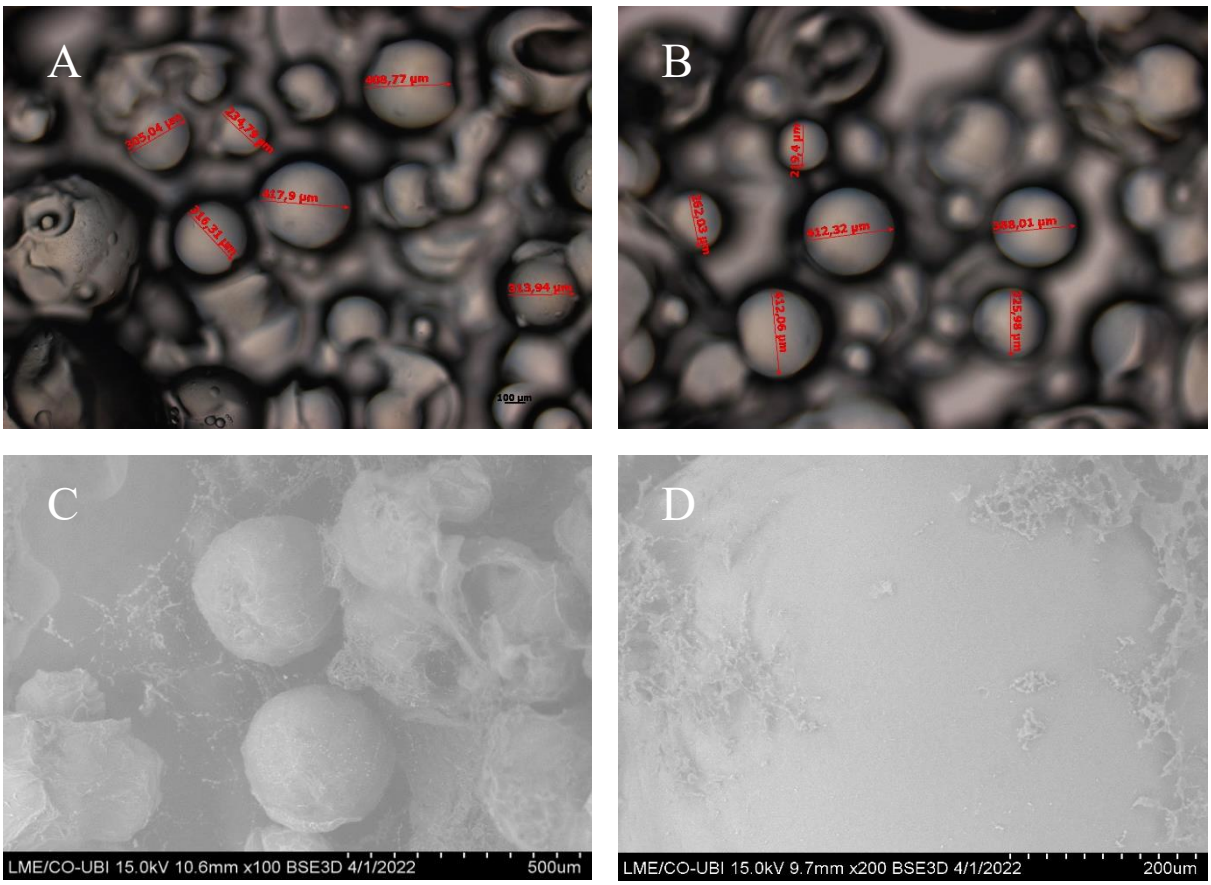

Figure 1. Semi-optical snapshots of calcium-crosslinked GG microspheres (A, B) and SEM images of calcium-crosslinked GG microspheres at x100 magnification (C) and x200 magnification (D).

mean diameter was of 330.37 ± 11.38 μm. Nickel-crosslinked GG microspheres had been previously described with a mean diameter of 239.06 ± 5.43 μm (D. Gomes, Gonçalves, et al., 2021). Representative snapshots can be seen in (**Fig. 1**). Further, the morphology and geometry of calcium-crosslinked microspheres was assessed through SEM. The microspheres present a consistent and uniform structure with spherical shape. At first glance, it appears that some rugosity is present, however examining the surface at x200 magnification, it becomes clear that the surface is smooth with no apparent pores, cavities or cracks (**Fig. 1D**). This result is opposite to what has been observed for GG microspheres crosslinked with magnesium, nickel and copper, where clear rugosity and cavities can be seen in the surface of the microspheres (D. Gomes, Costa, et al., 2021; D. Gomes, Gonçalves, et al., 2021). Following SEM, microspheres were analyzed by EDX to unveil the main elemental composition. A summary of the results can be found in **Table 1**. As previously mentioned, GG is mainly comprised of carbohydrates, which validates that the major chemical elements in the microspheres are carbon and oxygen. Further, calcium was detected at an appreciable level in calcium-crosslinked GG microspheres, confirming appropriate crosslinking. When compared to nickel-crosslinked GG microspheres, the normalized ion percentage levels seem to differ nearly two-fold. Indeed, when comparing copper-, magnesium-, nickel- and calcium-crosslinked microspheres by crosslinker percentage, it seems that transition metals are incorporated in higher degrees than alkaline earth metals (D. Gomes, Costa, et al., 2021; D. Gomes, Gonçalves, et al., 2021). This stronger crosslinker concentration can induce the formation of a tighter mesh network, resulting in more compact microspheres, which can justify why nickel-crosslinked microspheres are smaller than calcium-crosslinked microspheres (Babu et al., 2010).

Table 1. Elemental Composition of GG microspheres through EDX.

Element	Calcium-crosslinked GG microspheres		Nickel-crosslinked GG microspheres	
	C norm. [wt%]	C atom. [at%]	C norm. [wt%]	C atom. [at%]
Carbon	31.87	38.72	39.19	47.13
Oxygen	66.54	60.70	57.73	52.12
Calcium	1.59	0.58	-	-
Nickel	-	-	3.08	0.76
Total	100.0	100.0	100.0	100.0
Ref.	-		(D. Gomes, Gonçalves, et al., 2021)	

Then, FTIR analysis was performed to evaluate the chemical integrity of GG after microsphere assembly, as well as to detect the chemical interactions between GG and calcium. The recorded FTIR spectra for both GG powder and calcium-crosslinked GG microspheres can be seen in **Fig. 2**. The spectrum of GG powder showed characteristic peaks at 3333 cm^{-1}, due to the stretching of hydroxyl groups (-OH) from glucopyranose rings. The peak at 2912 cm^{-1} is assigned to -CH vibrations (Agnihotri & Aminabhavi, 2005; Dhanka et al., 2018). Further peaks at 1605 cm^{-1} and 1400 cm^{-1}, correspond to the presence of carboxylate anions (COO^-). The peak at 1026 cm^{-1} is linked to hydroxylic C-O stretching (Agnihotri & Aminabhavi, 2005; Dhanka et al., 2018). The spectrum for calcium-crosslinked GG microspheres displays similar peaks, although with slight variations in absorbance. Indeed, the rise of a peak at 1743 cm^{-1} and the disappearance of the peak at 1400 cm^{-1} suggests an interaction between the carboxyl groups from GG with calcium ions. Further, the quenching of the peaks at 3333cm^{-1} and 1026 cm^{-1} might suggest that calcium could also bind in the glucopyranose rings of glucose and to the negatively charged components of glucuronic acid, respectively. It appears that all subunits of GG are involved in the coordination of calcium binding and this change in FTIR spectra corroborates EDX results, confirming calcium crosslinking.

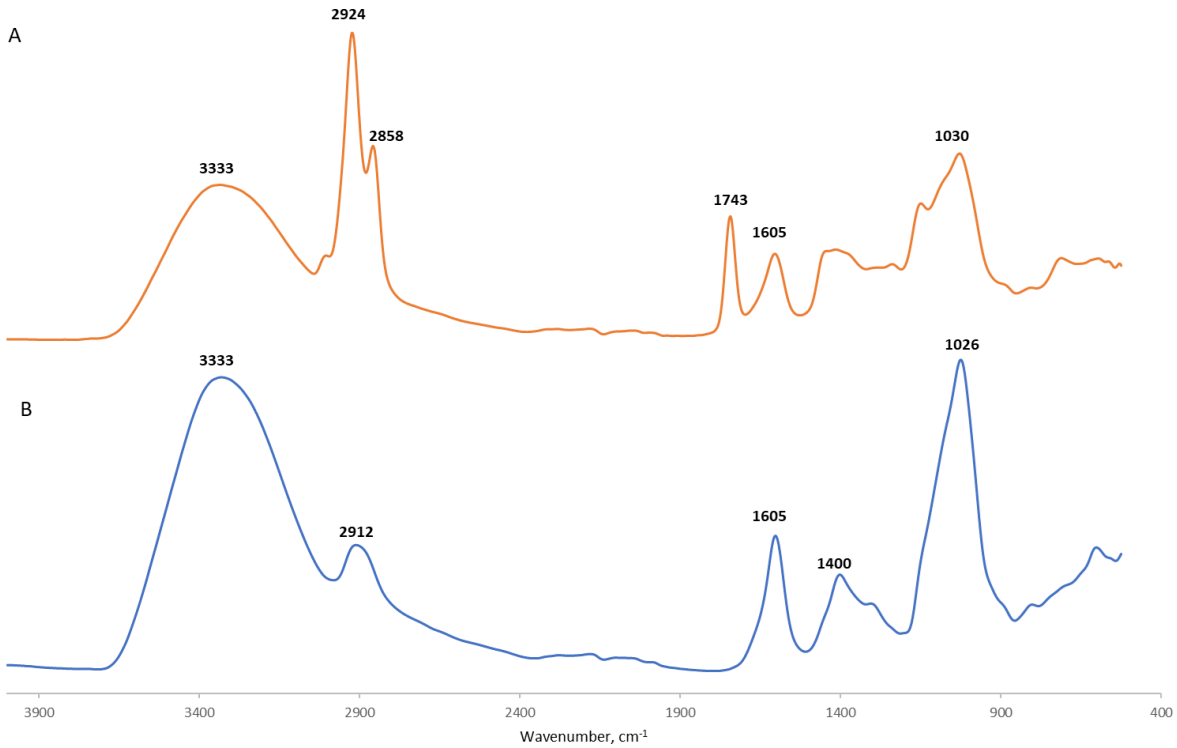

Figure 2. FTIR Spectra (Absorbance vs Wavenumber) of calcium-crosslinked GG microspheres (A) and GG powder (B).

3.2 *Optimization of the batch method for the capture of STEAP1*

As previously mentioned, the batch method employed follows a simple sequence of binding, washing and elution steps. It was intended to take advantage of the high predicted STEAP1 isoelectric point of ~9.2 (Compute pI – Expasy; https://web.expasy.org/compute_pi/) to separate it from the remainder *K. pastoris* proteome with an average isoelectric point of 6.46 (Proteome-pI database; (Kozlowski, 2017)). Although *K. pastoris* X33 Mut$^+$ were used for STEAP1 production, instead of the listed *K. pastoris* strain GS115 in the Proteome-pI database, no significant changes were expected in isoelectric point since X33 is derived from GS115 (Blanchard et al., 2008). So, the explored initial strategy was ionic exchange, based solely on pH manipulation for both microspheres, where it was intended to bind STEAP1 to GG microspheres at pH 6.2 in 10 mM MES buffer, wash off most impurities at pH 8 in 10 mM Tris buffer and then start eluting STEAP1 at pH 9.2 or higher in 10 mM Tris buffer, either by charge neutralization or charge repulsion. However, as can be seen in **Fig. 3**, protein samples recuperated from the initial batch with both microsphere crosslinkers presented an elevated molecular weight of >245 kDa. Indeed, it appears that STEAP1 tended to form complexes with GG microspheres, and in turn, potentially aggregate. It had been previously reported that sample boiling prior to Western Blot for other transmembrane proteins resulted in similar large molecular weight complexes in immunoreactive assays (Tsuji, 2020). To evaluate this condition, batch samples were left at room temperature, whereas their equivalent counterparts were boiled at 100 ◦C for 5 min prior to detection, however no change was detected for either condition (data not shown). Therefore, a

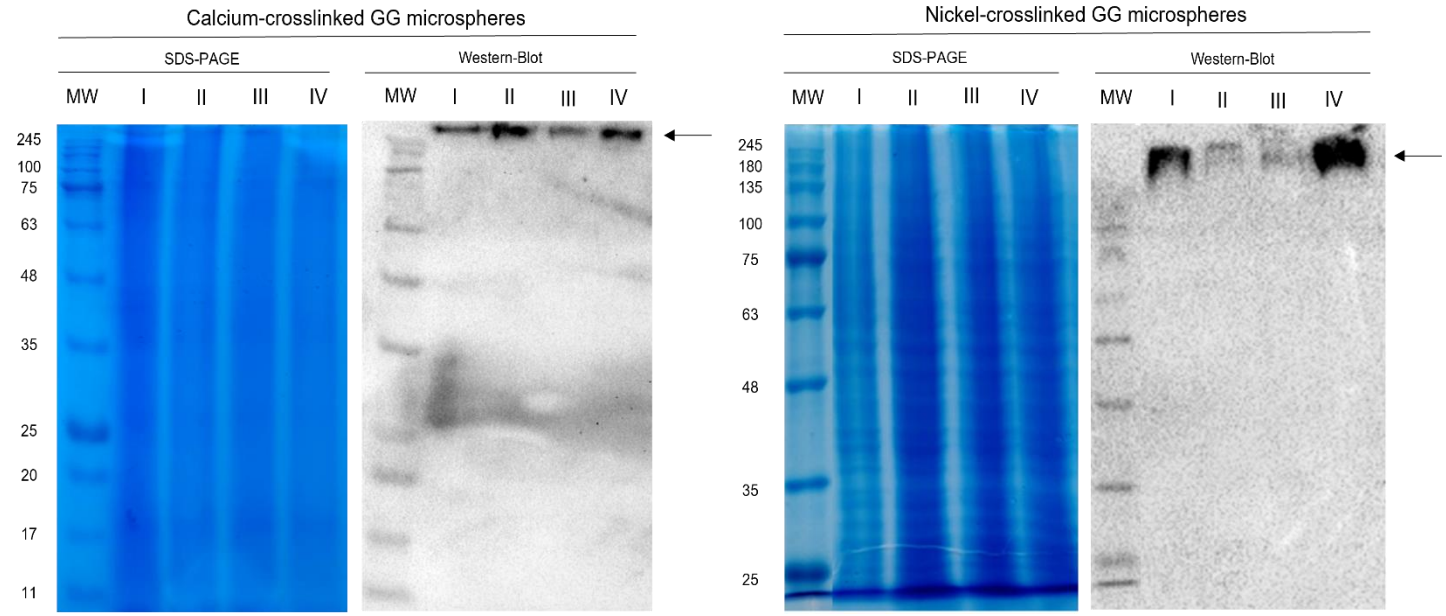

Figure 3. SDS-PAGE and Western-blot of the recovered supernatants from the initial batch for both calcium and nickel crosslinked microspheres (35 mL GG microspheres for both ions represented). MW – molecular weight; I – Sample that did not bind to GG microspheres at 10 mM MES pH 6.2; II – Washing step with 10 mM Tris pH 8; III – Elution step with 10 mM Tris pH 9.2; IV – Elution Step with 10 mM Tris pH 11; Arrows indicate STEAP1 complexes.

series of optimizations were conducted to improve protein stability and solubility, namely, detergent solubilization, initial lysate concentration screening and microspheres volume ratios.

First, and since solubilization of membrane proteins is of the utmost importance for proper stabilization and conformation outside the natural lipidic environment (Kalipatnapu & Chattopadhyay, 2005; Seddon et al., 2004), several mild nonionic detergents that our group had previously tested for STEAP1 at a 0.1% concentration (data not shown), were selected for solubilization assays. Following cell lysis and STEAP1 recovery procedure, resulting pellets were resuspended in 10 mM MES buffer at pH 6.2 with either 0.1% (v/v) of 5-Cyclohexyl-1-Pentyl-β-D-Maltoside (CYMAL-5), n-Decyl-β-D-Maltoside (DM), Nonidet P-40 (NP-40) or Genapol X-100 (GEN). In **Fig 4A**, it is observed that the Maltoside-based detergents were more effective in solubilizing STEAP1, with DM exhibiting the strongest band intensity. As for GEN and NP-40, very little difference can be observed from the control sample. In fact, it seems that GEN actually causes some degradation of STEAP1.

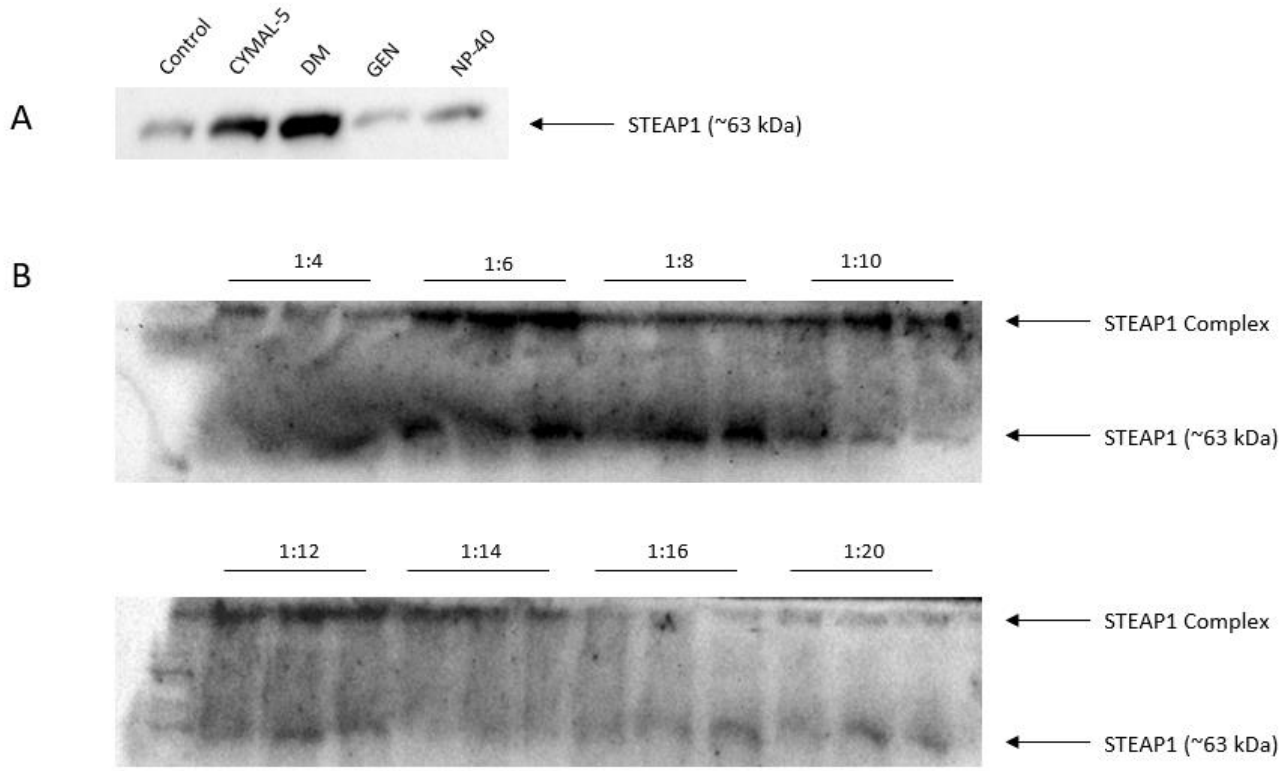

Figure 4. Western-blot of the detergent screening for solubilization of STEAP1 (control represents unsolubilized lysate samples) (A) and recovered supernatants from the Initial batch lysate dilution screening following a simple three step sequence per dilution: Binding – 10 mM MES pH 6.2; Washing – 10 mM Tris pH 8; Elution – 10 mM Tris pH 11 (B).

In the initial batch a lysate dilution of 1:4 was used, as previously described (D. Gomes, Gonçalves, et al., 2021). However, since this lysate dilution, and therefore total initial protein concentration, resulted in the formation of large molecular weight bands

exceeding 245 kDa, it was decided to assess if the total protein concentration was inducing aggregation events. So, a simplified batch, with only 3 steps consisting of binding (10 mM MES buffer at pH 6.2), washing (10 mM Tris pH 8) and elution (10 mM Tris pH 11) steps, was utilized to screen an array of initial lysate dilutions ranging from 1:4 to 1:20. Results are displayed in **Fig 4B**. Indeed, it seems that 1:4 dilution forms large molecular weight complexes and compromises analysis. Starting from 1:6 (total protein concentration of ~7 mg/mL) and forwards some migration of STEAP1 to approximately 63 kDa was observed. Further, the bands at the top of the membranes remain present even at the most diluted samples of 1:20 (~2.15 total protein in mg/mL). This might indicate that STEAP1 aggregation is not the main driving force for the formation of these high molecular weight complexes. Nevertheless, considering the information of both screenings, from this point forward all batches were performed with an initial lysate dilution of 1:6, since this dilution degree allows for the clarification of the highest amount of STEAP1 in each batch run. Also, 0.1% (v/v) DM was included in all buffers in order to solubilize and maintain STEAP1 stability throughout the batch runs. In fact, just applying these 2 optimized parameters in conjunction to the initial batch workflow with calcium-crosslinked GG microspheres, it was possible to bind the great majority of STEAP1 and start eluting it at pH 9.2, by charge neutralization (**Fig. 5**). Moreover, up until this point different microsphere volume ratios were tested. These were 20 mL and 35 mL of GG microspheres to 6 mL of buffer applied in each batch step. The 35 mL of GG microspheres exhibited better binding results of our membrane protein target and were selected for further analysis. The results from the ionic exchange strategy were very similar for nickel-crosslinked microspheres, in regards to elution profiles and protein content in each batch step (data not shown).

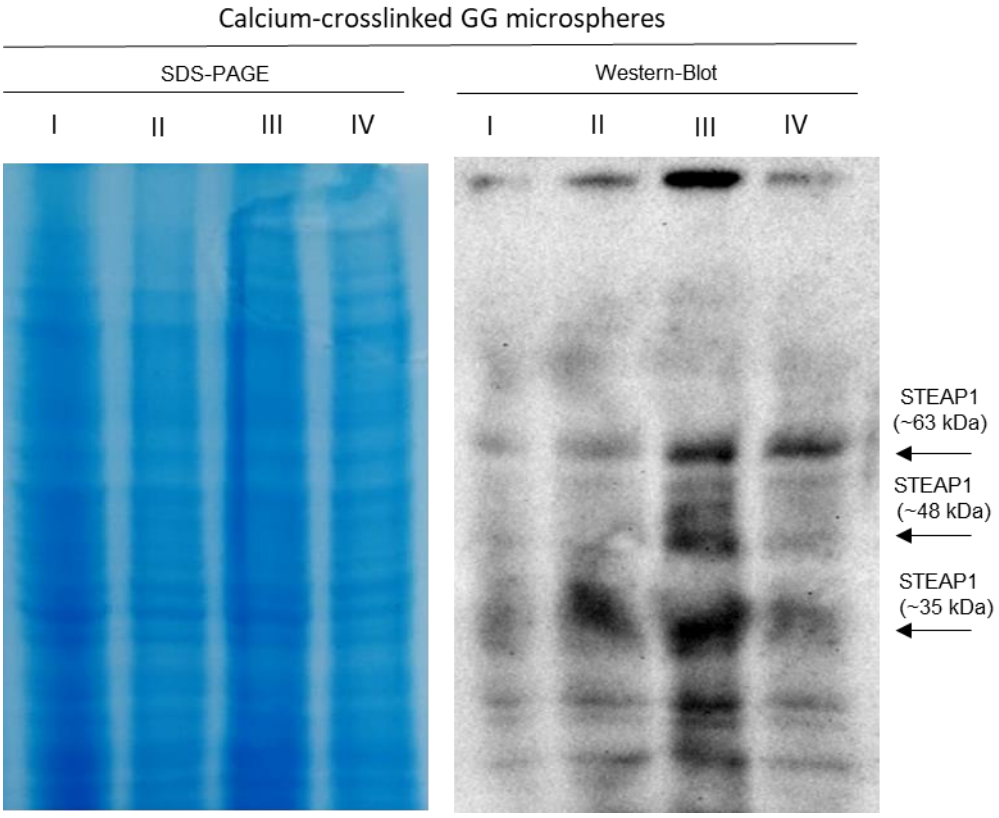

Figure 5. SDS-PAGE and Western-blot of the recovered supernatants from the optimized batch for calcium-crosslinked GG microspheres (35 mL GG microspheres); I – Sample that did not bind to GG microspheres at 10 mM MES pH 6.2; II – Washing step with 10 mM Tris pH 8; III – Elution step with 10 mM Tris pH 9.2; IV – Elution Step with 10 mM Tris pH 11.

3.3 Batch method for the capture of STEAP1

3.3.1 Affinity strategy for STEAP1 capture using nickel-crosslinked GG microspheres

Because the results from the ionic exchange strategy yielded equivalent results for both types of microspheres it would be redundant to develop the same approach for nickel- and calcium-crosslinked GG microspheres. Instead, nickel-crosslinked GG microspheres were used to capture STEAP1 through its 6xHis-Tag, simulating IMAC retention mechanisms, where elution would be prompted by increasing imidazole concentrations. Previous internal data had demonstrated that STEAP1 in a nickel IMAC column following an imidazole stepwise elution scheme (10 mM, 50 mM, 175 mM, 300 mM, 500 mM; elution profile adapted from (Pedro et al., 2018)) started eluting at 175 mM imidazole (data not shown). Therefore, in the present work it was decided to setup a batch roadmap with fixed pH at 9.2 to eliminate or reduce as much as possible any electrostatic interaction. The latter optimized batch through lysate dilution, DM solubilization and microsphere ratio tuning exhibited positive results, yet a large degree of complexation was still present. To tackle this issue, it was also added a moderate

amount of salt to the buffers, to promote a slight salting-in effect and promote STEAP1 stabilization. Salt stabilization had been previously demonstrated for Rhodopsin, a structurally similar transmembrane protein (Reyes-Alcaraz et al., 2011). The affinity batch was setup with a binding step consisting of 10 mM Tris at pH 9.2 with 150 mM NaCl and 5 mM imidazole and elution steps with the same amount of salt but with increasing concentrations of imidazole, corresponding to 175, 300 and 500 mM imidazole in 10 mM Tris pH 9.2. Following this gradient step mode, STEAP1 seemed to elute equally in all elution steps, suggesting that our target does in fact start eluting at 175 mM similar to IMAC. However, unlike IMAC, 175 mM imidazole was not enough to fully elute STEAP1 in a single step (data not shown). To address this elution profile, the batch was condensed to three steps, where binding would remain equal, followed by a washing step with 50 mM imidazole to remove any non-specific protein binding that may have occurred in the microspheres, and then a final elution step with 500 mM imidazole (the highest concentration from previous batch). Highlighted in **Fig. 6**, with the described conditions, most of STEAP1 was captured through an affinity approach. However, it seems that over half was eluted in the supposed washing step with 50 mM imidazole. This indicates that a 3.5 times lower imidazole concentration can elute STEAP1 in a GG batch method as opposed to the necessary 175 mM in IMAC.

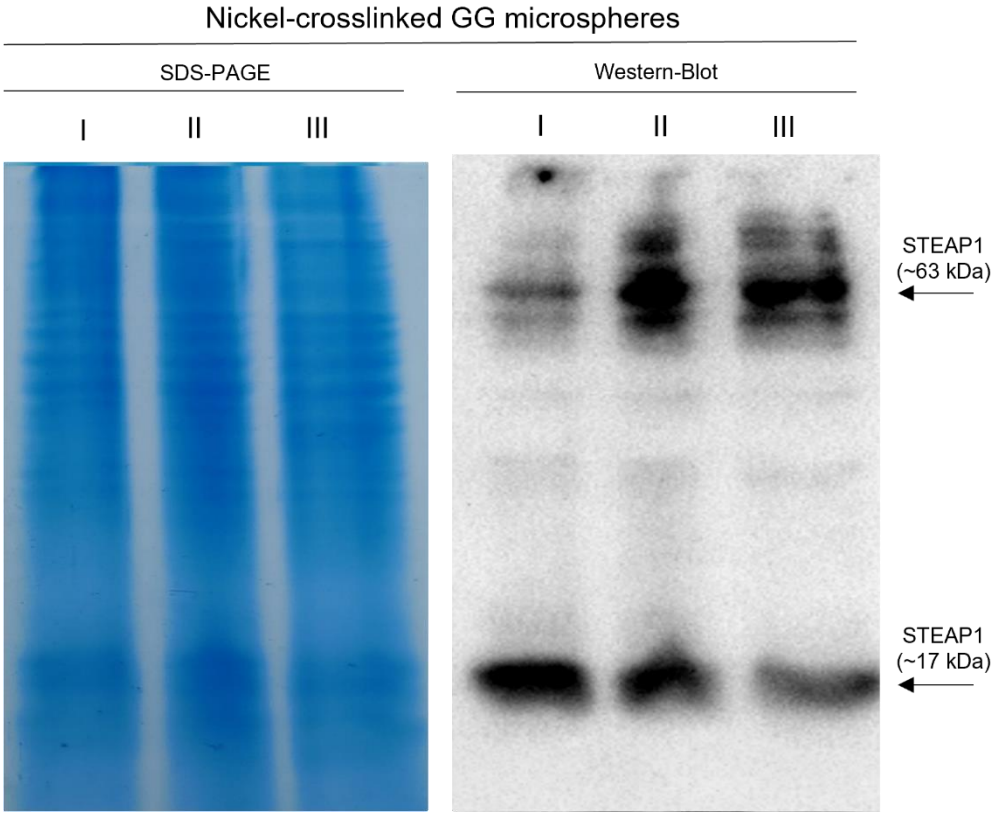

Figure 6. SDS-PAGE and Western-blot of the recovered supernatants from affinity batch with nickel-crosslinked GG microspheres; I – Sample that did not bind to GG microspheres at 10 mM Tris pH 9.2 with 150 mM NaCl and 5 mM imidazole; II – Washing step with 10 mM Tris pH 9.2 with 150 mM NaCl and 50 mM imidazole; III – Elution step with 10 mM Tris pH 9.2 with 150 mM NaCl and 500 mM imidazole.

Furthermore, a great deal of degradation (~17 kDa) was observed for the first time in all batch runs. Due to the degradation and the fact that it was not possible to recover the majority of STEAP1 in a single step, the samples recovered from nickel-crosslinked GG microspheres batches were excluded from further purification.

3.3.2 Ionic strategy for STEAP1 capture using calcium-crosslinked GG microspheres

Similar to the affinity strategy, for the ionic batch strategy using calcium-crosslinked GG microspheres, salt was introduced to attain the same salting-in effect. However, instead of a fixed concentration of 150 mM, this assay explored the increase of intra-step NaCl levels in order to streamline the batch method to mimic a standard ionic exchange chromatography. In the optimization batch, it was noticed that although STEAP1 eluted mostly at pH 9.2, there was still a fraction of STEAP1 only being eluted at pH 11 buffer base. To recover as much target protein as possible in a single step, a switch to a single elution step and the replacement of the previous elution step at pH 9.2 with an additional washing step were made, in order to enhance the removal of impurities. In this manner, the ionic exchange batch remained a four-step batch with the conditions underlined in **Fig. 7A**. In the binding step, practically all STEAP1 bound to calcium-crosslinked GG microspheres at pH 6.2 with no salt. Then, the minimal losses that were observed for the initial wash step at pH 8 with 100 mM NaCl, quickly turned into substantial losses by the increase to 200 mM NaCl at the same pH level. As intended, the bulk of STEAP1 was recovered in the final step by charge repulsion induced by the highest amount of salt. Although a clearer sample was obtained in the end of the four-step batch system, a significant loss was observed in line III. To tackle this issue, the batch was condensed into three steps by removing the washing step with 200 mM NaCl and by concentrating this sample at pH 11 with 500 mM NaCl. However, when swapping to the condensed batch mixed results were observed. As highlighted in **Fig. 7B,** while all of STEAP1 was retained during the binding step and remained bound during the washing step, target samples returned to a fully complexed state in the elution step, even with all optimizations previously described. Considering all the results thus far and GGs molecular weight of 500 kDa (Bacelar et al., 2016), we suspected that STEAP1 was forming complexes with the microspheres beyond simple ionic interactions. To assess the strength of this complexation, fully complexed samples were coupled with a Co-Immunoprecipitation polishing step. Indeed, it appears the antibody-STEAP1 interaction is stronger than GG-STEAP1, since post Co-IP STEAP1 was recovered in its monomeric form (**Fig. 8**). SDS-PAGE of Co-IP STEAP1 shows a high degree of purity, although a major unidentified protein can be seen between ~63 and ~75 kDa.

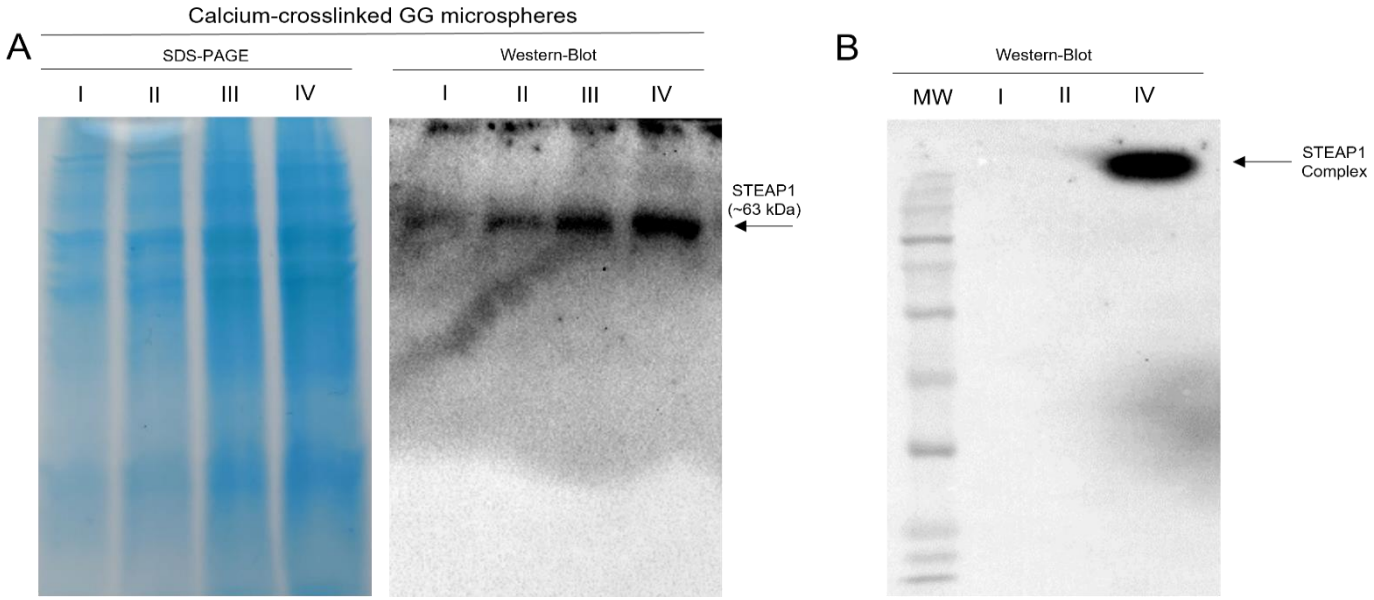

Figure 7. SDS-PAGE and Western-blot of the recovered supernatants from the ionic exchange batch for calcium-crosslinked GG microspheres for both a four-step batch (A) and Condensed batch (B) (35 mL GG microspheres); I – Sample that did not bind to GG microspheres at 10 mM MES pH 6.2; II – Wash step with 10 mM Tris pH 8 and 100 mM NaCl; III – Elution step with 10 mM Tris pH 8 and 200 mM NaCl; IV – Elution Step with 10 mM Tris pH 11 and 500 mM NaCl.

By analysis of the proteome from *Komagataella pastoris* X-33 reported by Huang and coworkers (Huang et al., 2011) and by taking into account proximity to the expected molecular weight and isoelectric point, we were able to identify Ferric and cupric reductase (FRE2) and Ferrioxamine B (SIT1) as possibilities for this unidentified protein. Summarizing the presented results, it appears that a simple GG batch can successfully act as a primary purification step. Even in the worst case scenario, where STEAP1 fully complexes with GG microspheres, a Co-IP polishing step can be applied to obtain a purified sample. Further, Co-IP seems to also be able to fix the aggregation issues derived from upstream stage (~63 kDa in lysate to ~35 kDa monomeric form).

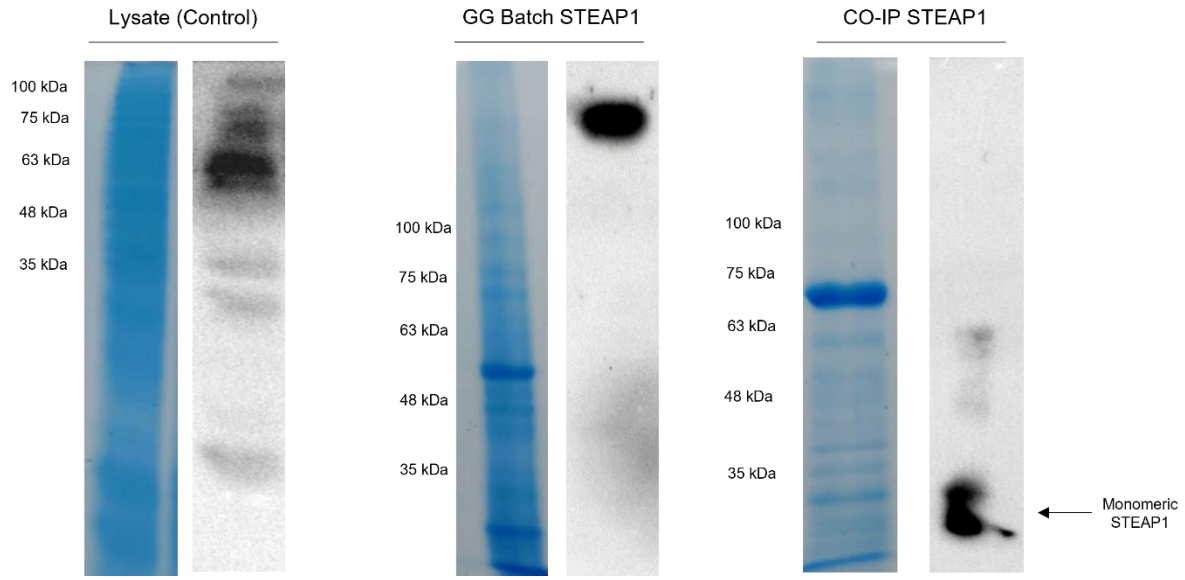

Figure 8. SDS-PAGE and Western-Blot of the entire purification workflow: the initial total protein content in *K.pastoris* lysate, the clarified sample from calcium-crosslinked GG batch and the purified co-immunoprecipitated STEAP1

4. Discussion

STEAP1 has been appointed as a putative biomarker and therapeutic agent in a plenitude of cancers, with higher expression levels in PCa. Unlike other STEAP family members (2-4), STEAP1 does not contain an N-terminal NADPH binding domain. Instead, it has a long tail that sits in the intracellular domain with undiscovered functions. Further, STEAP1 has been predicted to play a role in a slew of signaling pathways (Guo et al., 2020; Huo et al., 2020; Nakamura et al., 2019; Zhang et al., 2020) and we speculate this STEAP1 disposition could be related to signal transduction. As previously mentioned, it is imperative to uncover the full STEAP1 structure, in order to explore the role this protein plays in biological systems. For this, improvements to current bioprocesses are necessary. Earlier, our research group made strides in optimizing the production of recombinant human STEAP1 in a mini-bioreactor platform (Duarte et al., 2021). The produced recombinant protein fractions increased the proliferation of prostate cancer cell lines, indicating they acquire active confirmation (Duarte et al., 2021). Here, we tackled the downstream portion in an attempt to improve purification yields, resorting to a simple batch method with GG microspheres. Both calcium- and nickel-crosslinked GG microspheres were produced through a previously optimized W/O emulsion, resulting in average diameters of 330.37 ± 11.38 μm and 239.06 ± 5.43 μm, respectively. These values are lower than those reported for GG microspheres produced by ionotropic gelation (Babu et al., 2010; Narkar et al., 2010). Indeed, as the size of microspheres decreases it is expected an improvement in specific surface area, and consequently an improvement in adsorption capacity (Kawaguchi, 2000). However, no evident change was observed between calcium and nickel microspheres after the ionic optimization batch (data not shown). The initial batch strategy was based on a very simple ionic interaction. In the ionic approach, GG would always present a negative charge (pKa = 3.5; (Cassanelli et al., 2018)) and STEAP1 would bind at pH 6.2 with a positive charge, and be eluted at >pH 9.2, by electrostatic repulsion. However, in the initial batch only large molecular weight bands were observed in the immunoreactive assays. At first, it was suspected that STEAP1 might be getting stuck inside or in certain cavities in GG microspheres. However, calcium-crosslinked GG microspheres SEM images present a smooth surface with no apparent pores or cavities. Next, it was suspected that STEAP1 was forming large aggregates. To improve STEAP1 stability during the batch, several optimizations were initiated. First, a series of non-ionic detergents were applied in the solubilization of STEAP1. These detergents were selected mainly because they are non-denaturant and can ensure the biological function of membrane proteins, as opposed to ionic and zwitterionic detergents which are harsher and often lead do deactivation or

denaturation of membrane proteins (Kermani, 2021; Seddon et al., 2004). From the selected detergents, DM presented the best solubilization potential. Similar to most membrane proteins, STEAP1 is best solubilized by alkyl maltopyranosides. Indeed, approximately 50% of membrane proteins in the Membrane Proteins of Known 3D Structure database were solubilized by alkyl maltopyranoside detergents both in the purification and crystallization phases of structure determination (Stetsenko & Guskov, 2017). Thereafter, the influence of total protein content in the batch was assessed by screening an assortment of different dilutions from 1:4 to 1:20. Starting from a dilution of 1:6 (~7 mg/mL) and forwards, some migration was observed to ~63 kDa. This could suggest that aggregation was in fact a contributing factor, however even at dilutions of 1:20 (~2.15 mg/mL) the presence of large weight aggregates was constant throughout immunoreactive assays. When applying both DM and 1:6 dilution in the optimized batch (**Fig. 5**), it was possible to minimize the large molecular weight complexes. Furthermore, the remaining complexes were mainly localized at the elution step with pH 9.2, where the majority of STEAP1 eluted. When the SDS-PAGE of all assays is compared, it is clear that all lanes are very similar in protein composition. So, if hetero-aggregation was the cause, it would be expected that other proteins would interfere with antibody detection of STEAP1. Yet, the intensity of the complexes band seems to mimic the intensity to which STEAP1 is present in each batch step. In addition, the presence of small STEAP1 aggregates (~48 and ~63 kDa) is not considered a concern, since they have been previously associated with the recombinant production steps (Duarte et al., 2021). In fact, Kim and coworkers ventured as far as to call them the dimeric and trimeric STEAP1 (Kim et al., 2016). In order to further reduce the occurrence of complexation, the addition of salt was carried out to promote a small salting-in effect and stabilize STEAP1. In the four-step batch (**Fig. 7A**), only a very modest benefit was observed in the reduction of complexes. Later, when condensing to a three step batch to minimize STEAP1 losses, mixed results were observed. Indeed, STEAP1 was fully collected in the intended elution step without losses, but it came fully complexed. During the intra-step centrifugation steps and posterior supernatant collection, it was observed that some GG microspheres did not sediment completely and were recovered in the supernatant. Even with several optimization studies onto this capture method, it was not possible to identify a schema that could fully separate the GG microspheres from the target protein. So, we suspect that GG with 500 kDa was forming complexes with STEAP1 and increasing amounts of microspheres recovered would prompt higher rates of complexation. Indeed, these complexes seem to origin outside the scope of standard ionic interactions since electrostatic repulsion and 500 mM NaCl should have been more than enough to disrupt these interactions. STEAP1 has been previously predicted to act both as an ionic channel

and to modulate the concentration of small ions, calcium included (Barroca-Ferreira et al., 2018; I. M. Gomes et al., 2012). Perhaps STEAP1 functions as a calcium transmembrane channel and forms GG-STEAP1 complexes by the mediation of latent affinity towards the calcium crosslinker. Further, nickel cellular uptake has been shown to be calcium dependent, with some evidence suggesting that it crosses the plasma membrane through calcium channels (Muñoz & Costa, 2012), which might suggest why nickel-crosslinked GG microspheres suffered from the same complex formation. Nevertheless, the sample recovered from the condensed ionic strategy batch was coupled with a Co-IP polishing step, since this technique is highly specific and selective in the detection of physical protein interactions (Poetz et al., 2009). Results indicated that the formation of the antibody-STEAP1 immunoconjugates was stronger than the affinity between GG-STEAP1 complexes, as the latter complexes were disrupted and STEAP1 was recovered in its purified monomeric form. Further, our Co-IP results for recombinant human STEAP1 were very similar to those reported by an hydrophobic interaction chromatographic step coupled with Co-IP purification workflow, with lysates from LNCaP cells (Barroca-Ferreira et al., 2021). However, considering the inability to completely separate GG from STEAP1, the presence of glucose moieties in the GG backbone and the fact that reducing sugars are a known interference in the BCA protein quantification assay (Noyes et al., 2014), it was not possible to quantify the recovered samples. Furthermore, STEAP1 needs to form heterotrimeric ensembles with other STEAP members to attain metaloreductase activity (Oosterheert & Gros, 2020), making quantification via an enzymatic iron reduction approach inaccessible, since recombinant STEAP1 was used in the batch method. Indeed, new approaches that allow the quantification of the recovered samples should be addressed in future research.

In summary, we developed, for the first time, a simple batch method using GG microspheres that can be utilized for the capture and purification of membrane proteins. The ionic batch method is simple, fast, cost-effective and can be applied as a primary capture step for STEAP1. The complexation observed seems to be STEAP1-specific and the chemical nature of such strong complexes should be addressed in future research. Nevertheless, coupling a Co-IP polishing step to the batch method yields STEAP1 with a high degree of purity and completes the purification workflow. Further, since the average isoelectric point of membrane proteins seems to be between 8.5 to 9.0 (Tokmakov et al., 2021), it is safe to assume that this simple ionic GG batch method can be extended to the capture of other relevant membrane proteins with clinical interest.

Acknowledgements

The authors acknowledge the support from FEDER funds through the POCI-COMPETE 2020–Operational Programme Competitiveness and Internationalisation in Axis I–Strengthening Research, Technological Development and Innovation (Project POCI-01-0145-FEDER-007491), Jorge Barroca-Ferreira and Diana Gomes PhD Fellowships (SFRH/BD/130068/2017 and 2020.06792.BD, respectively). This work was also supported by the Health Sciences Research Centre CICS-UBI (UIDB/00709/2020 and UIDP/00709/2020), the Applied Molecular Biosciences Unit UCIBIO (UIDB/04378/2020 and UIDP/04378/2020) and the Associate Laboratory Institute for Health and Bioeconomy–i4HB (project LA/P/0140/2020) which are financed by National Funds from FCT/MCTES.

References

1. Sung, H. *et al.* Global Cancer Statistics 2020: GLOBOCAN Estimates of Incidence and Mortality Worldwide for 36 Cancers in 185 Countries. *CA. Cancer J. Clin.* **71**, 209–249 (2021).

2. Hubert, R. S. *et al.* STEAP: A prostate-specific cell-surface antigen highly expressed in human prostate tumors. *Proc. Natl. Acad. Sci. U. S. A.* **96**, 14523–14528 (1999).

3. Gomes, I. M., Arinto, P., Lopes, C., Santos, C. R. & Maia, C. J. STEAP1 is overexpressed in prostate cancer and prostatic intraepithelial neoplasia lesions, and it is positively associated with Gleason score. *Urol. Oncol. Semin. Orig. Investig.* **32**, 53.e23-53.e29 (2014).

4. Ihlaseh-Catalano, S. M. *et al.* STEAP1 protein overexpression is an independent marker for biochemical recurrence in prostate carcinoma. *Histopathology* **63**, 678–685 (2013).

5. Chen, W. J. *et al.* Regulatory Roles of Six-Transmembrane Epithelial Antigen of the Prostate Family Members in the Occurrence and Development of Malignant Tumors. *Front. Cell Dev. Biol.* **9**, 1–10 (2021).

6. Gomes, I. M., Maia, C. J. & Santos, C. R. STEAP proteins: From structure to applications in cancer therapy. *Mol. Cancer Res.* **10**, 573–587 (2012).

7. Yamamoto, T. *et al.* Six-transmembrane epithelial antigen of the prostate-1 plays a role for in vivo tumor growth via intercellular communication. *Exp. Cell Res.* **319**, 2617–2626 (2013).

8. Esmaeili, S.-A., Nejatollahi, F. & Sahebkar, A. Inhibition of Intercellular Communication between Prostate Cancer Cells by A Specific Anti-STEAP-1 Single Chain Antibody. *Anti-Cancer Agents in Medicinal Chemistry* vol. 18 1674–1679 (2018).

9. Kim, K. *et al.* Six-Transmembrane Epithelial Antigen of Prostate 1 (STEAP1) Has a Single b Heme and Is Capable of Reducing Metal Ion Complexes and Oxygen. *Biochemistry* **55**, 6673–6684 (2016).

10. Oosterheert, W. & Gros, P. Cryo-electron microscopy structure and potential enzymatic function of human six-transmembrane epithelial antigen of the prostate 1 (STEAP1). *J. Biol. Chem.* **295**, 9502–9512 (2020).

11. Ohgami, R. S., Campagna, D. R., McDonald, A. & Fleming, M. D. The Steap proteins are metalloreductases. *Blood* **108**, 1388–1394 (2006).

12. Grunewald, T. G. P. *et al.* STEAP1 is associated with the invasive and oxidative stress phenotype of ewing tumors. *Mol. Cancer Res.* **10**, 52–65 (2012).

13. Carrasquillo, J. A. *et al.* Imaging patients with metastatic castration-resistant prostate cancer using 89Zr-DFO-MSTP2109A anti-STEAP1 antibody. *J. Nucl. Med.* **60**, 1517–1523 (2019).

14. Doran, M. G. *et al.* Annotating STEAP1 regulation in prostate cancer with 89Zr immuno-PET. *J. Nucl. Med.* **55**, 2045–2049 (2014).

15. O'Donoghue, J. A. *et al.* Pharmacokinetics and biodistribution of a [89Zr]Zr-DFO-MSTP2109A Anti-STEAP1 antibody in metastatic castration-resistant prostate cancer patients. *Mol. Pharm.* **16**, 3083–3090 (2019).

16. Danila, D. C. *et al.* Phase i Study of DSTP3086S, an antibody-drug conjugate

targeting six-transmembrane epithelial antigen of prostate 1, in metastatic castration-resistant prostate cancer. *J. Clin. Oncol.* **37**, 3518–3527 (2019).

17. Williams, S. P. *et al.* ImmunoPET helps predicting the efficacy of antibody-drug conjugates targeting TENB2 and STEAP1. *Oncotarget* **7**, 25103–25112 (2016).

18. Boswell, C. A. *et al.* Impact of drug conjugation on pharmacokinetics and tissue distribution of Anti-STEAP1 antibody-drug conjugates in rats. *Bioconjug. Chem.* **22**, 1994–2004 (2011).

19. Krupa, M. *et al.* Immunization with recombinant DNA and modified vaccinia virus Ankara (MVA) vectors delivering PSCA and STEAP1 antigens inhibits prostate cancer progression. *Vaccine* **29**, 1504–1513 (2011).

20. Schober, S. J. *et al.* MHC Class I-Restricted TCR-Transgenic CD4+ T Cells Against STEAP1 Mediate Local Tumor Control of Ewing Sarcoma In Vivo. *Cells* **9**, 1–16 (2020).

21. Chen, X. *et al.* Inhibition of mouse RM-1 prostate cancer and B16F10 melanoma by the fusion protein of HSP65 & STEAP1 186-193. *Biomed. Pharmacother.* **111**, 1124–1131 (2019).

22. Zhao, Z. *et al.* Predictive potential of STEAP family for survival, immune microenvironment and therapy response in glioma. *Int. Immunopharmacol.* **101**, 108183 (2021).

23. Gomes, I. M., Santos, C. R. & Maia, C. J. Expression of steap1 and steap1b in prostate cell lines, and the putative regulation of steap1 by post-transcriptional and post-translational mechanisms. *Genes and Cancer* **5**, 142–151 (2014).

24. Löw, C. *et al.* High-throughput analytical gel filtration screening of integral membrane proteins for structural studies. *Biochim. Biophys. Acta - Gen. Subj.* **1830**, 3497–3508 (2013).

25. Nji, E., Li, D., Doyle, D. A. & Caffrey, M. Cloning, expression, purification, crystallization and preliminary X-ray diffraction of a lysine-specific permease from Pseudomonas aeruginosa. *Acta Crystallogr. Sect. F Struct. Biol. Commun.* **70**, 1362–1367 (2014).

26. Merilaïnen, G. & Wierenga, R. K. Crystallization and preliminary X-ray diffraction studies of the C-terminal domain of Chlamydia trachomatis CdsD. *Acta Crystallogr. Sect. F Struct. Biol. Commun.* **70**, 1431–1433 (2014).

27. Thangavelu Muthukumar, J. E. S. and G. K. Biological Role of Gellan Gum in Improving Sca ff old Drug Delivery , Cell Adhesion Properties for Tissue. *Molecules* **24**, 22 (2019).

28. Zia, K. M. *et al.* Recent trends on gellan gum blends with natural and synthetic polymers: A review. *Int. J. Biol. Macromol.* **109**, 1068–1087 (2018).

29. Danalache, F., Carvalho, C. Y., Alves, V. D., Moldão-Martins, M. & Mata, P. Optimisation of gellan gum edible coating for ready-to-eat mango (Mangifera indica L.) bars. *Int. J. Biol. Macromol.* **84**, 43–53 (2016).

30. Vieira, S. *et al.* Self-mineralizing Ca-enriched methacrylated gellan gum beads for bone tissue engineering. *Acta Biomater.* **93**, 74–85 (2019).

31. Park, H. *et al.* Enhanced biodegradation of hydrocarbons by Pseudomonas aeruginosa-encapsulated alginate/gellan gum microbeads. *J. Hazard. Mater.* **406**, (2021).

32. Lyu, C. J. *et al.* Biosynthesis of γ-aminobutyrate by engineered Lactobacillus brevis cells immobilized in gellan gum gel beads. *J. Biosci. Bioeng.* **128**, 123–128 (2019).

33. Villarreal-Otalvaro, C. & Coburn, J. M. Fabrication Methods and Form Factors of Gellan Gum-Based Materials for Drug Delivery and Anti-Cancer Applications. *ACS Biomater. Sci. Eng.* (2021) doi:10.1021/acsbiomaterials.1c00685.

34. Racovita, S., Lungan, M. A., Bunia, I., Popa, M. & Vasiliu, S. Adsorption and release studies of cefuroxime sodium from acrylic ion exchange resin microparticles coated with gellan. *React. Funct. Polym.* **105**, 103–113 (2016).

35. Gomes, D. *et al.* Applications of gellan natural polymer microspheres in recombinant catechol-O-methyltransferase direct capture from a Komagataella pastoris lysate. *Int. J. Biol. Macromol.* **172**, 186–196 (2021).

36. Gomes, D., Costa, D., Queiroz, J. A., Passarinha, L. A. & Sousa, A. A new insight in gellan microspheres application to capture a plasmid DNA vaccine from an Escherichia coli lysate. *Sep. Purif. Technol.* **274**, 119013 (2021).

37. Lei, L. *et al.* Antimicrobial hydrogel microspheres for protein capture and wound healing. *Mater. Des.* **215**, 110478 (2022).

38. Koubková, J. *et al.* Magnetic poly(glycidyl methacrylate) microspheres for protein capture. *N. Biotechnol.* **31**, 482–491 (2014).

39. Zhou, J. *et al.* Thiolactone-based conjugation assisted magnetic imprinted microspheres for specific capturing target proteins. *Chem. Eng. J.* **399**, 125767 (2020).

40. Lei, L. *et al.* Magnetic biohybrid microspheres for protein purification and chronic wound healing in diabetic mice. *Chem. Eng. J.* **425**, 130671 (2021).

41. Mahajan, H. S. & Gattani, S. G. Gellan Gum Based Microparticles of Metoclopromide Hydrochloride for Intranasal Delivery: Development and Evaluation. *Chem. Pharm. Bull. (Tokyo).* **57**, 388–392 (2009).

42. Lin, S. H. & Guidotti, G. *Chapter 35 Purification of Membrane Proteins*. *Methods in Enzymology* vol. 463 (Elsevier Inc., 2009).

43. Coelho, J. *et al.* Biosynthesis and isolation of gellan polysaccharide to formulate microspheres for protein capture. *Carbohydr. Polym.* **220**, 236–246 (2019).

44. Duarte, D. R. *et al.* Impact of glycerol feeding profiles on STEAP1 biosynthesis by Komagataella pastoris using a methanol-inducible promoter. *Appl. Microbiol. Biotechnol.* **105**, 4635–4648 (2021).

45. Laemmli, U. K. Cleavage of structural proteins during the assembly of the head of bacteriophage T4. *Nature* **227**, 680–685 (1970).

46. Abbas, Z. & Marihal, S. Gellan gum-based mucoadhesive microspheres of almotriptan for nasal administration: Formulation optimization using factorial design, characterization, and in vitro evaluation. *J. Pharm. Bioallied Sci.* **6**, 267 (2014).

47. Fan, Y., Yi, J., Hua, X., Zhang, Y. & Yang, R. Preparation and characterization of gellan gum microspheres containing a cold-adapted β-galactosidase from Rahnella sp. R3. *Carbohydr. Polym.* **162**, 10–15 (2017).

48. Babu, R., Sathigari, S., Kumar, M. & Pandit, J. Formulation of Controlled Release Gellan Gum Macro Beads of Amoxicillin. *Curr. Drug Deliv.* **7**, 36–43 (2010).

49. Agnihotri, S. A. & Aminabhavi, T. M. Development of Novel Interpenetrating Network Gellan Gum-Poly(vinyl alcohol) Hydrogel Microspheres for the Controlled Release of Carvedilol. *Drug Dev. Ind. Pharm.* **31**, 491–503 (2005).

50. Dhanka, M., Shetty, C. & Srivastava, R. Methotrexate loaded gellan gum microparticles for drug delivery. *Int. J. Biol. Macromol.* **110**, 346–356 (2018).

51. Kozlowski, L. P. Proteome-pI: Proteome isoelectric point database. *Nucleic Acids Res.* **45**, D1112–D1116 (2017).

52. Blanchard, V. *et al.* High-level expression of biologically active glycoprotein hormones in Pichia pastoris strains - Selection of strain GS115, and not X-33, for the production of biologically active N-glycosylated 15N-labeled phCG. *Glycoconj. J.* **25**, 245–257 (2008).

53. Tsuji, Y. Transmembrane protein western blotting: Impact of sample preparation on detection of SLC11A2 (DMT1) and SLC40A1 (ferroportin). *PLoS One* **15**, 1–18 (2020).

54. Seddon, A. M., Curnow, P. & Booth, P. J. Membrane proteins, lipids and detergents: Not just a soap opera. *Biochim. Biophys. Acta - Biomembr.* **1666**, 105–117 (2004).

55. Kalipatnapu, S. & Chattopadhyay, A. Membrane protein solubilization: Recent advances and challenges in solubilization of serotonin1A receptors. *IUBMB Life* **57**, 505–512 (2005).

56. Pedro, A. Q., Gonçalves, A. M., Queiroz, J. A. & Passarinha, L. A. Purification of Histidine-Tagged Membrane-Bound Catechol-O-Methyltransferase from Detergent-Solubilized Pichia pastoris Membranes. *Chromatographia* **81**, 425–434 (2018).

57. Reyes-Alcaraz, A., Martínez-Archundia, M., Ramon, E. & Garriga, P. Salt effects on the conformational stability of the visual G-protein-coupled receptor rhodopsin. *Biophys. J.* **101**, 2798–2806 (2011).

58. Bacelar, A. H., Silva-Correia, J., Oliveira, J. M. & Reis, R. L. Recent progress in gellan gum hydrogels provided by functionalization strategies. *J. Mater. Chem. B* **4**, 6164–6174 (2016).

59. Huang, C. J. *et al.* A proteomic analysis of the Pichia pastoris secretome in methanol-induced cultures. *Appl. Microbiol. Biotechnol.* **90**, 235–247 (2011).

60. Huo, S. F. *et al.* STEAP1 facilitates metastasis and epithelial-mesenchymal transition of lung adenocarcinoma via the JAK2/STAT3 signaling pathway. *Biosci. Rep.* **40**, 1–10 (2020).

61. Guo, Q. *et al.* Evaluation of the Prognostic Value of STEAP1 in Lung Adenocarcinoma and Insights Into Its Potential Molecular Pathways via Bioinformatic Analysis. *Front. Genet.* **11**, 1–13 (2020).

62. Nakamura, H. *et al.* Six-transmembrane epithelial antigen of the prostate 1 protects against increased oxidative stress via a nuclear erythroid 2-related factor pathway in colorectal cancer. *Cancer Gene Ther.* **26**, 313–322 (2019).

63. Zhang, Z. *et al.* A research of STEAP1 regulated gastric cancer cell proliferation, migration and invasion in vitro and in vivos. *J. Cell. Mol. Med.* **24**, 14217–14230 (2020).

64. Narkar, M., Sher, P. & Pawar, A. Stomach-Specific Controlled Release Gellan Beads of Acid-Soluble Drug Prepared by Ionotropic Gelation Method. *AAPS*

PharmSciTech **11**, 267–277 (2010).

65. Kawaguchi, H. Functional polymer microspheres. *Prog. Polym. Sci.* **25**, 1171–1210 (2000).

66. Cassanelli, M., Prosapio, V., Norton, I. & Mills, T. Acidified/basified gellan gum gels: The role of the structure in drying/rehydration mechanisms. *Food Hydrocoll.* **82**, 346–354 (2018).

67. Kermani, A. A. A guide to membrane protein X-ray crystallography. *FEBS J.* **288**, 5788–5804 (2021).

68. Stetsenko, A. & Guskov, A. An overview of the top ten detergents used for membrane protein crystallization. *Crystals* **7**, (2017).

69. Barroca-Ferreira, J. *et al.* Targeting STEAP1 Protein in Human Cancer: Current Trends and Future Challenges. *Curr. Cancer Drug Targets* **18**, 222–230 (2018).

70. Muñoz, A. & Costa, M. Elucidating the mechanisms of nickel compound uptake: A review of particulate and nano-nickel endocytosis and toxicity. *Toxicol. Appl. Pharmacol.* **260**, 1–16 (2012).

71. Poetz, O., Luckert, K., Herget, T. & Joos, T. O. Microsphere-based co-immunoprecipitation in multiplex. *Anal. Biochem.* **395**, 244–248 (2009).

72. Barroca-Ferreira, J. *et al.* Enhanced stability of detergent-free human native STEAP1 protein from neoplastic prostate cancer cells upon an innovative isolation procedure. *Int. J. Mol. Sci.* **22**, 1–15 (2021).

73. Noyes, A., Godavarti, R., Titchener-Hooker, N., Coffman, J. & Mukhopadhyay, T. Quantitative high throughput analytics to support polysaccharide production process development. *Vaccine* **32**, 2819–2828 (2014).

74. Tokmakov, A. A., Kurotani, A. & Sato, K. I. Protein pI and Intracellular Localization. *Front. Mol. Biosci.* **8**, 1–6 (2021).